Synthesis and Applications of Pure and Sulphur Doped p-type $CuBO_2$ nanostructures by Molten-Salt route

A thesis submitted towards partial fulfilment of the requirements for the degree of

Master of Technology in Nano science and Technology

Submitted by

PULOK DAS

ROLL NO.: M4NST19005

Under the guidance of

Prof. Kalyan Kumar Chattopadhyay
School of Materials Science and Nanotechnology
Jadavpur University
Kolkata -700032

&

(Dr). Nirmalya Sankar Das
Department of Physics (BSH)
Techno International Batanagar
Kolkata 700141

Course affiliated to
Faculty of Engineering and Technology
Jadavpur University
Kolkata-700032
India

2019

M.Tech. (Nanoscience and Technology) course affiliated to

Faculty of Engineering and Technology

Jadavpur University

Kolkata, India

CERTIFICATE OF RECOMMENDATION

This is to certify that the thesis entitled "**Synthesis and Applications of Pure and Sulphur Doped p-type $CuBO_2$ nanostructures by Molten-Salt route**" is a bonafide work carried out by **PULOK DAS** under our supervision and guidance for partial fulfilment of the requirement of Master of Technology in Nanoscience and Technology in School of Materials Science and Nanotechnology during the academic session 2017-2019.

THESIS ADVISOR
Prof. Kalyan Kumar Chattopadhyay
School of Materials Science and Nanotechnology,
Jadavpur University,
Kolkata-700 032

DIRECTOR
Prof. Chandan Kumar Ghosh
School of Materials Science and Nanotechnology,
Jadavpur University,
Kolkata-700 032

THESIS ADVISOR
Dr. Nirmalya Sankar Das
Department of Physics (BSH)
Techno International Batanagar
Kolkata-700 141

DEAN
Faculty Council of Interdisciplinary Studies, Law and Management
Jadavpur University,
Kolkata-700 032

M.Tech. (Nanoscience and Technology) course affiliated to

Faculty of Engineering and Technology

Jadavpur University

Kolkata, India

CERTIFICATE OF APPROVAL **

This foregoing thesis is hereby approved as a credible study of an engineering subject carried out and presented in a manner satisfactorily to warranty its acceptance as a prerequisite to the degree for which it has been submitted. It is understood that by this approval the undersigned do not endorse or approve any statement made or opinion expressed or conclusion drawn therein but approve the thesis only for purpose for which it has been submitted.

Committee of final examination ----------

for evaluation of Thesis ----------

**** Only in case the thesis is approved.**

DECLARATION OF ORIGINALITY AND COMPLIANCE OF ACADEMIC ETHICS

I hereby declare that this thesis contains literature survey and original research work by the undersigned candidate, as part of his Master of Technology (Nano science and Technology) studies during academic session 2017-2019.All information in this document has been obtained and presented in accordance with academic rules and ethical conduct.

I also declare that, as required by this rules and conduct, I have fully cited and referred all material and results that are not original to this work.

NAME: PULOK DAS

ROLL NUMBER: M4NST19005

THESIS TITLE: Synthesis and applications of pure and Sulphur doped p-type $CuBO_2$ nanostructures by Molten-Salt route.

SIGNATURE:
DATE:

Acknowledgement

In the first place, I would like to express my profound gratitude to my supervisor **Prof (Dr). Kalyan Kumar Chattopadhyay** for his advice and guidance from the very early stage of this research as well as giving me extraordinary experiences throughout the work. Above all and the most needed, he provided me constant encouragement and support in various ways. Thank you also for the amicable environment conducive to extensive research work at Thin Film and Nanoscience Lab, in which you have welcomed me. All these provided me great support, helping me to confront the difficult periods of my project, which I do not think I would have completed it otherwise.

I would like to express my special heartiest thanks to my co-supervisor (**Dr). Nirmalya Sankar Das** for his advices, guidance, and crucial contribution throughout my work. His involvement with his originality has triggered and nurtured my scholarly development that I will benefit from, for a long time to come. I really cannot value his support and generous cooperation. He was like an elder brother to me always by my side whenever i needed him. Without his guidance it would have been impossible for me to complete this project.

I would also like to express my sincere thanks to Dr. C. K. Ghosh, Dr. Mahua Ghosh Chowdhury, Dr. Sourav Sarkar, for their help, support, encouragement, suggestion and advice during the course of the research. Their enthusiasm provided me a helpful and effective way of learning which in turn inspired me to follow the research project with great enthusiasm.

I would also really like to thank all the staff members of School of Materials Science and Nanotechnolgy and Department of Physics for carrying out the critical characterization parts of the synthesized samples that composed a very important part of the thesis.

I extend my heartiest thanks to all my seniors of 'Thin Film & Nano Science' lab especially, Subhra di, Brahmi di, Souvik da, Biswojit da, Nripen da, Antika di, Ratna di, Karam da, Madhupriya di, Rimpa di, Tufan da, Subhasis da, Kaushik da, Sraboni di, Missi di, Rituparna di, and everyone in this lab for extending their helping hands. I would also like to thank all my friends Pratik, Ankita, Sumit, Debnath, Sourav, ankit, Sakat, Anupam, Utpal, moni, sandhi for their encouragement and cooperation.

Dedicated to my

PARENTS

for their support and encouragement.....

My Sincere gratitude to

All my teachers…..

Abstract

The works shown in the thesis –"Investigation on the Nanostructures of $CuBO_2$ p-type Transparent Conducting Metal Oxide" stresses on p-type novel copper delafossite $CuBO_2$. According to few previous reports, copper delafossites having $CuMO_2$ structure should have appreciable room temperature conductivity and wide band gap as the ionic radius of 'M' decreases. A plenty of works have been carried out with p type Cu delafossites after the discovery of $CuAlO_2$. Nanorods of $CuBO_2$, the latest member in the family of p-TCO, were prepared by an easy molten salt method for the first time. Following this process, p-type transparent conducting oxide $CuBO_2$ is considered as a novel and important addition in this delafossite family. Studies regarding this novel material have already indicated its high transparency and high electrical conductivity claiming the same as a promising material for "Transparent Electronics". Therefore, this novel is selected delafossite for this entire thesis work and emphasised on molten salt synthesis technique, investigation of its different physical and opto-electrical properties, and several interesting applications.

In this thesis work, synthesis of "S-doped $CuBO_2$" was achieved by an easy molten salt process. The synthesis was optimized by varying the molarity of the precursor and various synthesis parameters. Moreover, several synthesis parameters like molarity, temperature and synthesis duration could be controlled effectively. So we opted for molten-salt synthesis in our work.

Here we would like to report the first-time observation of its excellent electron field emission property from such p-type wide band gap material. Proper phase formation of the as-prepared samples was confirmed from x-ray diffraction studies whereas energy dispersive x-ray analysis showed the composition of the samples to be near stoichiometric. High resolution transmission electron microscopic studies were carried out to obtain morphological information and the exact particle size. Field emission scanning electron microscopic (FESEM) studies was carried out to obtain the morphology of $CuBO_2$ samples. The information regarding the work function was theoretically obtained using density functional theory. The optical transmittance and band gaps of the samples were obtained from ultraviolet-visible spectroscopic studies. The electron field emission property of the sample was studied with a standard field emission measurement set-up and the samples exhibited very good field emission performance compared to other Cu-delafossites, resulting in a turn-on field as low as with the maximum emission current density

up to which gradually decreased with increasing particle size. All the samples were tested for their photocatalysis performance under UV irradiation. It was observed that the $CuBO_2$ cubes having most distinct nanorods, which exhibited highest rate constant for rhodamine B degradation from water.

Contents

Acknowledgement

Abstract

Chapter 1: Introduction 1-27

1.1 Nanoscience & Nanotechnology 2
1.1.1 What is Nanotechnology 2
1.1.2 History of Nanotechnology 3
1.1.3 What is Nanometre Scale 4

1.2 What is Nanomaterials 5
1.2.1 History of Nanomaterials 5
1.2.2 Classification of Nanomaterials 6
1.2.3 Why so much interested in Nanomaterial 8
1.2.4 Nanomaterial Synthesis and Processing 9
1.2.5 Properties of Nanomaterials 13

1.3 Applications 15
1.3.1 Fuel cells 15
1.3.2 Catalysis 16
1.3.3 Field emission 16
1.3.4 Next-Generation Computer Chips 16
1.3.5 Super-capacitor 17
1.3.6 Elimination of Pollutants 17
1.3.7 Sensors 17
1.3.8 Medical and Healthcare application 18
1.3.9 Future transport 18

1.4 Photocatalysis 20
1.5 Chemical Modulation of Valance Band 20
1.6 Structure of copper delafossite 21
1.7 Introduction of $CuBO_2$ 22
1.8 Objectives 24

References 25

Chapter 2: Review of Past Work 28-40

2.1 General Idea 29
2.2 Some works about traditional delafossites 30
2.3 CuBO2 as a novel material 32
2.4 Different experimental synthesis methods of $CuBO_2$ 33
2.5 Review of detail Characterization Process 34
2.6 Review of Properties and Application of $CuBO_2$ 37
References 39

Chapter 3: Instruments & Apparatus 41-69

3.1 Major Synthesis Apparatus 42
3.1.1. Furnace and Oven 42
3.1.2. Pelletizer 42
3.1.3. Magnetic Stirrer 43
3.1.4. Spin coater 44
3.1.5. Hot Plate 45
3.2. Characterization Apparatus 46
3.2.1. X–Ray diffractometer (XRD) 46
3.2.2. Field Emission Scanning Electron Microscope (FESEM) 49
3.2.3. Ultraviolet Visible Spectrophotometer 53
3.2.4. Energy Dispersive Analysis of X−rays (EDAX) 57
3.2.5 Transmission electron microscope (TEM) 59
3.2.6. X-Ray Photoelectron Spectroscopy (XPS) 61
3.2.7. IV Characterization Apparatus 64
3.2.8 High Voltage DC power Supply 66
3.2.9. Electrometer, Multimeter 66
3.3. Application oriented equipment 66
3.3.1. Apparatus for field Emission property measurement 66
3.3.2. Apparatus for Photocatalysis measurement 67

Chapter 4: Modulation of Transport Properties of $CuBO_2$ by Sulphur doping 70-86

Abstract 71
4.1 Introduction 71
4.2 Experimental details 73
4.2.1 Synthesis 73
4.2.2 Characterization 74
4.3 Results and discussion 75
4.3.1 Structural studies 75
4.3.2 Compositional studies 77
4.3.3 Morphological studies 78
4.3.4 Optical studies 81
4.3.5 IV characteristics 82
4.4. Conclusion 84
Reference 85
Chapter 5: Enhancement of photocatalytic activity of $CuBO_2$ nano structures due to Sulphur doping **87-98**
Abstract 88
5.1 Introduction 88
5.2 Synthesis and characterization 90
5.3. Results and discussions 90
5.3.1. Crystallographic study 90
5.3.2. Morphological study 91
5.3.3. Composition study 92
5.3.4 Photocatalytic activity analysis 93
5.4. Conclusion 97
References 98
Chapter 6: Sulphur incorporation in CuBO2: enhancement of cold electron emission behaviour with optimized doping **99-111**
Abstract 100
6.1 Introduction 100
6.2 Synthesis and Characterization 101
6.2.1. Field emission experiment 102
6.3. Result and discussion 103
6.3.1. Structural studies 103

6.3.2. Morphological studies 104
6.3.3. Composition studies 105
6.3.4. Field emission studies 106
6.4. Conclusion 109
Reference 110
Chapter 7: Grand conclusion & Scope for Future works 112-115

7.1 Grand conclusion 113
7.2 Scope for future works 114

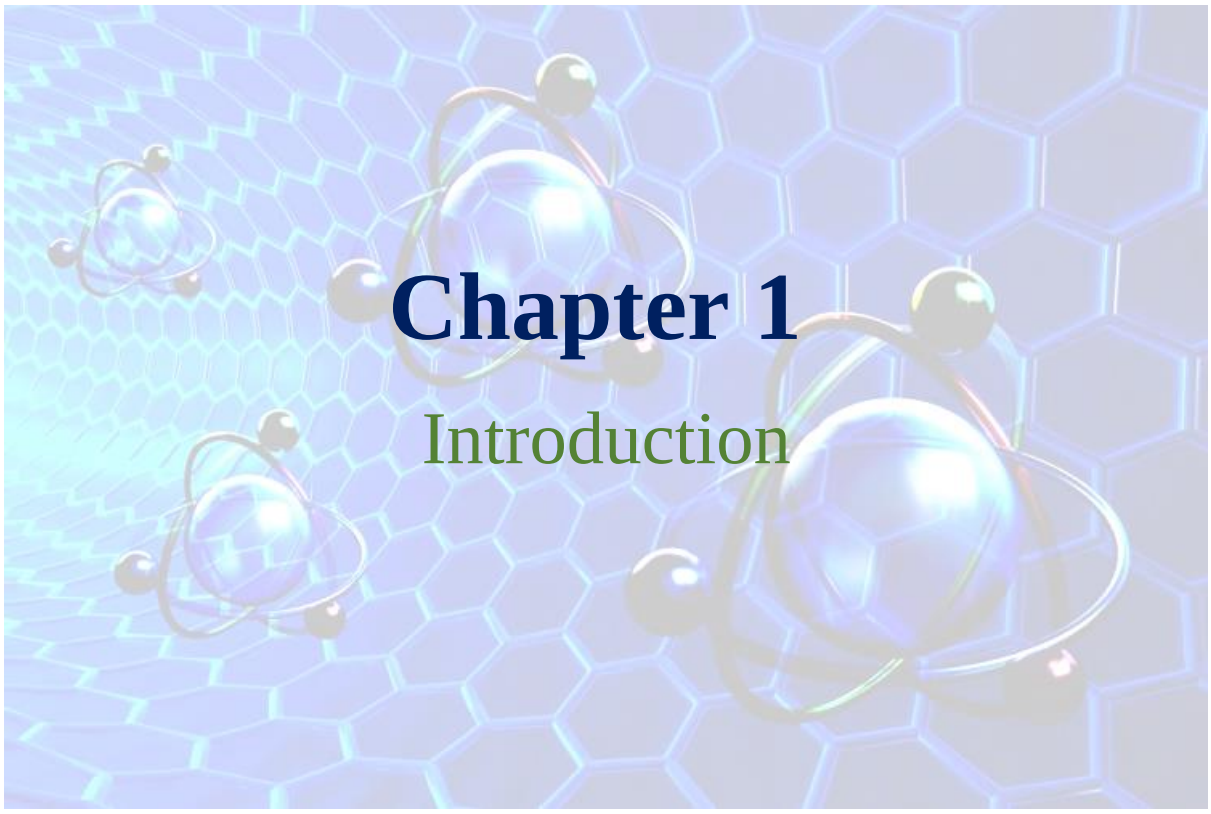

Chapter 1

Introduction

1.1 Nanoscience & Nanotechnology :

Nanoscience & technology is an interdisciplinary field of science and technology which has its early beginnings in the 1980s. It is science, engineering, and technology conducted at the nanoscale, which is about 1 to 100 nanometers. One nanometer is a billionth of a meter, or 10^{-9} of a meter. Nanotechnology is manipulation of matter on an atomic, molecular, and supramolecular scale. Nanotechnology as defined by size is naturally very broad, including fields of science as diverse as surface science, organic chemistry, molecular biology, semiconductor physics, energy storage, microfabrication, molecular engineering, etc. The associated research and applications are equally diverse, ranging from extensions of conventional device physics to completely new approaches based upon molecular self-assembly, from developing new materials with dimensions on the nanoscale to direct control of matter on the atomic scale.

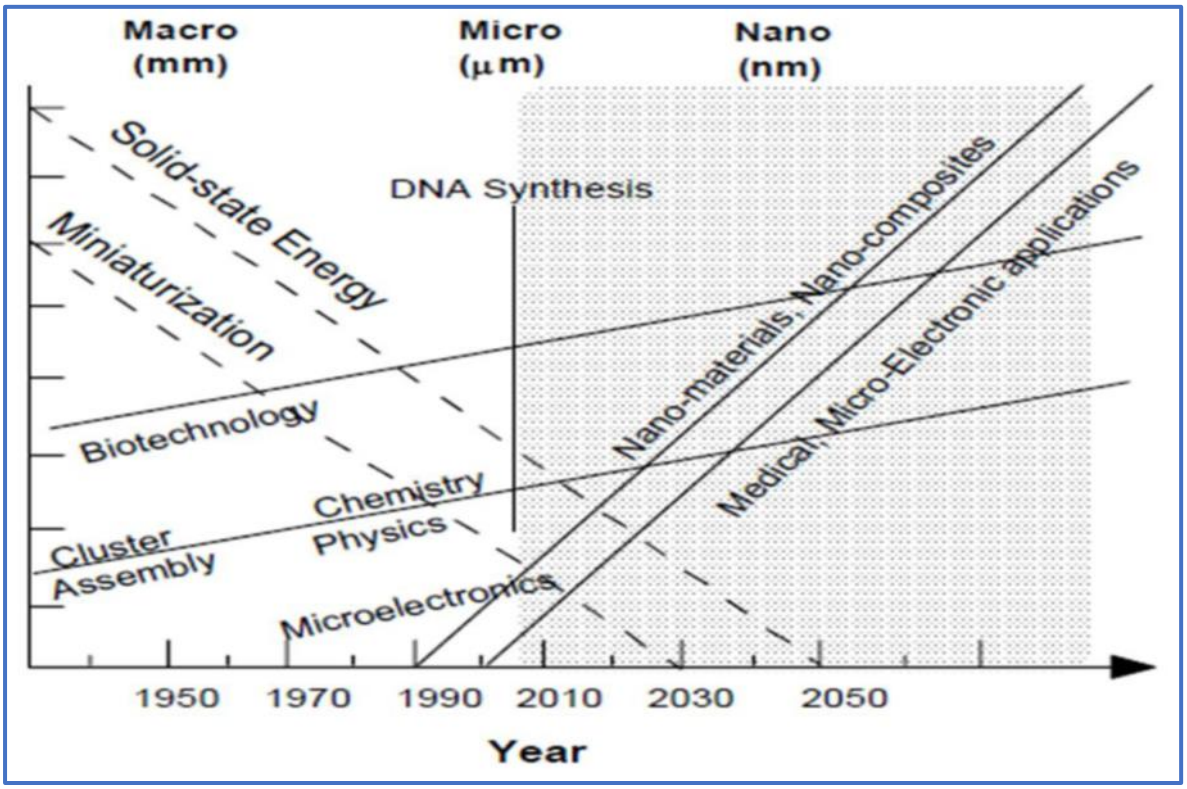

Figure 1.1: Time phase of Nanotechnology

1.1.1 What is Nanotechnology:

Maximum definitions turn around the study and control of phenomena and materials at length scales below 100 nm and pretty often they make a comparison with a human hair, which is

about 80,000 nm wide. The term “Nanotechnology" was invented by Professor Norio Tanaguchi at the university of tokyo in 1971. The original definition, translated into English “Nanotechnology" is the production technology to get the extra high accuracy and ultrafine dimensions, i.e. the preciseness and fineness on the order of 1 nm (nanometer), 10^{-9} meter in length [1]. In 1986, Drexler expanded Feynman's definition and defined nanotechnology as “Nanotechnology" is the principle of manipulation atom by atom, through control of the structure of matter at the molecular level [2]. In a broader sense, we consider a material to be in nanoscale if the material structurally at least in one dimension is less than 100 nanometer. This type of nanostructure can be defined as 2D nanostructure where one dimension is in nanoscale and other two are in microscale; example: thin-film. If two dimensions are less than 100 nanometers and one dimension is in microscale then we get 1D nanostructure i.e. nano rod and nano wires. The materials having nano dimension in all the directions are termed as nanoparticles, colloids, quantum dots etc...

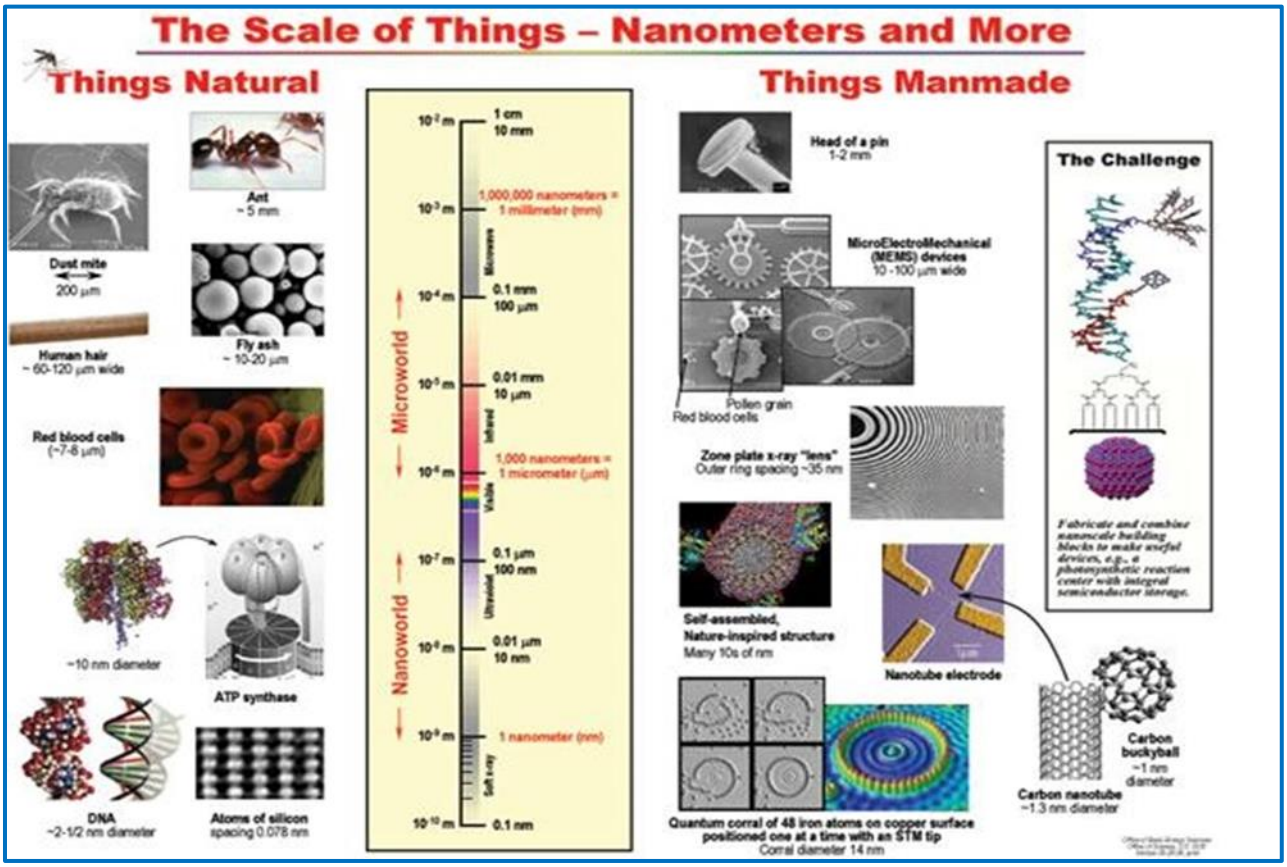

Figure1.2: Area of Nanoscience and Technology

1.1.2 History of Nanotechnology:

- The early 2000s also saw the beginnings of commercial applications of nanotechnology, although these were limited to bulk application of nanomaterials.

- The first ever concept was presented in 1959 by the famous professor of physics Dr. Richard Feynman.
- **1974:** "Nanotechnology"- Professor Norio Taniguchi for the first time uses the term nanotechnology [3].
- **1981:** IBM develops Scanning Tunnelling Microscope [4].
- **1985:** "Buckyball"- Scientists at Rice University and University of Sussex discover Fullerene (C60) [5].
- **1986**:"Engines of Creation"- First book on nanotechnology by K. Eric Drexler [6].
- **1989:** IBM logo made with individual atoms.
- **1991:** Carbon Nanotubes discovered by S. Ijima.
- **1999: "**Naano medicine"- First Nano medicine book by R. Freitas.
- **2000:** National Nanotechnology Initiative' was launched.
- **2003**: 21st century nanotechnology research report published.
- **2005:** DNA based computer discovered and algorithmic self assembly.
- **2007:** Lithium-ion battery with a common type of virus was discovered.
- **2009:** Several DNA-like robotic nanoscale assembly devices were discovered.
- **2010:** Invention of Graphene .
- **2014:** Updated 2014 strategic plan was released by the NNI.

1.1.3 What is Nanometre Scale:

The nanometre scale is conventionally indicated as 1 to 100 nm. One nanometre is one billionth of a meter. The size range is set normally to be minimum 1 nm to avoid single atoms or very small group of atoms to be designed as nano objects. Therefore nanoscience and nanotechnologies deal with at least clusters of atoms of 1nm size. The upper limit is normally 100nm, but this is a "fluid" limit, often objects with greater dimensions (even 200nm) are defined nanomaterials. A valid question a student might ask is "why 100 nm, and not 150 nm?", or even "why not 1 to 1000 nm?". The reason why the "1 to 100 nm range" is defined as approximate is that the definition itself focuses on the effect that the dimension on a certain material e.g. the insurgence of a quantum-phenomena rather than at what exact dimension this

effect arises. Nan science is not the science of small, but the science at which material with small dimension show new physical phenomena, collectively called quantum effect, which assize dependent and dramatically different from the properties of macro-scale materials.

1.2 What is Nanomaterials:

Nanoscale materials are defined as a set of substances where at least one dimension is less than approximately 100 nanometers. A nanometer is one millionth of a millimeter – approximately 100,000 times smaller than the diameter of a human hair. Nanomaterials are of interest because at this scale unique optical, magnetic, electrical, and other properties emerge. These emergent properties have the potential for great impacts in electronics, medicine, and other fields.

Figure 1.3: Nanomaterial (For example: Carbon nanotube)

1.2.1 History of Nanomaterials:

The history of nanomaterials began immediately after the big bang when Nanostructures were formed in the early meteorites. Nature later evolved many other Nanostructures like seashells, skeletons etc. Nanoscaled smoke particles were formed during the use of fire by early humans. The scientific story of nanomaterials however began much later. One of the first scientific report is the colloidal gold particles synthesized by Michael Faraday as early as 1857. Nanostructured catalysts have also been investigated for over 70 years. By the early 1940's, precipitated and fumed silica nanoparticles were being manufactured and sold in USA and Germany as substitutes for ultrafine carbon black for rubber reinforcements. Nanosized amorphous silica particles have found large-scale applications in many every-day consumer

products, ranging from non-diary coffee creamer to automobile tires, optical fibers and catalyst supports. In the 1960s and 1970's metallic nanopowders for magnetic recording tapes were developed. In 1976, for the first time, nanocrystals produced by the now popular inert- gas evaporation technique was published by Granqvist and Buhrman. Recently it has been found that the Maya blue paint is a nanostructured hybrid material. The origin of its color and its resistance to acids and biocorrosion are still not understood but studies of authentic samples from Jaina Island show that the material is made of needle-shaped paly gorskite (clay) crystals that form a superlattice with a period of 1.4 nm, with intercalates of amorphous silicate substrate containing inclusions of metal (Mg) nanoparticles. The beautiful tone of the blue color is obtained only when both these nanoparticles and the superlattice are present, as has been shown by the fabrication of synthetic samples.

A nanomaterial is an object that has at least one dimension in the nanometre scale. First, all nanomaterial consist of very small particles. This is the first advantage of nanomaterial and nanotechnologies, promoting attainment of super miniaturization. Because they are small, nanostructures can be packed very closely together. As a result, on a given unit of area one can locate more functional nanodevices, which is very important for Nanoelectronics. Their high packing density has the potential to bring higher area and volume capacity to information storage and higher speed to information processing.

Today nanophase engineering expands in a rapidly growing number of structural and functional materials, both inorganic and organic, allowing to manipulate mechanical, catalytic, electric, magnetic, optical and electronic functions. The production of nanophase or cluster-assembled materials is usually based upon the creation of separated small clusters which then are fused into a bulk-like material or on their embedding into compact liquid or solid matrix materials. e.g. nanophase silicon, which differs from normal silicon in physical and electronic properties, could be applied to macroscopic semiconductor processes to create new devices. For instance, when ordinary glass is doped with quantized semiconductor "colloids," it becomes a high performance optical medium with potential applications in optical computing.

1.2.2 Classification of Nanomaterials:

Nanomaterials have extremely small size which having at least one dimension 100 nm or less. Nanomaterials can be nanoscale in one dimension (e.g. surface films), two dimensions (e.g. strands or fibres), or three dimensions (e.g. particles). They can exist in single, fused,

aggregated or agglomerated forms with spherical, tubular, and irregular shapes. Common types of nanomaterials include nanotubes, dendrimers, quantum dots and fullerenes. Nanomaterials have applications in the field of nano technology, and displays different physical chemical characteristics from normal chemicals (i.e., silver nano, carbon nanotube, fullerene, photocatalyst, carbon nano, silica). There are various types of nanoscale structures like, thin films, nanowires, nanoparticles etc. Nanoparticles are often called as quantum dots and can be considered as quasi zero dimensional systems. It is nothing but basic physics acting behind the novel properties of the above mentioned systems and it has been well explained by theoretical research. To understand these systems, it is very essential to discuss the density of states (DOS) of quantum dots (0 dimension), quantum wires (1 dimension) and quantum wells (2 dimensions) in brief.

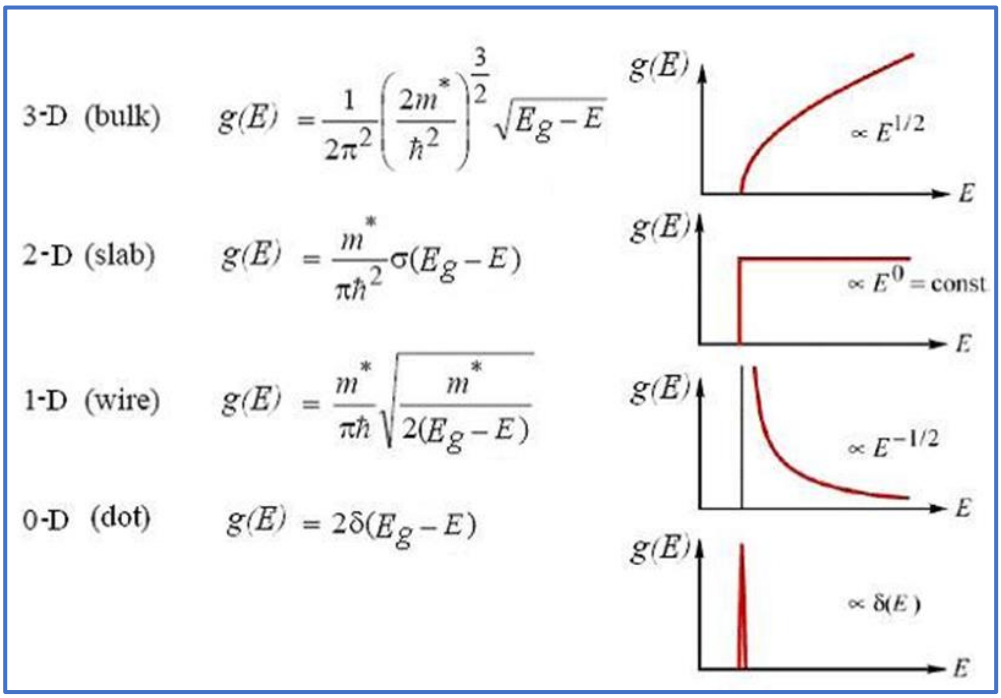

Table 1.1: Density of states

Nanomaterials are materials which are characterized by an ultra fine grain size (< 50 nm) or by a dimensionality limited to 50 nm. Nanomaterials can be created with various modulation dimensionalities as defined by Richard W. Siegel: zero (atomic clusters, filaments and cluster assemblies), one (multilayers), two (ultrafine-grained overlayers or buried layers), and three

(nanophase materials consisting of equiaxed nanometer sized grains).

Classification	Examples
Dimension ▪ 1 dimension ▪ 2 dimension ▪ 3 dimension	Films, coatings, multilayer, etc. Tubes, fibers, wires, platelets, etc. Particles, quantum dots, hallow spheres, etc.
Phase Composition ▪ Single-phase solid ▪ Multi-phase solid ▪ Multi-phase system	Crystalline, amorphous, particles and layers, etc. Matrix composites, coated particles, etc. Colloid, aerogels, ferrofluids, etc.
Manufacturing Process ▪ Gas phase reaction ▪ Liquid phase reaction ▪ Mechanical procedures	Flame synthesis, condensation, CVD, etc. Sol-gel, precipitation, hydrothermal processing, etc. Ball milling, plastic deformation, etc.

Table1.2: Classification of nanomaterial with regard to different parameters

1.2.3 Why so much interested in Nanomaterial:

These materials have created a high interest in recent years by virtue of their unusual mechanical, electrical, optical and magnetic properties. Some examples are given below:

- Nanophase ceramics are of particular interest because they are more ductile at elevated temperatures as compared to the coarse-grained ceramics.

- Nanostructured semiconductors are known to show various non-linear optical properties. Semiconductor Q-particles also show quantum confinement effects which may lead to special properties, like the luminescence in silicon powders and silicon germanium quantum dots as infrared optoelectronic devices. Nanostructured semiconductors are used as window layers in solar cells.

- Nanosized metallic powders have been used for the production of gas tight materials, dense parts and porous coatings. Cold welding properties combined with the ductility make them suitable for metal-metal bonding especially in the electronic industry.

- Single nanosized magnetic particles are mono-domains and one expects that also in magnetic nanophase materials the grains correspond with domains, while boundaries on the contrary to disordered walls. Very small particles have special atomic structures with discrete electronic states, which give rise to special properties in addition to the super

para magnetism behaviour. Magnetic nanocomposites have been used for mechanical force transfer (ferrofluids), for high density information storage and magnetic refrigeration.

- Nanostructured metal clusters and colloids of mono- or pluri metallic composition have a special impact in catalytic applications. They may serve as precursors for new type of heterogeneous catalysts (Cortex-catalysts) and have been shown to offer substantial advantages concerning activity, selectivity and lifetime in chemical transformations and electrocatalysis (fuel cells). Enantioselective catalysis was also achieved using chiral modifiers on the surface of nanoscale metal particles.

- Nanostructured metal-oxide thin films are receiving a growing attention for the realization of gas sensors (NOx, CO, CO_2, CH_4 and aromatic hydrocarbons) with enhanced sensitivity and selectivity. Nanostructured metal-oxide (MnO_2) finds application for rechargeable batteries for cars or consumer goods. Nanocrystalline silicon films for highly transparent contacts in thin film solar cell and nano-structured titanium oxide porous films for its high transmission and significant surface area enhancement leading to strong absorption in dye sensitized solar cells.

- Polymer based composites with a high content of inorganic particles leading to a high dielectric constant are interesting materials for photonic band gap structure.

1.2.4 Nanomaterial Synthesis and Processing:

There are many different ways of creating nanostructures: of course, macromolecules or nanoparticles or bucky balls or nanotubes and so on can be synthesized artificially for certain specific materials. They can also be arranged by methods based on equilibrium or near equilibrium thermodynamics such as methods of self-organization and self-assembly (sometimes also called bio-mimetic processes). Using these methods, synthesized materials can be arranged into useful shapes so that finally the material can be applied to a certain application. We are dealing with very fine structures: a nanometer is a billionth of a meter. This indeed allows us to think in both the ‘bottom up’ or the ‘top down’ approaches to synthesize nanomaterials, i.e. either to assemble atoms together or to dis-assemble (break, or dissociate) bulk solids into finer pieces until they are constituted of only a few atoms.

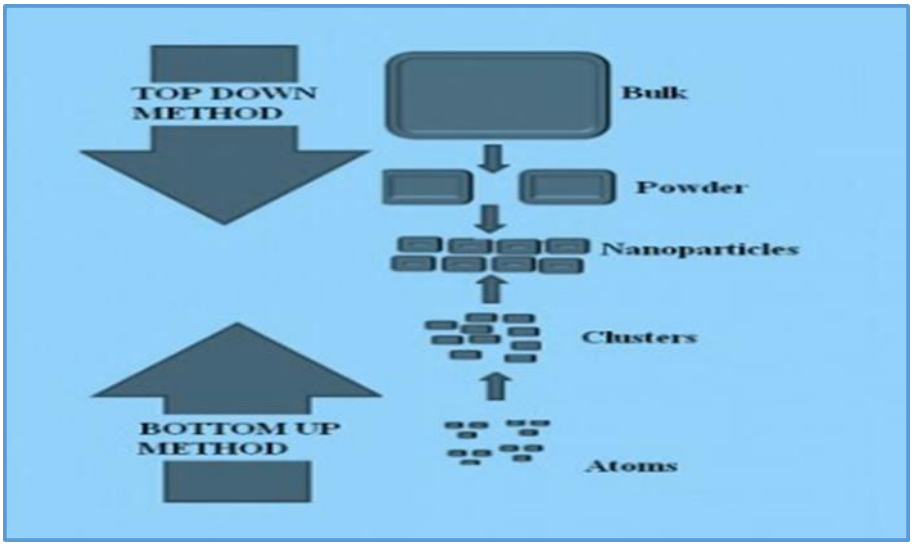

Fig 1.4: Top down and bottom up

(1) Mechanical grinding:

Mechanical attrition is a typical example of 'top down' method of synthesis of nanomaterials, where the material is prepared not by cluster assembly but by the structural decomposition of coarser-grained structures as the result of severe plastic deformation. This has become a popular method to make nanocrystalline materials because of its simplicity, the relatively inexpensive equipment needed, and the applicability to essentially the synthesis of all classes of materials. Mechanical milling is typically achieved using high energy shaker, planetary ball, or tumbler mills. The energy transferred to the powder from refractory or steel balls depends on the rotational (vibrational) speed, size and number of the balls, ratio of the ball to powder mass, the time of milling and the milling atmosphere. Nanoparticles are produced by the shear action during grinding.

(2) Sol-gel process:

The sol-gel process, involves the evolution of inorganic networks through the formation of a colloidal suspension (sol) and gelation of the sol to form a network in a continuous liquid phase (gel). The precursors for synthesizing these colloids consist usually of a metal or metalloid element surrounded by various reactive ligands. The starting material is processed to form a

dispersible oxide and forms a sol in contact with water or dilute acid. Removal of the liquid from the sol yields the gel, and the sol/gel transition controls the particle size and shape. Calcination of the gel produces the oxide. Sol-gel processing refers to the hydrolysis and condensation of alkoxide-based precursors such as $Si(OEt)_4$ (tetraethyl orthosilicate, or TEOS). The reactions involved in the sol-gel chemistry based on the hydrolysis and condensation of metal alkoxides M(OR)z can be described as follows:

$$MOR + H_2O \rightarrow MOH + ROH \text{ (hydrolysis)}$$

$$MOH + ROM \rightarrow M\text{-}O\text{-}M + ROH \text{ (condensation)}$$

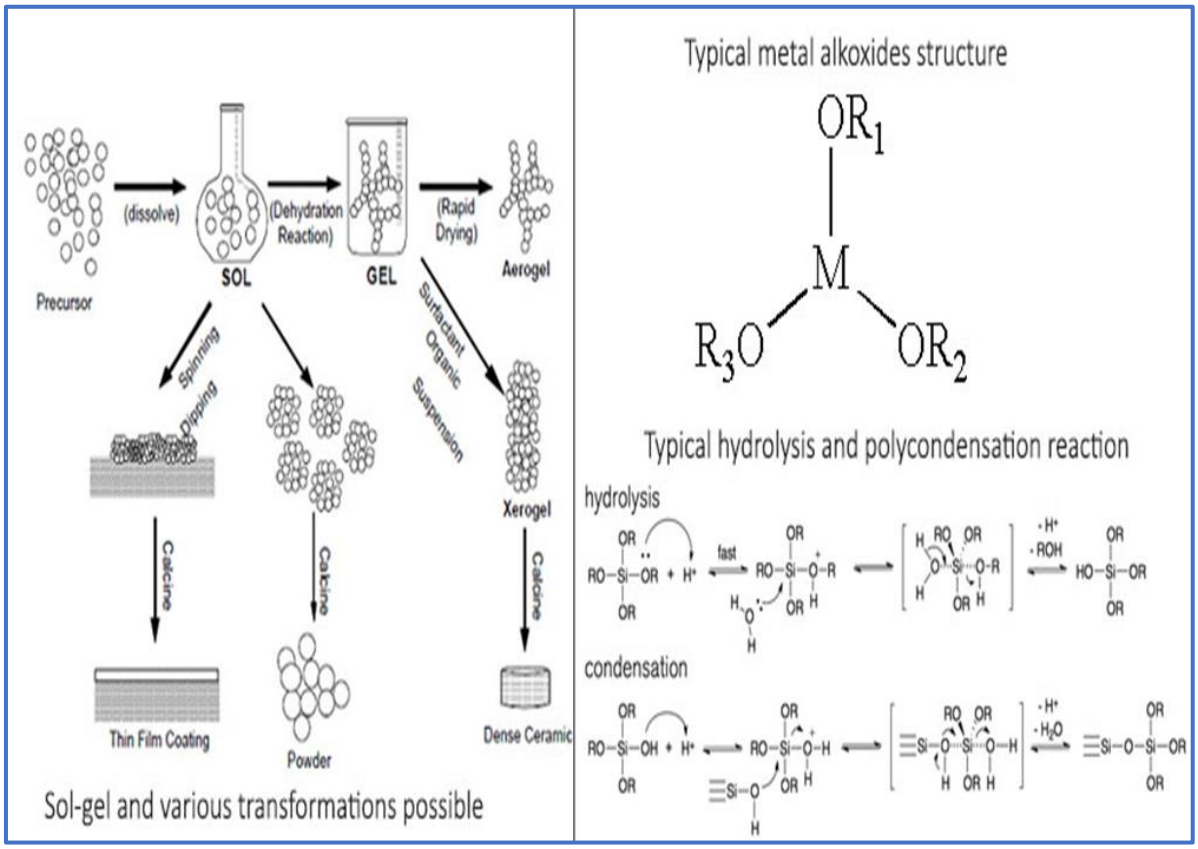

Fig 1.5: Mechanism of Sol-Gel process [7]

(3) Gas Phase synthesis of nanomaterials:

The gas-phase synthesis methods are of increasing interest because they allow elegant way to control process parameters in order to be able to produce size, shape and chemical composition controlled nanostructures. Before we discuss a few selected pathways for gas-phase formation of nanomaterials, some general aspects of gas-phase synthesis needs to be discussed. In conventional chemical vapour deposition (CVD) synthesis, gaseous products either are allowed

to react homogeneously or heterogeneously depending on a particular application.

(4) Solid States:

The simplest fashion to produce nanoparticles is by heating the desired material in a heatresistant crucible containing the desired material. This method is appropriate only for materials that have a high vapour pressure at the heated temperatures that can be as high as 2000 °C.

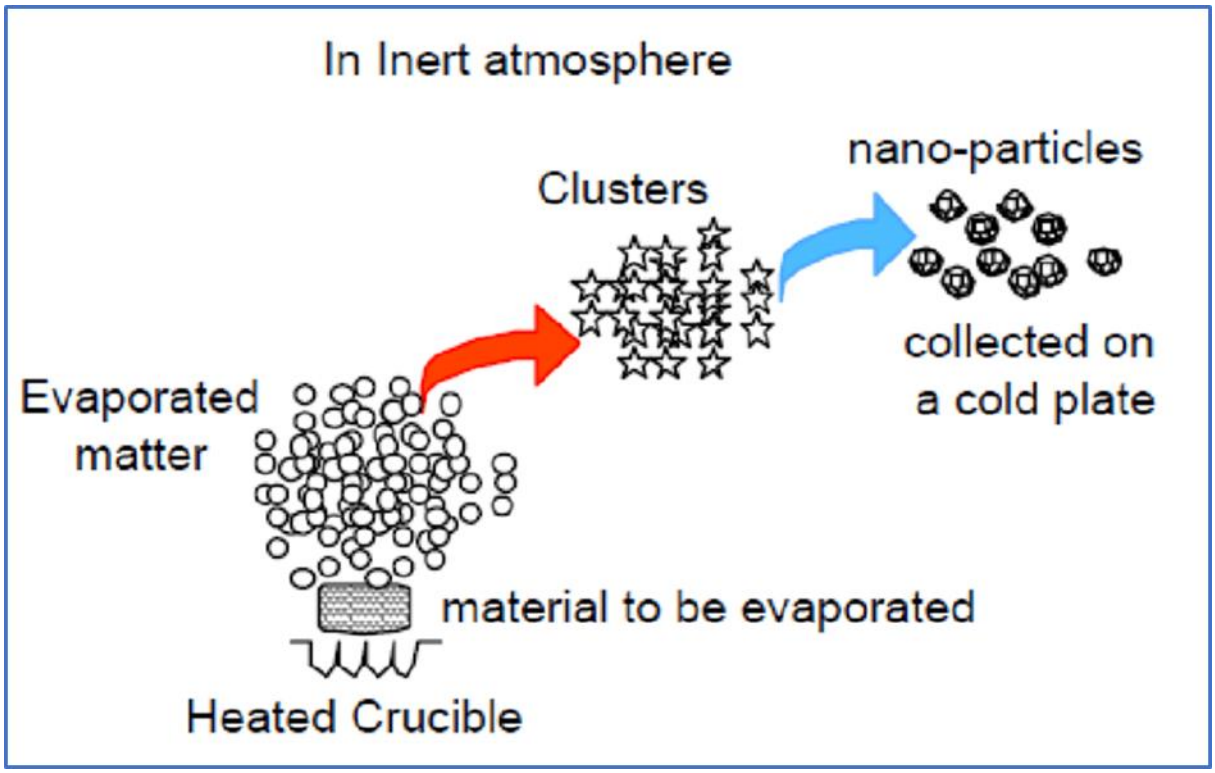

Figure 1.6: Schematic representation of gas phase process of synthesis [8]

(5) Chemical Vapour Condensation (CVC):

In Chemical vapor deposition the evaporative source used in GPC is replaced by a hot wall reactor in the Chemical Vapour Condensation or the CVC process. Depending on the processing parameters nucleation of nanoparticles is observed during chemical vapour deposition (CVC) of thin films and poses a major problem in obtaining good film qualities.
The original idea of the novel CVC process which is schematically shown below where, it was intended to adjust the parameter field during the synthesis in order to suppress film formation and enhance homogeneous nucleation of particles in the gas flow. It is readily found that the residence time of the precursor in the reactor determines if films or particles are formed. In a

certain range of residence time both particle and film formation can be obtained.

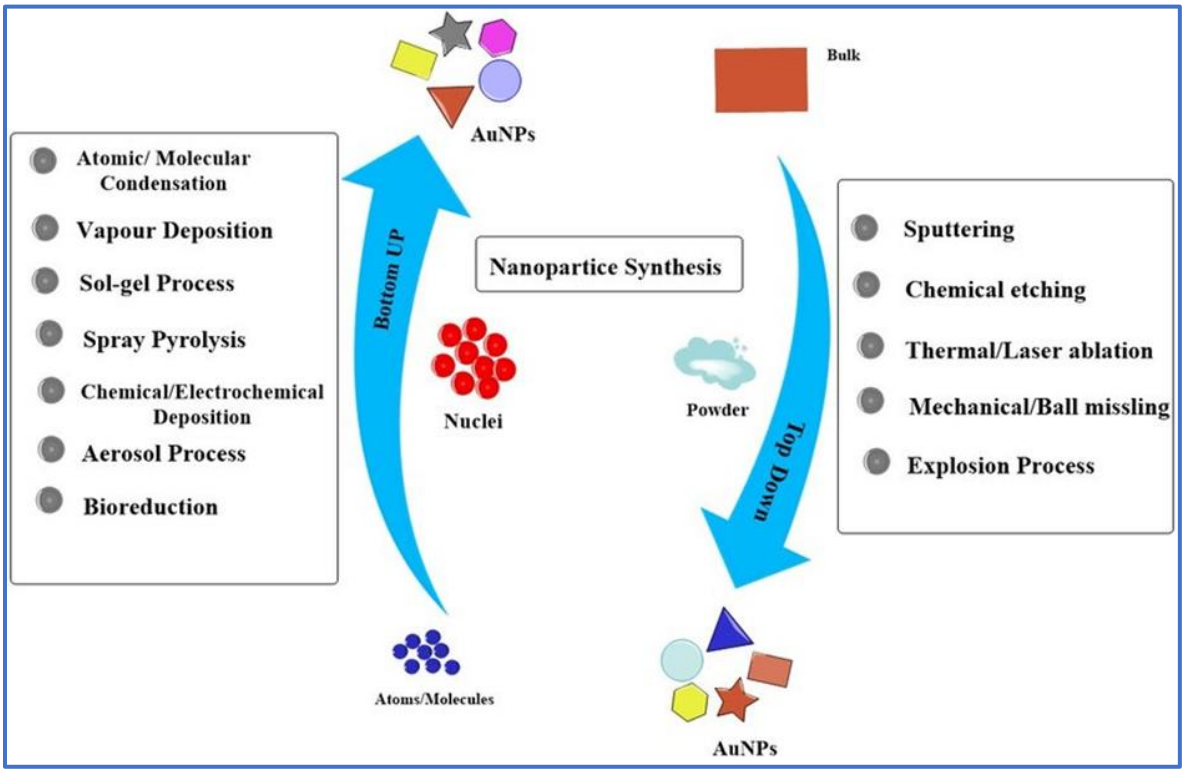

Figure 1.7: Schematic of Nanoparticle Synthesis

1.2.5 Properties of Nanomaterials:

Nanomaterials have the structural features in between of those of atoms and the bulk materials. While most micro structured materials have similar properties to the corresponding bulk materials, the properties of materials with nanometer dimensions are significantly different from those of atoms and bulks materials. This is mainly due to the nanometer size of the materials which render them: (i) large fraction of surface atoms; (ii) high surface energy; (iii) spatial confinement; (iv) reduced imperfections, which do not exist in the corresponding bulk materials [9]. Due to their small dimensions, nanomaterials have extremely large surface area to volume ratio, which makes a large to be the surface or interfacial atoms, resulting in more "surface" dependent material properties. Especially when the sizes of nanomaterials are comparable to length, the entire material will be affected by the surface properties of nanomaterials. This in turn may enhance or modify the properties of the bulk materials. For example, metallic nanoparticles can be used as very active catalysts. Chemical sensors from

nanoparticles and nanowires enhanced the sensitivity and sensor selectivity. The nanometer feature sizes of nanomaterials also have spatial confinement effect on the materials, which bring the quantum effects [10].

(1) Optical properties:

One of the most fascinating and useful aspects of nanomaterials is their optical properties. Applications based on optical properties of nanomaterials include optical detector, laser, sensor, imaging, phosphor, display, solar cell, photocatalysis, photo-electrochemistry and biomedicine. The optical properties of nanomaterials depend on parameters such as feature size, shape, surface characteristics, and other variables including doping and interaction with the surrounding environment or other nanostructures [11]. It may also be controlled by dopant incorporation which changes the band gaps. The variation of band gap generally occurs due to the change of lattice parameters by annealing [12-13] or impurity doping [14-15].

(2) Electrical Properties:

Electrical Properties of Nanoparticles" discuss about fundamentals of electrical conductivity in nanotubes and nanorods, carbon nanotubes, photoconductivity of nanorods, electrical conductivity of nanocomposites. One interesting method which can be used to demonstrate the steps in conductance is the mechanical thinning of a nanowire and measurement of the electrical current at a constant applied voltage. The important point here is that, with decreasing diameter of the wire, the number of electron wave modes contributing to the electrical conductivity is becoming increasingly smaller by well-defined quantized steps. Charge transport phenomenon for materials with nanoscale dimension mainly depends on the grain boundary [16]. The effects of grain boundary plays a very significant role as its interface contains a density of defects like vacancies, dangling bonds, vacancy clusters etc [17].

(3) Mechanical Properties:

Mechanical Properties of Nanoparticles" deals with bulk metallic and ceramic materials, influence of porosity, influence of grain size, super plasticity, filled polymer composites, particle filled polymers, polymer-based nanocomposites filled with platelets, carbon nanotube-

based composites. The discussion of mechanical properties of nanomaterials is, in to some extent, only of quite basic interest, the reason being that it is problematic to produce macroscopic bodies with a high density and a grain size in the range of less than 100 nm. However, two materials, neither of which is produced by pressing and sintering, have attracted much greater interest as they will undoubtedly achieve industrial importance. These materials are polymers which contain nanoparticles or nanotubes to improve their mechanical behaviors, and severely plastic-deformed metals, which exhibit astonishing properties. However, because of their larger grain size, the latter are generally not accepted as nanomaterials.

(4) Magnetic properties:

Bulk gold and Pt are non-magnetic, but at the nano size they are magnetic. Surface atoms are not only different to bulk atoms, but they can also be modified by interaction with other chemical ecies, that is, by capping the nanoparticles. This phenomenon opens the possibility to modify the physical properties of the nanoparticles by capping them with appropriate molecules. Actually, it should be possible that non-ferromagnetic bulk materials exhibit ferromagnetic-like behavior when prepared in nano range. One can obtain magnetic nanoparticles of Pd, Pt and the surprising case of Au (that is diamagnetic in bulk) from non-magnetic bulk materials. In the case of Pt and Pd, the ferromagnetism arises from the structural changes associated with size effects [18].

1.3 Applications:

1.3.1 Fuel cells:

A fuel cell is an electrochemical energy conversion device that converts the chemical energy from fuel (on the anode side) and oxidant (on the cathode side) directly into electricity. The heart of fuel cell is the electrodes. The performance of a fuel cell electrode can be optimized in two ways; by improving the physical structure and by using more active electro catalyst. A good structure of electrode must provide ample surface area, provide maximum contact of catalyst, reactant gas and electrolyte, facilitate gas transport and provide good electronic Carbon nanotubes (CNTs) have chemical stability, good mechanical properties and high surface area, making them ideal for the design of sensors and provide very high surface area due to its structural network. Since carbon nanotubes are also suitable supports for cell growth,

electrodes of microbial fuel cells can be built using of CNT. Conductance. In this fashion the structure should be able to minimize losses [19].

1.3.2 Catalysis:

Higher surface area available with the nanomaterial counterparts, nano-catalysts tend to have exceptional surface activity. For example, reaction rate at nano-aluminum can go so high, that it is utilized as a solid-fuel in rocket propulsion, whereas the bulk aluminum is widely used in utensils. Nano-aluminum becomes highly reactive and supplies the required thrust to send off pay loads in space. Similarly, catalysts assisting or retarding the reaction rates are dependent on the surface activity, and can very well be utilized in manipulating the rate-controlling step.

1.3.3 Field emission:

Nanoscale field emission have currently become a major focus of attention due to their applications in flat panel displays, dynamic computerized tomography (CT) scanners, vacuum microelectronic devices, infrared imaging devices, high intensity luminescent tubes, etc. The emission of electrons from a metal-vacuum interface, in the presence of an external electric field normal to the emitting surface, was initially treated as a quantum mechanical tunnelling process by Fowler and Nordheim (‘original’ F-N theory) [20]. It was found that the materials with wide band gap have low or negative electron affinity, which, in turn, enhances the low-macroscopic field emission properties. For many semiconducting material, its emission properties may give an additional impetus on the other properties opening up a new window in the field-emission technology with a new group of materials other than carbon-based films.

1.3.4 Next-Generation Computer Chips:

The microelectronics industry has been emphasizing miniaturization, whereby the circuits, such as transistors, resistors, and capacitors, are reduced in size. By achieving a significant reduction in their size, the microprocessors, which contain these components, can run much faster, thereby enabling computations at far greater speeds. However, there are several technological impediments to these advancements, including lack of the ultrafine precursors to manufacture these components; poor dissipation of tremendous amount of heat generated by

these microprocessors due to faster speeds; short mean time to failures (poor reliability), etc. Nanomaterials help the industry break these barriers down by providing the manufacturers with nanocrystalline starting materials, ultra-high purity materials, materials with better thermal conductivity, and longer-lasting, durable interconnections (connections between various components in the microprocessors). For example: Nanowires for junction less transistors:

1.3.5 Supercapacitor:

A super capacitor is a high-capacity capacitor with capacitance values much higher than other capacitors (but lower voltage limits) that bridge the gap between electrolytic and rechargeable. They typically store 10 to 100 times more energy per unit volume or than electrolytic capacitors, can accept and deliver charge much faster than batteries, and tolerate many more charge and discharge cycles than rechargeable batteries. A transition metal oxide exhibits high amounts of pseudo capacitance [21].

1.3.6 Elimination of Pollutants:

Nanomaterials possess extremely large grain boundaries relative to their grain size. Hence, they are very active in terms of their chemical, physical, and mechanical properties. Due to their enhanced chemical activity, nanomaterials can be used as catalysts to react with such noxious and toxic gases as carbon monoxide and nitrogen oxide in automobile catalytic converters and power generation equipment to prevent environmental pollution arising from burning gasoline and coal.

1.3.7 Sensors:

Sensors rely on the highly active surface to initiate a response with minute change in the concentration of the species to be detected. Engineered monolayers (few Angstroms thick) on the sensor surface are exposed to the environment and the peculiar functionality (such as change in potential as the CO/anthrax level is detected) is utilized in sensing.

1.3.8 Medical and Healthcare application:

Nanotechnology is already broadening the medical tools, knowledge, and therapies currently available to clinicians. Nanomedicine, the application of nanotechnology in medicine, draws on the natural scale of biological phenomena to produce precise solutions for disease prevention, diagnosis, and treatment. Below are some examples of recent advances in this area

- Commercial applications have adapted gold nanoparticles as probes for the detection of targeted sequences of nucleic acids, and gold nanoparticles are also being clinically investigated as potential treatments for cancer and other diseases.

- Nanotechnology researchers are working on a number of different therapeutics where a nanoparticle can encapsulate or otherwise help to deliver medication directly to cancer cells and minimize the risk of damage to healthy tissue. This has the potential to change the way doctors treat cancer and dramatically reduce the toxic reacts of chemotherapy.

- Research in the use of nanotechnology for regenerative medicine spans several application areas, including bone and neural tissue engineering. For instance, novel materials can be engineered to mimic the crystal mineral structure of human bone or used as a restorative resin for dental applications. Researchers are looking for ways to grow complex tissues with the goal of one day grow-ing human organs for transplant. Researchers are also studying ways to use graphene nanoribbons to help repair spinal cord injuries; preliminary research shows that neurons grow well on the conductive graphene surface.

1.3.9 Future transport:

Nanotechnology offers the promise of developing multifunctional materials that will contribute to building and maintaining lighter, safer, smarter, and more efficient vehicles, aircraft, spacecraft, and ships. In addition, nanotechnology offers various means to improve the transportation infrastructure :

- Nano-engineered materials in automotive products include polymer nano-composites structural parts; high-power rechargeable battery systems; thermo-electric materials for temperature control; lower rolling-resistance tires; high-efficiency/low-cost sensors and electronics; thin-film smart solar panels; and fuel additives and improved catalytic converters for cleaner exhaust and ex-tended range.

- Nanoscale sensors, communications devices, and other innovations enabled by nanoelectronics can also support an enhanced transportation infrastructure that can communicate with vehicle-based systems to help drivers maintain lane position, avoid collisions, adjust travel routes to avoid congestion, and improve drivers interfaces to onboard electronics

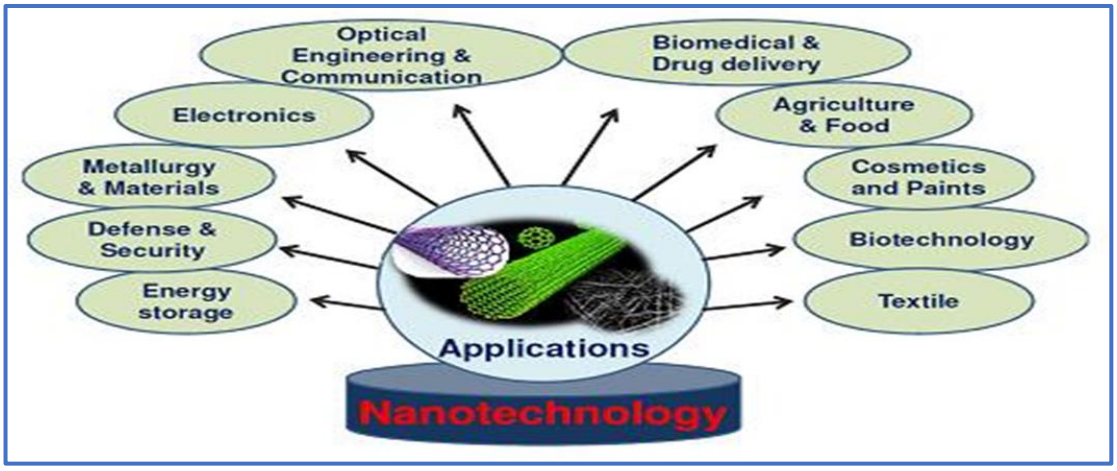

Figure 1.8: Application of Nanotechnology

1.4 Photocatalysis:

In today's world different industries like textile, cosmetic, paper, leather, pharmaceutical etc. Uses and produces a large amount of dyes as waste products which contaminates water soil and many other edible products. They are very toxic and hazardous for human life and also for the ecosystem. Therefore to remove the organic pollutants nanomaterials are widely used as catalyst to decompose these harmful dyes under visible and UV light [22]. This phenomenon is commonly known as photocatalysis. With the ever-growing dependency of modern human life on industry, photocatalysis has been the focus of significant attention in recent years.

1.5 Chemical Modulation of Valance Band:

Existing TCOs are basically n-type in nature, whereas it is very difficult to prepare binary metal oxides with comparable p-type conductivity. Probably The reason behind this is the electronic structure of these metal oxides. It is well known that in metal oxides, conduction band consists of metallic s orbitals and valance band consists of p orbitals of oxygen. So electrons can easily move in the metallic s orbitals in n-type binary oxide materials. But O 2p orbitals are far lower lying than the valence orbit of metallic atoms and this leads to the formation of deep acceptor level by the holes and r tightly bound. That means there is high probability for the holes to be localized around the high electronegative oxygen atoms. Therefore these holes require relatively high energy to overcome the large barrier height in order to move within the crystal lattice and this results in poor p-type conductivity and hole mobility [23-28].

To overcome this problem a possible solution was proposed by Kawazoe and co-authors introducing 'degree of covalency' in the metal-oxygen bonding to induce the formation of an extended valence band structure, i.e. the valence band edge should be modified by mixing orbitals of appropriate counter cations that have energy-filled-levels comparable to O 2p orbital. This would reduce the strong coulombic force by oxygen ions and thus delocalizing the holes. This is the necessary approach to obtain p-TCO, which is called 'Chemical Modulation of the Valence Band (CMVB)' [23].

For this we need appropriate cationic species for which CMVB technique will be valid. Research work showed that $3d^{10}$ shell of Cu+ and $4d^{10}$ of Ag+ can be the required cationic species. Open d shell can be used for CMVB technique but for TCO we cannot use it due to d-d transition which gives strong coloration. a schematic diagram of CMVB technique is shown in Fig 1.9 below.

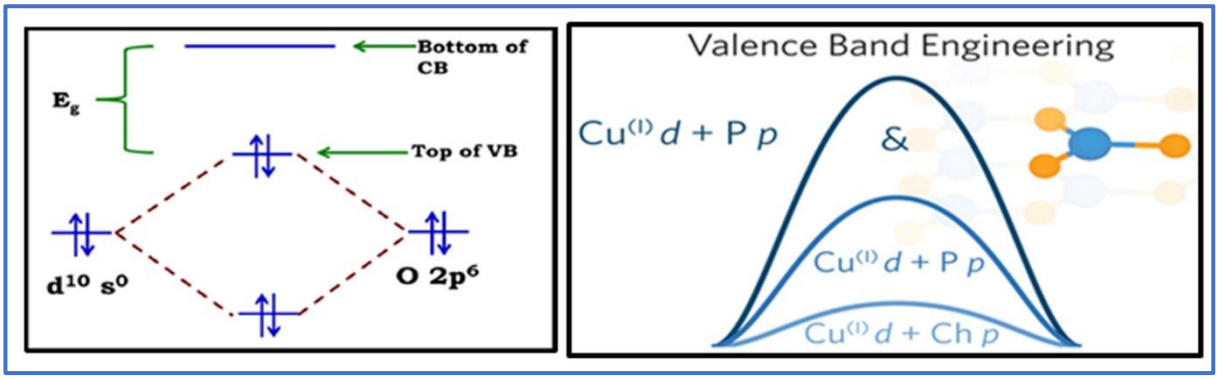

Figure 1.9: Schematic diagram of CMVB

1.6 Structure of copper delafossite:

For designing a p- type TCO structural requirement is of important necessity. Tetrahedral coordination of oxide ions acts in reducing the localization behaviour of 2p electrons on oxide ions [24] and it is beneficial for p-type conductivity One of the possible structures is the delafossite structure which is shown in figure 1.10.

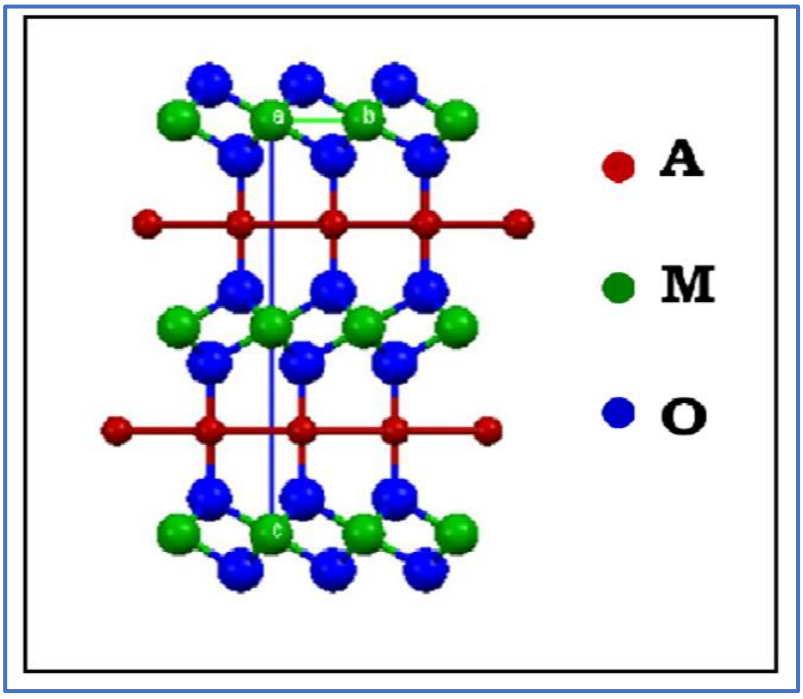

Fig-1.10: Delafossite crystal structure.

Materials with delafossite crystal structure $AM0_2$ (A is monovalent cations, Cu^+ Ag^+; M is trivalent cations, B^{3+}, Al^{3+}, Ga^{3+}, In^{3+}, etc.) [29-31] can be used to design p-TCOs mainly for three reasons.

1) As observed we can see alternate stacking of A and layers of MO_2 which consist MO_6 octahedral sharing edges. Each A atom is coordinated with two oxygen atoms linearly to form a O-A-O dumbbell unit which is parallel to the c axis Oxygen atoms link O-A-O dumbbell layers with the MO_2 layers. Also each oxide ion forms a ,pseudo tetrahedral co-ordination (M_3AO) with the MO_2 layer with the neighboring M and an ion. This configuration delocalizes the holes at the valence band edge to achieve the p-type conductivity [29].

2) Secondly, O-A-O dumbbell layer and MO_2 layer effectively reduces the dimension of crosslinking of A^{+1} ions and, thus enlarging the band gap [23-25].

3) Finally, the most important factor in this structure is the low coordination number of the A+1ions due to the large separation from oxygen legands. This results the strong coulombic repulsion between 2p electrons in oxygen legands and d^{10} electrons in A^{+1} ions. Hence the d^{10} energy levels of A^{+1} ions become almost comparable to the O 2p orbital, resulting in a high degree of mixing of these levels which is essential for CMVB technique [23]. This leads to the delocalization of holes at the valence band edge.

1.7 Introduction of $CuBO_2$:

P-type transparent conductive oxides (TCOs) are one of the important new-age nanomaterials which have proved to be promising candidates for optoelectronic device technology and junction based ‘invisible device’ fabrication. Various nanostructures of p-type TCOs are attracting attention due to their rare combination of excellent novel optical and electrical properties. In 2007 Snure et al. reported a new wide band gap p-type TCO, $CuBO_2$ with high transparency and high room-temperature electrical conductivity 1.65 S/cm.[30] This value of conductivity is 65% higher than that of $CuAlO_2$ reported by Kawazoe et al. Due its $CuBO_2$ is a very new material which is invented just for ten years. So till now research on $CuBO_2$ is in a very preliminary stage globally. There are numerous estimations about the crystal structure of $CuBO_2$ in the published papers reported by several groups. Since now the most acceptable

crystal structure of $CuBO_2$ is delafossite with hexagonal crystal system and lattice parameters a=b=2.84 Å, c=16.52 Å.[30] The unique structure of delafossites fulfils the all requirements for chemical modulation of valance band which is the main driving arrangement for achieving high p-type conductivity theoretical investigation shows that the band gap of $CuMO_2$ should increase with decreases of the ionic radius of M. Boron, which has the smallest ionic radius among the trivalent elements of periodic table, is appropriate for $CuMO_2$ structure. So, according to some theatrical reports $CuBO_2$ should have the largest band gap and hence better transmission characteristics [31- 32]. Cupper Delafossites are usually ternary oxides having unique crystal structure where metal planes and O atoms connected by dumbbell Cu atoms [33] resulting in chemically modulated valance band where the electron pairs of O atoms become delocalized and offers enhanced conductivity. $CuAlO_2$ emerged as the most popular p-type TCO in this field. Several attempts have been made to enhance the conductivity of $CuAlO_2$ and other Cu delafossites by different groups including ours by doping and incorporating defects [34]. Inspite of all those efforts, electrical conductivity of p-type TCOs even for the Cu delafossites is still inferior to n-type TCOs and further research regarding this is urgently required. It has been proved that delafossites of $Cu(M)O_2$ form are expected to exhibit higher band gap as the ionic radius of M decreases. This indicates that $CuBO_2$ should have the largest optical band gap among the Cu delafossites[35]. Undoped $CuBO_2$ also possess very high room temperature electrical conductivity [36] claiming itself a potential candidate for junction fabrication with n-type TCOs. The conductivity of $CuBO_2$ is 1.65 S/cm [37] which is also higher than the other delafossite materials. Transparency of $CuBO_2$ is also high. So from the properties we can choose $CuBO_2$ as a novel material for device application. therefore $CuBO_2$ has become a potential candidate in the field of TCO research.

1.8 Objectives:

The main objectives of this thesis are concerned with the development of successful molten-salt synthesis routes for the production of p-type transparent conducting oxide $CuBO_2$ and sulphur doped $CuBO_2$ nanostructures as well as understanding their various structural, optical, electrical properties.

Some major objectives of this thesis are listed below-

(a) To synthesized pure $CuBO_2$ and sulphur doped $CuBO_2$ nanostructures by simple molten salt route. Also optimized the correct synthesis condition to get desired materials.

(b) Synthesized materials are characterized by some sophisticated tools like X-ray diffractometer (XRD), field emission scanning electron microscope (FESEM), UV-Visible spectrophotometer, TEM, IV measurement instrument etc

(c) Finally determines such applications of as prepared materials in the field likes Field Emission, conductivity and photocatalysis.

References:

[1] N. Taniguchi, \On the Basic Concept of `Nano-Technology' ", Proc. Intl. Conf. Prod. Eng. Tokyo, Part II, Japan Society of Precision Engineering, 1974.

[2] K.E. Drexler, \Engines of Creation", Fourth Estate, London 1990, p. 296.

[3] N. Taniguchi, "On the Basic Concept of 'Nano-Technology'," Proc. Intl. Conf. Prod. Eng. Tokyo, Part II, Japan Society of Precision Engineering, 1974.

[4] G. Binnig et al., Phys. Rev. Lett. 49, 57,(1982).

[5] Smalley, R.E., 1997. Discovering the fullerenes. Reviews of Modern Physics, 69(3), p.723.

[6] K.E. Drexler, Engines of creation: The coming era of nanotechnology, (Oxford University Press, Oxford, 1986); K.E. Drexler, C. Terson, G. Pergamit, Unbounding the Future: The Nanotechnology Revolution (Morrow, New York, 1991); K.E. Drexler, Nanosystems: Molecular Machinery, Manufacturing, and Computation,(Wiley, New York, 1992).

[7] Burda, C., Chen, X., Narayanan, R. and El-Sayed, M.A., 2005.

[8] Nanomaterials – B. Viswanathan, published by Narosa Publishing House.

[9] Deshpande, S., Patil, S., Kuchibhatla, S.V. and Seal, S., 2005. Size dependency variation in lattice parameter and valency states in nanocrystalline cerium oxide. Applied Physics Letters, 87(13).

[10] Anisotropic nanomaterials: structure, growth, assembly, and functions, P. R. Sajanlal, T. S. Sreeprasad, A. K. Samal and T. Pradeep, NANO REVIEWS, vol 2, (2011).

[11] Physical Properties of Nanomaterials, Juh Tzeng Lue, Encyclopedia of Nanoscience and Nanotechnology,Volume X: Pages (1–46).

[12] O. Vigil, F. Cruz, A. Morales-Acevedob, G. Contreras-Puente, Materials Chemistry and Physics 68 (2001) 249–252.

[13] G. Anil Kumar, M. V. Ramana Reddy, KattaNarasimha Reddy, Journal of Physics: Conference Series 365 (2012) 012031.

[14] H. Merzouk,A. Chelouche,S.Saoudi, D. Djouadi, A. Aksas,ApplPhys A (2012) 109:841–844

[15] B. SrinivasaRao, V. Rajagopal Reddy, B. Rajesh Kumar, T. SubbaRao, International Journal of Nanoscience, Vol. 11, No. 3 (2012) 1240006 (5 pages).

[16] SoumenDhara, P. K Giri, Journal of Experimental Nanoscience, 8(2013) 3, 332–340.

[17] C. Suryanarayana, Bull. Mater. Sci., 17 (1994)307.

[18] Nanomaterials –An introduction to synthesis, properties and application, Environmental Engineering and Management Journal, 2008, Vol. 7, No.6, 865-870.

[19] Optical properties and spectroscopy of nanomaterials - Jin Zhng Zhang, published by

World Scientific Publishing Co. Pte. Ltd.

[20] K. Nagaveni, G. Sivalingam, M.S. Hegde, Giridhar Madras, Applied Catalysis B: Environmental 48 (2004) 83–93.

[21] Jialin Li , Li Liu, Ying Yu, Yiwen Tang, Huanlun Li, Feipeng Du, Electrochemistry Communications 6 (2004) 940–943.

[22] K. Ashok, Surf. Rev. Lett., 18, 11 (2011).

[23] Conway, Brian E. Springer Science & Business Media,2013.

[24] H. Kawazoe, M. Yasukawa, H. Hyodo, M. Kurita, H. Yanagi, H. Hosono, Nature 389 (1997)939.

[25] H. Kawazoe, H. Yanagi, K. Ueda, H. Hosono, MRS Bull. August 2000, p. 28.

[26] Hideo Hosono, Thin Solid Films 515 (2007)6000–6014.

[27] S. Fraga, S. Karwowski, K. M. S. Saxena, Handbook of Atomic Data,
Elsevier (1976) Amstardam,pp.259.

[28] D. DeVault, J. Chem. Educ. 21 (1944) 526, 575.

[29] A.N. Banerjee, , K.K. Chattopadhyay, Progress in Crystal Growth and Characterization of Materials, Volume 50, Issues 1–3, 2005, Pages52–105.

[30] M. Snure, A. Tiwari, Appl. Phys. Lett. 91 (2007)092123.

[31] C. T. Prewitt, R. D. Shannon, D. B. Rogers, Inorg. Chem. 10 (1971)719.

[33] H. Kawazoe, M. Yasukawa, H. Hyodo, M. Kurita, H. Yanagi, H. Hosono, Nature 389 (1997) 939.
[34] A.N. Banerjee, R. Maity, P.K. Ghosh, K.K. Chattopadhyay, Thin Solid Films 474 (2005) 261.

[35] M. Snure, A. Tiwari, Appl. Phys. Lett. 91 (2007) 092123.

[36] X. Nie, S.H. Wei, S.B. Zhang, Phys. Rev. Lett. 88 (2002) 066405.

[37] D. B. Rogers, R. D. Shannon, C. T. Prewitt, J. L. Gilson, Inorg. Chem.10 (1971)723.

Chapter 2

Review of Past Work

2.1. General Idea:

We have already discussed about the Importance of semiconductor materials as transparent conducting oxide (TCO) materials especially in their nanostructured forms due to their varieties of applicability in fabrication of nanodevices and junction based nanoelectronics in the last chapter. So it is important to discuss in detail the advance regarding research on these nanostructured materials as reported by other research groups for establishing the perspectives of the problems addressed in this thesis. Oxide nanostructures have been widely studied during last few decades for exploring their application-worthy optical and electrical properties [1]. Advance and Vigorous research work had been carried out on several metal oxides like pure and F doped SnO_2 (FTO), ZnO, pure and doped CdO, CuO, NiO etc.[2-10]. Due to their high electrical conductivity and optical transparency in the visible light transparent conductive oxides like, indium tin oxide, doped zinc oxide and indium molybdenum oxide are used widely as transparent electrodes in a number of applications [11-14]. However, industrial usage of TCO nanostructures are mainly dominated by n-type oxides like SnO_2, ZnO, In_2O_3, etc [15-17] and their p-type counterparts are comparatively less used for these purposes. The reason is p-type TCOs are generally considered to exhibit inferior electrical conductivity compared to the n-types, and thus they are not appropriate candidates to be used in smart applications like "invisible electronics". To advance the use of TCOs in the field of electronics, such as transparent light emitting diodes, UV detectors, solar cells, etc., it is used to develop p-type TCOs with high electrical conductivity and transparency. Doping of n-type oxides sometimes solves the problem partially, but the necessity of development of highly conducting intrinsic p-type TCOs can never be ignored. Kawazoe and his workers had proposed a unique technique which is famous as 'Chemical Modulation of Valance Band' in 1997 to fulfil this requirement [18]. Several p-type ternary oxide materials have been developed whereas $CuBO_2$is a very new addition in this group of materials with this technique proposed. Exploiting the principle of chemical modulation of valence band, several cooper based delafossites were developed having $CuMO_2$ structure with M as Cr, Fe, Ga, Sc, Y, etc [20-21]. Those Cu delafossites and their nanostructures exhibit very high conductivity and appreciable transmittance, fulfilling the criteria of a proper p-type semiconductor opening up new possibilities for fabrication of high figures of merit junction based devices and several other applications like photocatalysis, photodiodes, sensing, etc.

2.2. Some works about traditional delafossites:

Hosono and its co-workers are developing transparent oxide semiconductors: he proposed a material design concept for an transparent amorphous oxide semiconductor (TAOS) with large electron mobility, which is used in next generation display.

Optically transparent oxides tend to be electrical insulators, by virtue of their large electronic bandgap (>3.1 eV). The most notable exceptions are doped versions of the oxides In_2O_3, SnO_2 and ZnO—all n-type (electron) conductors—which are widely used as the transparent electrodes in flat-panel displays [22]. On the other hand, no transparent oxide exhibiting high p-type (hole) conductivity is known to exist, whereas such materials could open the way to a range of novel applications. For example, a combination of the two types of transparent conductor in the form of a p-n junction could lead to a 'functional' window that transmits visible light yet generates electricity in response to the absorption of ultraviolet photons. Here we describe a strategy for identifying oxide materials that should combine p-type conductivity with good optical transparency. Hooson and it's co-workers have illustrated the potential of this approach by reporting the properties of thin films of $CuAlO_2$, a transparent oxide having room-temperature p-type conductivity up to 1 S cm^{-1}. Although the conductivity of our candidate material is significantly lower than that observed for the best n-type conducting oxides, it is sufficient for some applications, and demonstrates that the development of transparent p-type conductors is not an insurmountable goal.

The recent discoveries of several new transparent conducting oxides of n-type and trials [23] to fabricate field-effect transistors from the materials, are in striking contrast with the lack of reports of p-type conducting oxides. The nonexistence of p-type transparent conducting oxides is thought to originate from a general characteristic in the electronic structure of oxides: the strong localization of the upper edge of the valence band to oxide ions. Therefore, any finding of a p-type conducting oxide must include modification of the energy band structure to reduce the localization behaviour, which in turn requires new insight into the relation between electronic structure and properties of oxide materials. In the technological field, finding such a material may open the way to new applications such as ultraviolet-emitting diodes.

First, let us consider the requirements for the major cationic species of candidate oxides if the localization behaviour in the valence band of typical oxides is to be modified. The cationic

species is required to have a closed shell whose energy is almost comparable to those of the 2p levels of oxygen anions. The closed shell valence state is required to avoid coloration due to intra-atomic excitations. The cations we selected are Cu^{+}, Ag^{+} and Au^{+}, which have the electronic configuration $d^{10}s^{0}$. Within the group of cations having the same electronic configuration, the energy of the d^{10} closed shell electrons is highest for these three cations, and is expected to overlap with that of the 2p electrons on oxide ions.

Second structural requirement relates to the bandgap. Direct interaction between d^{10} electrons on neighboring Cu+ ions may reduce the bandgap. As we are currently interested in transparent materials, an approach is needed to enlarge the bandgap so that there is no absorption in the visible. This is effectively done by lowering the dimension of crosslinking of Cu^{+} ions.

The structure of $CuAlO_2$ can be viewed as a layer structure with the sequence Cu–O–Al–O–Cu along the c-axis, and the three-dimensional crosslinking of the Cu^{+} network is reduced to two-dimensional. This may give rise to a larger bandgap for the delafossite than for Cu_2O. Benko and Koffyberg have reported a positive sign of See beck coefficient for a sintered body of the material [24]. However, because of the low conductivity (1:7 3 1023 S cm21) and mobility (< 1 3 1021 cm2 V21 s21), they proposed a hopping mechanism for hole transport.
Mi Zhong. has described the Electronic properties and formation energies of vacancy defects in delafossite $CuAlO_2$ by using “First Principle Density Function Theory”. The introduced vacancy defects enhance the hybridization between O-2p and Cu-3d states, which is good for p-type conductivity.

Many work on $CuAlO_2$ is being done in “Thin Film Lab” Jadavpur University under the guidance of Prof (Dr) Kalyan Kumar Chattopadhyay, which are follows-
In 2009, Nanocrystalline powders of $CuAlO_2$ were synthesized through sol–gel method using nitrate-citrate route and also through solid state reaction method. It has been observed that the particle size prepared by nitrate-citrate technique is less than the particle size prepared by the solid-state reaction method.

In 2010, The effect of antimony doping on the optical and electrical properties of copper aluminium oxide synthesized by solid state reaction technique was investigated. A nonlinear current–voltage characteristic was observed for the Sb-doped $CuAlO_2$ samples whereas the same was linear for the undoped samples.

Thin films of p-type transparent conducting $CuAlO_2$ have been synthesized through reactive radio frequency magnetron sputtering on silicon and glass substrates at substrate temperature 3000C.

In 2012, An ab initio calculation has been carried out to investigate the biaxial strain (-10:71% < "€ < 9:13%) effect on elastic, electronic and optical properties of $CuAlO_2$. All the elastic constants (c11, c12, c13, c33) except c44 decrease (increase) during tensile (compressive) strain. The band gap is found to decrease in the presence of tensile as well as compressive strain. The relative decrease of the band gap is asymmetric with respect to the sign of the strain. From calculations, it is clear that the tensile strain can enhance the hole mobility as well as the transparency of $CuAlO_2$.

In 2013, Modification of orbital interactions by suitable "orbital alloying" is a necessity to obtain direct gap group IIIA delafossite with shallow acceptor states, which unfortunately have never been realized. Dispersion of Cu 3d character by incorporating shallower acceptor (Ch 3p) states is concluded upon analyzing the photoemission spectra of the valence band.

In 2018, $CuBO_2$ nanostructures have been synthesized via sol–gel method. A novel uniform nanonetwork-like structure is obtained and its band gap is found to be 4.24eV. In ultraviolet light irradiation, this as-synthesized sample shows efficient photocatalytic activity for degradation of organic dye Rhodamine B. The degradation efficiency and the rate constant were calculated as ∼70% and 1.32×10^{-3} min^{-1}, respectively.

2.3. $CuBO_2$ as a novel material

$CuBO_2$ belongs to the family of Copper delafossite. It has high p-type electrical conductivity and hole mobility at room temperature [14]. Some theoretical observation predicted that band gaps of delfossite materials have an inverse relationship with the ionic radius of the trivalent cation in the delafossite compound [13]. The only material whose has the lowest ionic radius among the trivalent elements in the periodic table is Boron. So according to the theoretical observation $CuBO_2$ should have the largest band gap among the materials of copper delafossite

family and hence should exhibit better transmittance characteristics in the visible spectra. These observations are also matched with the experimental results [14]. From the above observation, we can see that $CuBO_2$ is a very significant material in the family of TCO and it needs further elaborative research works.

2.4. Different experimental synthesis methods of $CuBO_2$:

A large number of scientific articles demonstrate easy synthesis of Cu-delafossites in high temperature annealing technique using several different sources of the trivalent cations [18-21]. But availability of Boron in natural form is very rare. So Synthesis of $CuBO_2$ by solid state sintering process is not possible for the high vapour pressures of boron oxides. So synthesis of $CuBO_2$ is extremely challenging for the researchers.

Synthesis of $CuBO_2$ was first reported by Snure and Tiwari in 2007 [14]. They employed pulsed laser deposition (PLD) technique for the synthesis of $CuBO_2$ while preparing the bulk target, they used CuO and B_2O_3 as precursor materials. In atypical sol-gel synthesis, Snure et al. dissolved these precursors in nitric acid followed by addition of citric acid in stoichiometric molar ratio to this solution. According to their analysis citric acid worked as chelating agent for binding between one Cu and one B atom. They thereafter refluxed the solution for 12 h to obtain the gel which was annealed further to produce powder. They applied a pressure of 200 MPa to the powder sample to fabricate $CuBO_2$ pellet (target) which was then transferred inside the PLD chamber for laser ablation. For, PLD technique, Snure et al. used the base pressure of 10^{-6} torr and working oxygen pressure 10^{-2} torr, a KrF pulsed excimer laser of wavelength 248 nm and pulse width of 25 ns. They maintained a moderately high substrate temperature of 700 °C while the experiment. Laser energy density and repetition rates were maintained at 3 J/c^2 and 10 Hz, respectively. Finally, they synthesized $CuBO_2$ films of 200 nm thickness on single crystal sapphire (001).

In 2009, another synthesis method of $CuBO_2$ was reported by Zheng and his co-workers[25] In their typical procedure, 50 mL of 0.1 mol/dm^3 $Na_2B_4O_7$, $10H_2O$ aqueous solution and 1mL of 0.002 mol/dm3 phosphate ester were prepared separately and poured into a 500 mL three-neck round-bottom flask equipped with a thermometer and a mechanical stirrer. They added 10 mL of 2 mol/dm3 $CuSO_4 \cdot 5H_2O$ aqueous solution thereafter with this for 0.5 h while being stirred and maintained the same experimental conditions for 7h. After synthesis, they collected the sample and washed the obtained precipitates to remove by-products, and then dried the

same at 60℃ for 8h to obtain the final copper borate powders. They varied the synthesis temperature at 10℃, 30℃, 50℃, 70℃ According to Zheng et al. this synthesis phosphate ester was used as the modifying agent. Another sample was also synthesized without phosphate ester at 70℃ for 7h to observe the effect of the same in this typical synthesis.

In 2013, Chesta Ruttanapun reported the synthesis of $CuBO_2$ delafossite by solid state reaction technique [26] In this synthesis route stoichiometric amounts of CuO and B_20_3 powders were ball milled for 24 h in the presence of alcohol after that the crushed powder was calcined at 1005℃ for 6 hours in air. This synthesized powder was then cooled and pressed into pellets with 12 mm in diameter and 2–3 mm in thickness. These pellets were sintered at 1005 ℃ into an aluminium crucible in air medium. This condition was sustained for 24 h and then rapidly quenched to room temperature and required sample is obtained.

In a latest development in 2014, Soylu et al. synthesized of $CuBO_2$ film using copper (II)-acetate monohydrate and boric acid as precursors [27]. At room temperature acetic acid, ethyleneglycol and dimethylformamide were added to the water solutions of the precursors to obtain the sol. A film of this sol was prepared by spin coating system on cleaned silicon substrate. The obtained coating was dried at 150℃ to obtain a solid film. The solid film of $CuBO_2$ was annealed at 500℃ for 4 h. Al dots were deposited through molybdenum mask with contact area of 3.14 cm2 using thermal evaporation technique. As a result, $CuBO_2$ /p- Si/Al hetero junction was formed.

2.5. Review of detail Characterization Process:

The synthesized $CuBO_2$ was characterized by several techniques to investigate the structural, optical and electrical properties. Snure et al. characterized their samples (pellet and film) by using of XRD and EDX [14]. According to their investigation $CuBO_2$ possesses delafossite structure of R-3mspace group. Additional peaks were reported in the XRD pattern of the bulk pellet which indicates the existence of a small amount of secondary CuO phase in the material, no additional peaks were observed in the XRD pattern of thin film. Three peaks were observed which correspond to (006), (012), and (012) planes of copper delafossite structure. These results indicate the growth tendency of $CuBO_2$ film in (001) orientation. This phenomenon is consistent with earlier observation for other Copper delafossites[29-31] . In this report, Snure et al. estimated values of lattice parameters of $CuBO_2$ films as a=2.84 Å and c=16.52 Å. They also observed the EDAX spectrum of the CuBO2 film and pellet. Only the peaks corresponding to Cu Lα, Cu Kα, Cu Kβ, O Kα, and B Lα were detected. In case of films, additional peak of

Al Lα was observed due to the sapphire substrate. Using all these investigations Snure et al. confirmed the proper phase formation of $CuBO_2$ in thin film form. AFM measurement was used to observe the surface morphology of the synthesized $CuBO_2$ in thin film. The surface of the film consisted of nanoparticles with an average diameter ~25 nm. From the three dimensional rendering, the average roughness of the film was observed to be 20 nm [14].

Zheng et al. investigated some stable weak green powder at room temperature [25]. They are characterized their samples by XRD (SHIMADZU XRD-6000 diffractometer employing Nifiltered Cu Kα radiation, at a scanning rate of $6°min^{-1}$ with 2θ ranging from 10° to 60°) for analysing the phase of the samples. The XRD patterns of the as-synthesized materials indicated that the materials were all in crystalline form. The author reported that the diffraction pattern of samples prepared at 10°C and 30°C were in good agreement with JCPDS files no. 28–1256 ($CuBO_2$). For synthesis temperature at 70°C (for sample prepared with ester) CuB_20_4 was formed which was matched with JCPDS file no. 01–0472. For these three samples characteristic peaks of impurities were not detected but other borates and unreacted compounds were detected. Mixed phase of $CuBO_2$ and CuB_20_4 was formed for reaction temperature at 50°C. The morphology of the samples was observed using a Hitachi scanning electron microscope (SEM) with a field FESEM (JEOL-6700F) and a Hitachi H- 800 TEM. The powders were dispersed in absolute ethanol and ultrasonicated before SEM and TEM characterization. From the SEM image, the morphology of samples prepared at temperature 10°C and 30°C were found to be 1D nanowhiskers with diameters of 100 nm, lengths of 2 μm and spindle shape with diameters of 100–200 nm and lengths of 1 μm respectively. The TEM image of the synthesized materials showed the same morphologies (1 D and 2 D) as characterized in SEM. Selected area electron diffraction (SAED) reported the perfectly single crystalline form of the same. For bonding information of the functional groups, IR spectroscopy of the samples as powder-pressed KBr pellet used a JIR-5500 (JEOL) spectrophotometer at room temperature. From this statement it was investigated that the phosphate ester was not bonded to the surface of copper borate for the synthesis temperature at 10°C, but when the temperature was enhanced from 50°C to 70°C, the bond formed between phosphate ester and copper borate [25].

The authors also suggested a probable growth mechanism of the prepared samples [18]. According to the report presence of the surfactant took a major role to control the surface energy of the nano/microcrystals. Due to ‘selective adhesion’ i.e. stabilization of a certain surface by the surfactant, growth rate varied at different crystallographic planes. At higher temperature control of ‘selective adhesion’ became difficult and there was a dimensional

change in the structure (1D to 2D). For kinetic growth process, the growth rate was exponentially proportional to the surface energy. At lower synthesis temperature, samples obtained were elongated along their own crystallographically high energy directions. The schematic illustration of possible growth mechanisms of this synthesis is shown in figure 2.1.

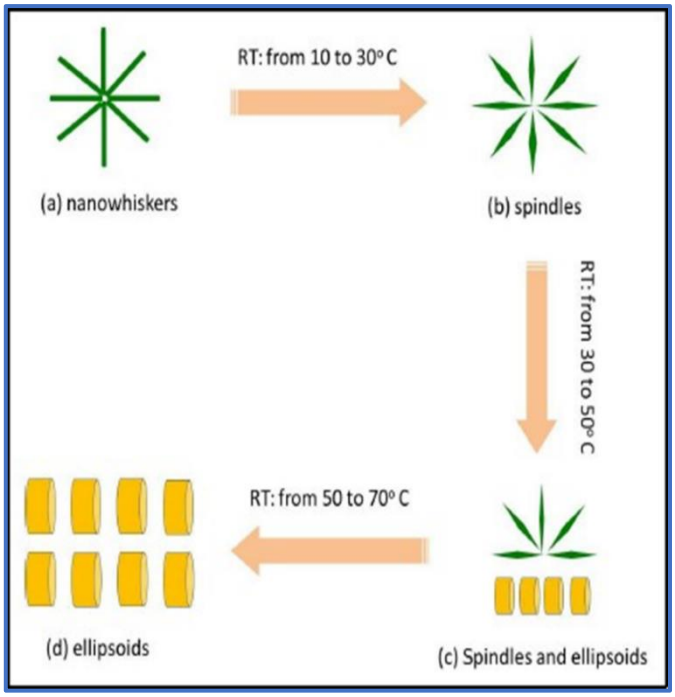

Figure 2.1: Schematic of possible growth mechanism of copper borate nano/microstructure with different morphologies

Ruttanapun confirmed the pure phase formation of $CuBO_2$ by XRD characterization of the synthesized materials [26]. In this report the $CuBO_2$ was also proposed to be of hexagonal delafossite structure (R-3m space group) with lattice parameters a= 2.872 Å and c=16.580 Å. The SEM images showed that the $CuBO_2$ samples consist of micrograins with 1–5 μm diameters. $CuBO_2$ samples were characterized with TGA and DTG analyses and this showed a 10% weight loss in the temperature range 200°C to 1000°C. XPS was used to investigate the valence state and oxidation number of components in $CuBO_2$. The survey spectrum showed Cu, B, and O peaks, with reference to the C1s peak at 285 eV. The binding energies of Cu(2p3/2) and Cu(2p1/2) were found at 933 and 953 eV, respectively with some minor satellites. The B(1s), O(1s) peaks were at 192 eV and 530.8 eV respectively [26].

Soylu et al. characterized the $CuBO_2$ film using XRD and FTIR [20]. They found only two peaks corresponding to (100) and (012) in the XRD spectra. The crystallite size was also determined from this spectrum using Scherrer's equation and it was found to be 44.5 nm. In

FTIR spectra confirmed various bondings like B-O-B, Cu^{2+} O^{-}, $B0_3$ triangles etc. The thickness of $CuBO_2$ film was determined using a XEI software of PARK system Atomic Force Microscopy (AFM) and was found to be 120 nm [20]. The morphology of the $CuBO_2$ film was investigated by SEM. The $CuBO_2$ film was consisted of nanoparticles with different sizes of 70–80 nm and 280–400 nm. The most of particle sizes are in the range of 70–80 nm. The particle size distribution of the film on substrate was not homogeneous.

2.6. Review of Properties and Application of $CuBO_2$:

Snure et al. studied the transmittance spectra of the as-synthesized $CuBO_2$ thin film in the wavelength range 200-900 nm using UV-Vis spectrophotometer [14]. The film showed high optical transparency with transmission value >85% for wavelengths above 550 nm. The indirect and direct band gaps of this film were calculated to be 2.2 and 4.5 eV respectively [14]. They also studied electrical conductivity of $CuBO_2$ film which exhibited a semiconductor like temperature dependence. Room-temperature electrical conductivity of the $CuBO_2$ film was found to be 1.65 S/cm. Hall coefficient measurements showed the film was p-type in nature with carrier density of the order of 1017 cm^{-3} and hall mobility ~100 cm^2 V^{-1} S^{-1} [14]. Positive value of Seebeck coefficient also confirmed the p-type nature of the films.

To study the surface characteristics, Zheng et al. measured the relative contact angle of copper borate samples. The measured contact angle had been increased along with the synthetic temperature increasing i.e. hydrophobicity improved from $CuBO_2$ to $Cu(BO_2)_2$[18]. Ruttanapun reported the absorbance spectra of the $CuBO_2$ sample [23]. The direct gap of this material was calculated to be 3.6 eV. The calculated indirect band gaps were 2.5 eV and 1.9 eV. Two co-operating factors, photon and phonon energy, for transition across the inter band gap ware determined and they were found to be 2.2 eV and 0.3 eV. Fluorescence spectroscopy with emission peak at 355 nm confirmed the direct band type transition of $CuBO_2$. Electrical conductivity of the pellet was measured by using four-probe method and at room temperature it was observed as $4.12*10^{-4}$ S/m which was smaller than that reported by Snure et al [14].The positive value of Seebeck coefficient indicated the p-type nature of the sample. In the temperature range of 650 to 830 K Seebeck values were found to be 450 μV/K to 950 μV/K and thermal conductivities were measured to be $1.4*10^{-4}$ to $5.3*10^{-5}$ W/m- K2 within the same temperature values. The maximum values of power factor and dimensionless figure of merit were 5.3*10-3 W/m-K^2 and 0.0016, respectively, at 960 K. The experimental results of electrical resistivity exhibited results of 0.004 S/cm to 0.038 S/cm within the said temperature

range [26].

Soylu et al. observed the transmission and absorbance spectra for $CuBO_2$ film by using UV vis–NIR spectrophotometer [20]. The sample showed high transparency >80% at 1200 nm wavelength. The direct band gap of the $CuBO_2$ thin film was calculated from the transmission spectrum and it was found to be 3.94 eV. Soylu et al. developed a new rectifying structure $CuBO_2$/p-Si diode with photo sensing property [27]. It showed significant efficiency for producing high voltage protection circuit in electronic application. They also observed that the photocurrent in the reverse bias I–V characteristic is strongly enhanced due to photoillumination. They claimed that combination of thin $CuBO_2$ layer and p-Si has provided high voltage protection level, which does not develop in conventional Si diodes [27]. Some important published papers about the synthesized $CuBO_2$ samples is summarized in the below table 2.1.

Publishing Year	Research Group	Synthesis Route	Morphology	Direct Band Gap (eV)	Indirect Band Gap (eV)	Electrical conductivity at room temperature
2007	Snure et al.14	Pulsed laser deposition	Thin film (20 nm)	4.5	2.2	1.65 S/cm
2009	Zheng et al.18	A typical method	**1D** Nanowhiskers with (Diameters **100** nm. Length ~**2** µm.) and spindle shape (Diameters**100** -**200** nm. Lengths ~**1**µm.)	-	-	-
2013	Ruttanapun et ai.19	Solid state reaction	Micrograins with **1-5** µm. diameters	3.6	2.5 and 1.9	4.12*10-4 S/m
2014	Soylu et al.20	Sol-spin coating	Film with particle size ~**70-80** nm.	3.94		

Table 2.1: Summarized information of different experimental synthesis procedure of $CuBO_2$

References

[1] Jebril, S.; Kuhlmann, H.; Muller, S.; Ronning, C.; Kienle, L.;Duppel, V.; Mishra, Y. K.; Adelung, R. Cryst. Growth Des. 2010, 10, 2842−2846.

[2] R. G. Gordon, MRS Bull. 25 (2000)52

[3] A. N. Banerjee, S. Kundoo, P. Saha and K. K. Chattopadhyay, J. Sol Gel Sci. Technol. 28 (2003)105

[4] S. Major, A. Banerjee and K. L. Chopra, Thin Solid Films 122 (1984)31

[5] J. Hu and R. G. Gordon, J. Appl. Phys. 72 (1992)5381

[6] T. Minami, H. Nanto and S. Takata, Jpn. J. Appl. Phys., Part 2: Lett. 23 (1984)L280

[7] W. O. Lytle and A. E. Junge, U.S. Patent No. 2,566,346,(1951)

[8] R. Groth, Phys. Status. Solidi 14 (1966)69

[9] S. E. Dali, M. Jayachandran and M. J. Chockalingam, J. Mater. Sci. Lett.18

[10] J. L. Vossen, RCA Rev. 32 (1971) 269

[11] S. J. Pearton, D. P. Norton, K. Ip, Y. W. Heo, and T. Steiner, Prog. Mater. Sci. 50, 293 (2005)

[12] M. Snure and A. Tiwari, J. Appl. Phys. 101, 124912(2007)

[13] B. Kumar, H. Gong, and R. Akkipeddi, J. Appl. Phys. 98, 073703(2005)

[14] Michael Snure, AshutoshTiwari, App. Phys. Lett. **91**, 092123(2007)

[15] Yang, B.; Kumar, A.; Zhang, H.; Feng, P.; Katiyar, R. S.; Wang,Z. J. Phys. D: Appl. Phys. 2009, 42, 045415/1−5.

[16] Tiwari, A.; Snure, M. J. Nanosci. Nanotechnol. 2008, 8, 3981−3987.

[17] Mazumder, N.; Sen, D.; Saha, S.; Ghorai, U. K.; Das, N. S.; Chattopadhyay, K. K. J. Phys. Chem. C 2013, 117, 6454−6461.

[18] Jeong, J. A.; Jeon, Y. J.; Kim, S. S.; Kim, B. K.; Chung, K. B. Sol. Energy Mater. Sol. Cells 2014, 122, 241−250.

[19] (a) Hiroshi Yanagi, Shin-ichiro Inoue, Kazushige Ueda, Hiroshi Kawazoe, Hideo Hosono, and NoriakiHamada,Journal of Applied Physics **88**, 4159 (2000); (b) H. Kawazoe, M.Yasukawa,H.Hyodo,M.Kurita,H.Yanagi,andH.Hosono,Nature**389**,939(1997)(c) K. Ueda, T. Hase, H. Yanagi, H. Kawazoe, H. Hosono, H. Ohta, M. Orita, and M. Hirano, J. Appl. Phys. **89**, 1790 (2001); (d) H. Yangi, T. Hase, S. Ibuki, K. Ueda, and H. Hosono, Appl. Phys. Lett.**78**, 1583 (2001)

[20] Varadarajan, V.; Norton, D. P. Appl. Phys. A: Mater. Sci. Process. 2006, 85, 117−120.

[21] Trari, M.; Bouguelia, A.; Bessekhouad, Y. Sol. Energy Mater. Sol. C 2006, 90, 190−202.

[22] Hamberg, I. & Granqvist, C. G. Evaporated Sn-doped In2O3 films: basic optical properties and applications to energy-efficient windows. *J. Appl. Phys.* **60,** R123–R159 (1986).

[23] Seager, C. H., McIntyre, D. C.,Warren,W. L. & Tuttle, B. A. Charge trapping and device behavior in ferroelectric memories. *Appl. Phys. Lett.* **68,** 2660–2662 (1996).

[24] Benko, F. A. & Koffyberg, F. P. Opto-Electronic Properties of CuAlO2. *J. Phys. Chem. Solids* **45,** 57–59 (1984).

[25] YunhuiZheng, Zichen Wang, YumeiTian, YuningQu, Shengli Li, Dongmin An, Xue Chen, Shuang Guan, Colloids and Surfaces A: Physicochem. Eng. Aspects 349 (2009) 156–161

[26] ChestaRuttanapun, J. Appl. Phys. 114, 113108(2013)

[27] M. Soylu, Ahmed A. Al-Ghamdi, Saad Bin Omran, F. Yakuphanoglu, Journal of Alloys and Compounds 617 (2014)602–608

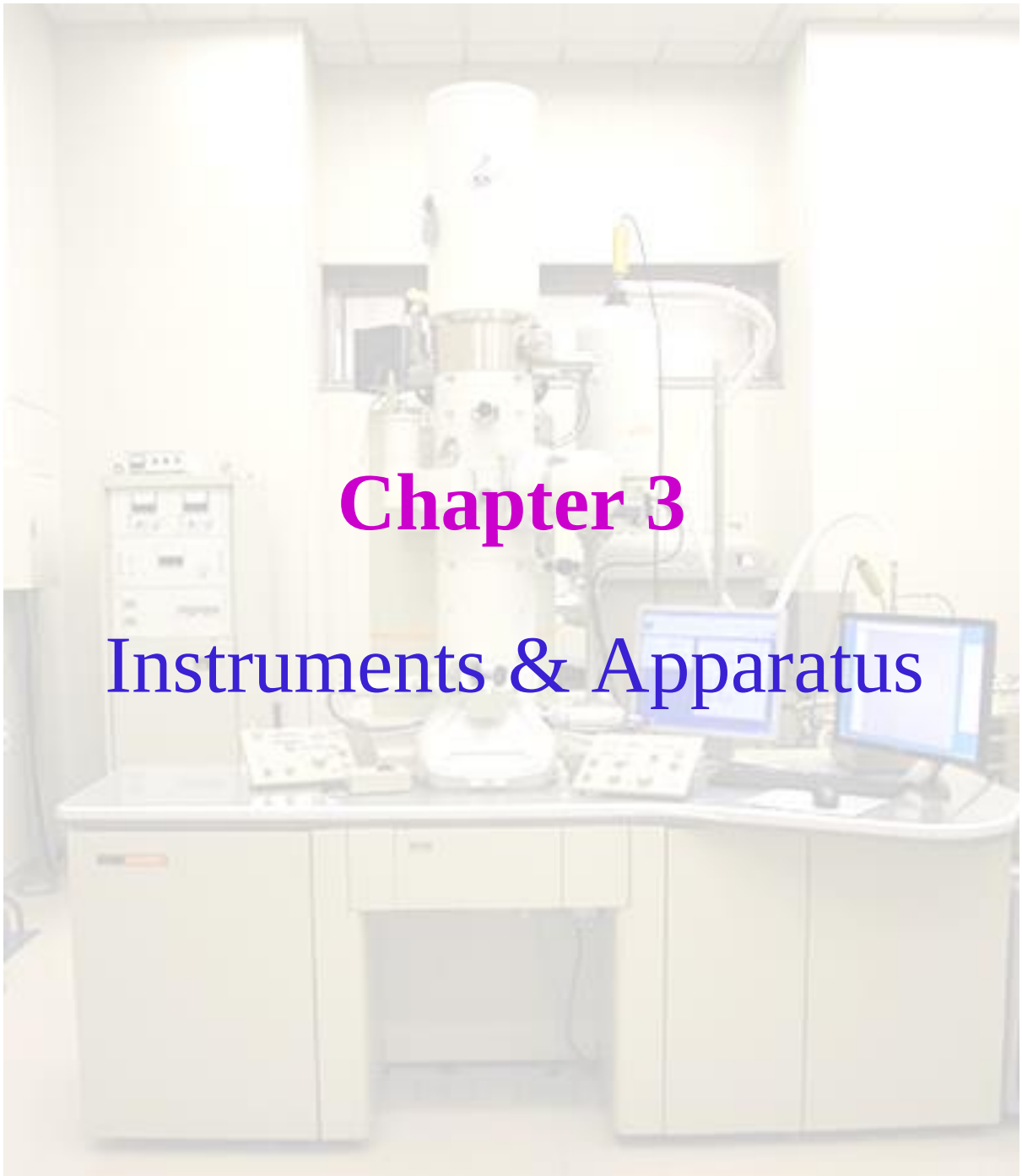

Chapter 3

Instruments & Apparatus

3.1 Major Synthesis Apparatus:

3.1.1. Furnace and Oven:

Box furnaces are commonly used for solid state heating. Starting materials are stoichiometrically mixed and annealed in the furnace within the temperature range of 1000 – 1200 0C for 15 – 20 h. Thorough intermediate grinding is an important step for phase uniformity. Synthesis of $CuBO_2$ nanorods through molten salt process have done in blue box-Furnace at 8000^{o}c for 3 hours. Alumina boats and crucibles or plain Borosil glass beaker was used for the reaction chamber. The temperature controller usually controls the rate of heating and maintains the temperature with an accuracy of ±0.5^{o}c. Fig.3.1 (a) and (c) shows the digital image of the furnace used. A low temperature oven was used for drying the samples and also for certain hydrothermal reactions. The digital image of a typical oven is shown in Fig.3.1 (b).

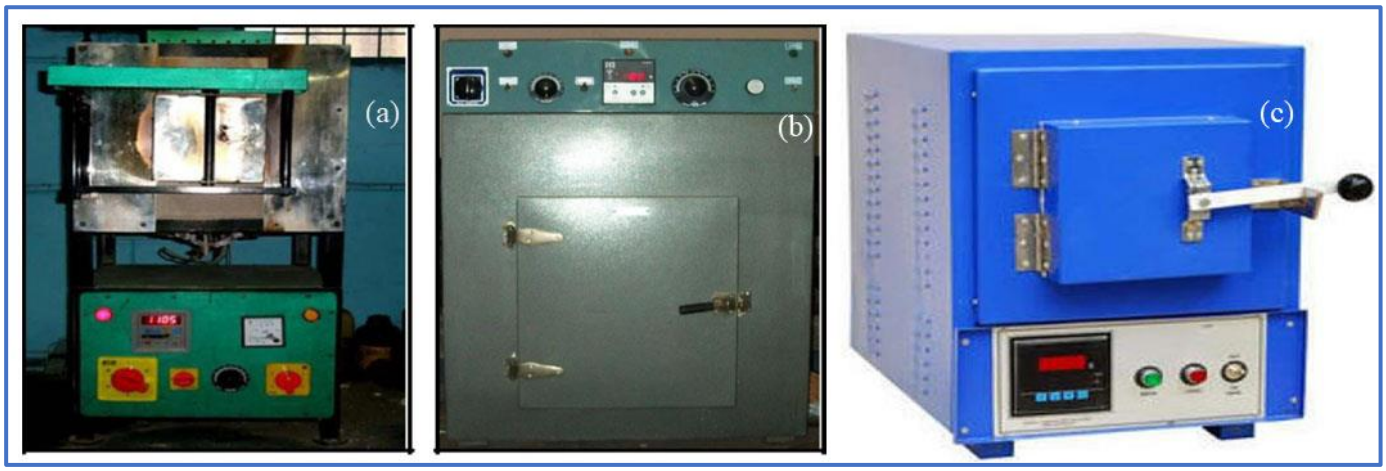

Fig.3.1: Digital images of (a) Furnace and (b) Oven (c) Blue box furnace

3.1.2. Pelletizer:

Pelletizing is an important sample preparation technique, which involves the formation of a solid 'pellet' for analysis via methods that require flat, round samples. The pellets are formed via the agglomeration of fine, amorphous powders in the presence of moisture in a piece of apparatus known as a pelletizer. A solid or liquid binder can also be added before and during pelletizing if needed for process considerations or increasing the hardness of the product. Most common method is the potassium bromide (KBr) pellet method, in which the sample is well mixed with fine alkali halide powder and finely pulverized. The pulverized sample is then fed

into a pellet-forming die when applies a vacuum force on the sample to form transparent pellets. In addition to KBr, cesium iodide may also be used to form pellets. To prepare the pellets we have used a binder because in absence of binder the pellets were found to be very brittle. We have used polyvinyl alcohol (PVA) as the binding agent. In another way To prepare the paste, suitable amount of PVA is mixed with deionized water and is mildly heated with constant stirring until an adhesive gel is formed. One or two drops of this paste are mixed with the oxide powder by a mortar and pestle. Then the powder is pressed into thick films of 12 mm diameter and about 1.5 – 2 mm of thickness under the uniaxial pressure of 1 GPa for 3 min using the pelletizer. The pellets are then sintered at 400 ºC for 3 h to expel the PVA from the sample. Pellets are then connected with electrical contacts to perform characterizations.

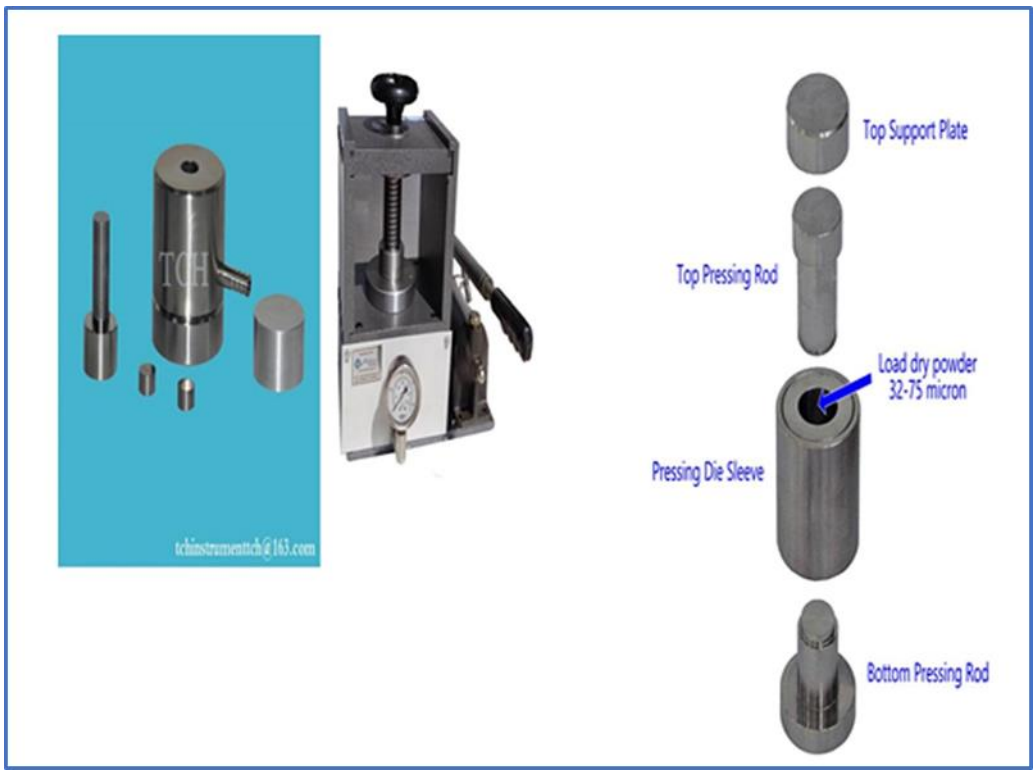

Figure 3.2. Different components of Pelletizer

3.1.3. Magnetic Stirrer:

The magnetic stirrer can stir the magnetic bit within the solution of the beaker through a revolving magnetic arrangement attached with it. A heater arrangement associated with the stirrer can heat the solution at a desired temperature and the temperature is controlled by a knob as shown in Fig.3.3.

Figure 3.3. Digital image of a magnetic stirrer

3.1.4. Spin coater:

Spin Coating is a procedure used to deposit thin films on flat substrates. Thin films of various thicknesses (μm to nm range) can be deposited on the substrate depending on the rotational velocity of the machine and viscosity of the fluid being deposited. In this process, the solution is first deposited on the substrate, and the substrate is then accelerated quickly to the desired rotational velocity. The liquid on the substrate flows out radially, due to the

centrifugal forces acting on it, and the excess is ejected off the edge of the substrate. The film continues to thin slowly until disjointing pressure effects causes the film to reach an equilibrium thickness or it turns solid like due to a dramatic rise in viscosity from solvent

evaporation. The final thinning of the film is then due to solvent evaporation.

Figure 3.4. the model of the spin coaters at Thin Film and Nano Science Lab, JU, manufactured by Apex Instruments

3.1.5. Hot Plate:

A hot plate is a tabletop laboratory heater that is generally used to heat glassware and its contents. This apparatus usually features two or more electric heating elements. Most hot plates also contain magnetic stirrers that allow the heated liquid to be stirred simultaneously and automatically. There are a couple of methods other than direct heating that are also used in the laboratory for experimental purposes. One method of heating is to suspend the slightly above the surface of the hot plate with no direct contact. This reduces the temperature of the glass, slows down the rate of heat exchange and encourages even heating. This works well for low boiling point operations. Another method is to suspend glassware above a plate and surround the flask by a skirt of tinfoil. The skirt should start at the neck of the flask and drape down to the surface of the plate, not touching the sides of the flask, but covering the majority of the plates surface. This method is for glassware to be heated at higher temperatures because the flask is warmed indirectly by the hot air collecting under the skirt and unlike simply suspending the glassware, this method is better protected from drafts.

3.2. Characterization Apparatus:

3.2.1. X–Ray diffractometer (XRD):

In the year 1895, the German physicist Roentgen discovered X-rays and so named due to the unknown nature at that time. These rays were invisible, traveled in straight lines and affected the photographic plate like ordinary light. Also, these rays show more penetrating power than light. In the year 1912, the exact nature of X-rays and diffraction phenomenon of x-rays by atomic planes of crystals were properly discovered. This discovery showed the wave nature of X-rays and explored a new direction to investigate the structure of matter. Solid matter can be divided as follows:

- Amorphous: The atoms are arranged in a random way similar to the disorder we find in a liquid. Glasses are amorphous materials.

- Crystalline: The atoms are arranged in a regular pattern, and one smallest volume element that by repetition in three dimensions describe the crystal. This smallest volume element is called a unit cell. The dimensions of the unit cell are described by three axes: a, b, c and the angles between them alpha (α), beta (β), gamma (γ). About 95% of all solids can be described as crystalline. X-rays are electromagnetic radiation of almost same nature as light but having shorter wavelength of 0.5 to 2.5 Å regions. X-rays occupy the region between gamma and ultraviolet rays in the entire spectrum.

X−rays are generated in a cathode ray tube by heating a filament to produce electrons, accelerating the electrons toward a target by applying a voltage, and bombarding the target material with electrons. When electrons have sufficient energy to dislodge inner shell electrons of the target material, characteristic X−ray spectra are produced. These spectra consist of several components, the most common being Kα and Kβ. Kα consists, in part, of $K\alpha_1$ and $K\alpha_2$. $K\alpha_1$ has a slightly shorter wavelength and twice the intensity as $K\alpha_2$. The specific wavelengths are characteristic of the target material (Cu, Fe, Mo, Cr). Filtering, by foils or crystal

monochrometers, is required to produce monochromatic X−rays needed for diffraction. $K\alpha_1$ and $K\alpha_2$ are sufficiently close in wavelength such that a weighted average of the two is used.

X-rays are electromagnetic radiation of almost same nature as light but having shorter wavelength of 0.5 to 2.5 Å regions. X-rays occupy the region between gamma and ultraviolet rays in the entire spectrum.

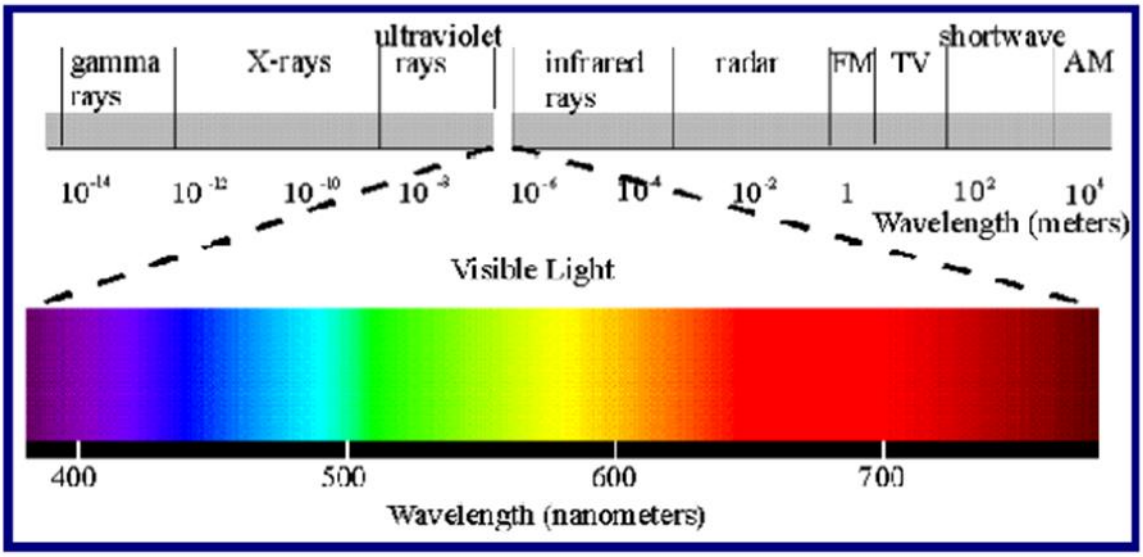

Figure 3.5: Illustration of electromagnetic spectrum

Diffraction is a scattering phenomenon in which a large number of atoms participate and act as scattering center. X-rays scattered by the atoms which are periodically arranged in the lattice, have definite phase relationship in between them. In some scattering direction, destructive interference takes place but in few directions, constructive interference occurs and forms the diffracted beam. **"A diffracted beammay be defined as a beam composed of a large number of scattered rays mutuallyreinforcing oneanother."**

- **Working Principle:**

In XRD, a collimeter beam of X-rays is incident on a specimen and is diffracted by the crystalline phases in the specimen. Using Bragg equation for first order diffraction, lattice spacing may be found from the diffraction angles. Bragg's law is the basic law which governs the X-ray diffraction technique of structural analysis. In Bragg's law, the interaction between x-rays and the electrons of the atoms is described as a process of reflection of x-rays by the atomic planes. When mono chromatic x-rays incident on the atoms in the crystal lattice, atomic

planes allow a part of x-rays to pass through and reflect the other part, there exist a path difference in between the reflected rays from plane 1 and plane 2. These rays will reinforce each other, only when this path difference is equal to an integral multiple of the wavelength.

The ***Bragg's law*** can be written as:

$2d\sin\theta = n\lambda$

Where **n** is an integer and **λ** is the wavelength of the x-rays used, **θ** is Bragg angle and **d** is the interplanar spacing.

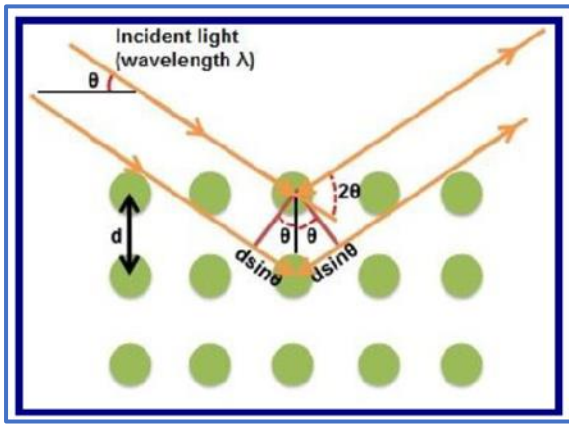

Fig 3.6: Illustration of bragg's law of Diffractometer

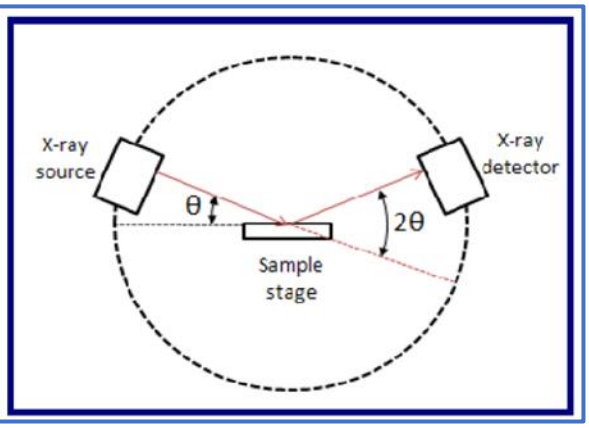

Fig 3.7: Schematic of X-Ray

- **Applications:**

a) Measurement of interplanar spacing between two atomicplanes.

b) Determination of orientation of singlecrystal.

c) Determination of crystal structure for an unknownmaterial.

d) Measurement of particle size, phase and internal stressetc.

A RigakuUltima III X-ray diffractometer was used for recording the diffraction pattern of the samples in θ-2θ configuration with Cu Kα radiation (λ =1.5404 Å) operated at 40 KV voltage and 30 mA current. A photographic image of X-ray diffractometer is shown in **Fig 3.8**

Figure 3.8: Experimental set up of X-Ray Diffractometer

3.2.2. Field Emission Scanning Electron Microscope (FESEM):

An FESEM is microscope instead of light it works with electrons, liberated by a field emission source.

1. **Principle:**

Under vacuum, electrons generated by a Field Emission Source are accelerated in afield gradient. The beam passes through Electromagnetic Lenses, focusing onto the specimen. As result of this bombardment different types of electrons are emitted from the specimen. A detector catches the secondary electrons and an image of the sample surface is constructed by comparing the intensity of these secondary electrons to the scanning primary electron beam. Finally the image is displayed on a monitor. A FESEM is used to visualize very small topographic details on the surface or entire or fractioned objects. Researchers in biology, chemistry and physics apply this technique to observe structures that may be a ssmall as 1 nanometer (= billion of a millimeter). The FESEM may be employed for example to study organelles and DNA material in cells, synthetical polymers, and coatings on microchips.

2. Preparation:

In order to be observed with a SEM objects are first made conductive for current. This is done by coating them with an extremely thin layer (1.5 - 3.0 nm) of gold or gold palladium. Further on, objects must be able to sustain the high vacuum and should not alter the vacuum, for example by losing water molecules or gasses. Metals, polymers and crystals are usually little problematic and keep their structure in the SEM. Biological material, however, requires a prefixation, e.g. with cold slush nitrogen (cryo-fixation) or with chemical compounds. This particular microscope is for seen of a special cryo-unit where frozen objects can be fractured and coated for direct observation in the FESEM. Chemically fixed material needs first to be washed and dried below the critical point to avoid damage of the fine structures due to surface tension. Coating is then performed in a separate device.

Source of electrons:

In standard electron microscopes electrons are mostly generated by heating a tungsten filament by means of a current to a temperature of about 2800°C. Sometimes electrons are produced by a crystal of lanthanum hexaboride (LaB_6) that is mounted on a tungsten filament. This modification results in a higher electron density in the beam 81 and abetter resolution than with the conventional device. In a field emission (FE) scanning electron microscope no heating but a so-called "cold" source is employed. An extremely thin and sharp tungsten needle (tip diameter 10^{-7} –10^{-8} m) functions as a cathode in front of a primary and secondary anode. The voltage between cathode and anode is in the order of magnitude of 0.5 to 30 KV. Because the electron beam produced by the FE source is about1000 times smaller than in a standard microscope, the image quality is markedly better. As field emission necessitates an extreme Vacuum (10^{-8} Torr) in the column of the microscope, a device is present that regularly decontaminates the electron source by a current flash. In contrast to a conventional tungsten filament, a FE tip last theoretically for a lifetime, provided the vacuum is maintained stable.

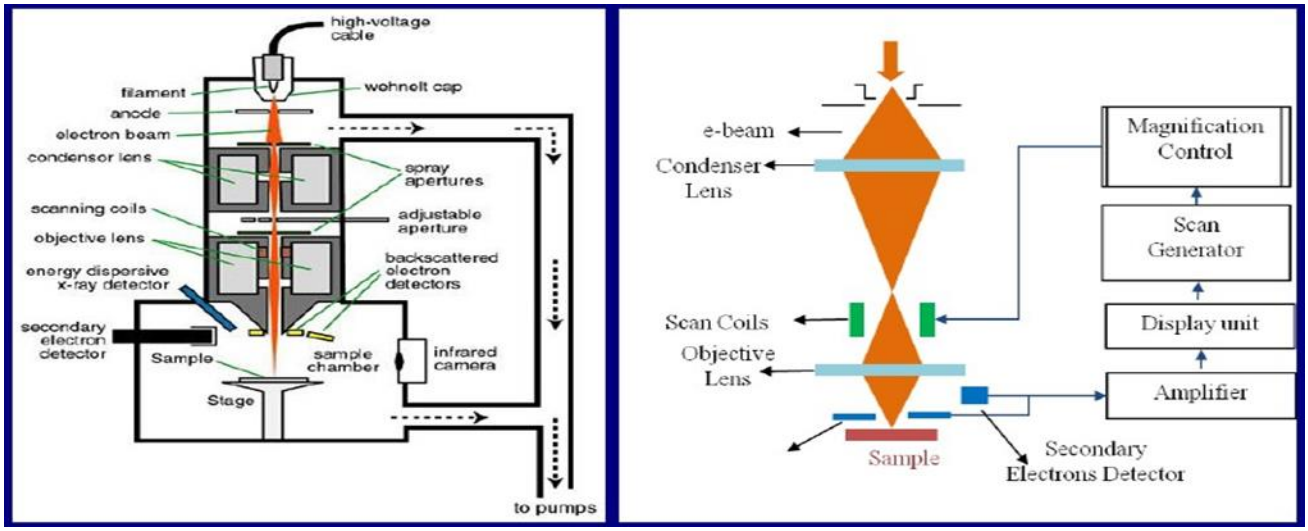

Fig 3.9 Configuration of FESEM and its different components

- **Condenser lens:**

The current in the condenser determines the diameter of the beam: a low current results in a small diameter, a higher current in a larger beam. A narrow beam has the advantage that the resolution is better, but the disadvantage that the signal to noise ratio is worse. The situation is reversed when the beam has a large diameter. The condenser lens is consist mostly out of two parts.

- **Scan coils:**

The scan coils deflect the electron beam over the object according to a zigzag pattern. The formation of the image on the monitor occurs in synchrony with this scan movement. The scan velocity determines the refreshing rate on the screen and the amount of noise in the image. Scan coils often consist of upper and lower coils, which prevent the formation of a circular shadow at low magnification.

- **The objective lens:**

The objective lens is the lowest lens in the column. The objective focuses the electron beam on the object (see FOCUS in the virtual FESEM). At a short working distance(= object in a higher position, that is closer to the objective lens) the objective lens needs to apply a greater force to deflect the electron beam. The shortest working distance produces the smallest beam diameter, the best resolution, but also the poorest depth of field. (The depth of field indicates which range in vertical direction in the object can still be visualized sharply).

- **The stigmator coils:**

The stigmator coils are utilized to correct irregularities in the x and y deflection of the beam and thus to obtain a perfectly round-shaped beam. When the beam is not circular, but

ellipsoidal, the image looks blurred and stretched (see ALIGN X Y in the virtual FESEM).

- **Object chamber:**

After the object has been covered by a conductive layer (see preparation) it is mounted on a special holder. The object is inserted through an exchange chamber into the high vacuum part of the microscope and anchored on a moveable stage. In the virtual FESEM the object can be moved in horizontal and vertical direction on the screen by operating the arrows in the POSITION box. In the real microscope the object can be repositioned in the chamber by means of a joy stick that steers in left right axis, or forward and backward. In addition, the object can be tilted (e.g. for stereo views), rotated and moved in Z direction (= closer or further away to the Objective lens). The "secondary electron emission" detector (scintillator) is located at the rear of the object holder in the chamber.

- **Image formation:**

When the primary probe bombards the object, secondary electrons are emitted from the object surface with a certain velocity that is determined by the levels and angles at the surface of the object. The secondary electrons, which are attracted by the Corona, strike the scintillator (fluorescing mirror) that produces photons. The location and intensity of illumination of the mirror vary depending on the properties of the secondary electrons. The signal produced by the scintillator is amplified and transduced to a video signal that is fed to a cathode ray tube in synchrony with the scan movement of the electron beam. The contrast in the "real time" image that appears on the screen reflects the structure on the surface of the object. Parallel to the analog image, a digital image is generated which can be further processed.

Fig 3.10 FESEM (Hitachi S-4800) SET UP

3.2.3. Ultraviolet Visible Spectrophotometer:

UV spectroscopy is type of absorption spectroscopy in which light of ultra violet region (200-400 nm) is absorbed by the molecule. Absorption of the ultraviolet radiations results in the excitation of the electrons from the ground state to higher energy state. The energy of the ultraviolet radiation that are absorbed is equal to the energy difference between the ground state and higher energy states ($\Delta E = h\upsilon$).

There are two laws that govern the absorption of light by a medium, known as Lambert's law and Beer's law. Lambert's law predicts that the absorbance is directly proportional to the thickness/path length of the medium. Beer's law explains the effect of concentration of colored components in solution on light transmission or absorption. By combining of these two laws, we get Lambert- Beer's law which is as follows:

$$\log (I_0/I_t) = A = \alpha cd$$

Where, A denotes absorbance, α denotes molar absorptivity, c is concentration and d is path length. From the Lambert-Beer's law it is clear that greater the number of molecules capable of absorbing light of a given wavelength, the greater the extent of light absorption. That is the basic principle of UV spectroscopy.

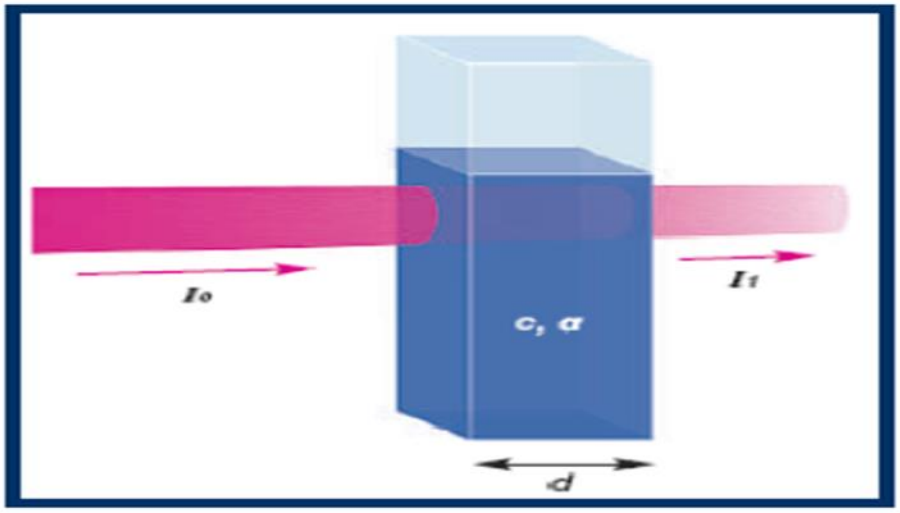

Fig 3.11: Lambert-Beer's law

- **Configuration of instrument:**

A spectrophotometer is an instrument which measures the transmittance or absorbance of a sample as a function of the wavelength of electromagnetic radiation. The main components of a spectrophotometer are:

1. Source
2. Monochromator
3. Sample container
4. Detectors

1. **Source:**

The ideal light source would yield a constant intensity over all wavelengths with low noise and long-term stability. Unfortunately, however, such a source does not exist. Two sources are commonly used in UV-visible spectrophotometers. Theelectrical excitation of deuterium or hydrogen at low pressure produces acontinuous UV spectrum. The mechanism for this involves formation of an excitedmolecular species, which breaks up to give two atomic species and an ultravioletphoton. This can be shown as;

$$D_2 + \text{electrical energy} \rightarrow D_2^* \rightarrow D' + D'' + hv$$

Deuterium lamps emit radiation in the range 160-375 nm. Quartz windows must be used in these lamps, and quartz cuvettes must be used, because glass absorbs radiation of wavelengths less than 350 nm. The tungsten filament lamp is commonly employed as a source of visible

light. This type of lamp is used in the wavelength range of 350-2500 nm.

1. **Monochromator:**

All monochromators contain certain components like entrance slit, collimating mirrors, dispersing device (usually a prism or a grating), focusing mirrors and exit slit.Polychromatic radiation (radiation of more than onewavelength) enters the monochromator through the entrance slit. The beam iscollimated, and then strikes the dispersing element at an angle. The beam is split intoits component wavelengths by the grating or prism. By moving the dispersing elementor the exit slit, radiation of only a particular wavelength leaves the monochromatorthrough the exit slit.

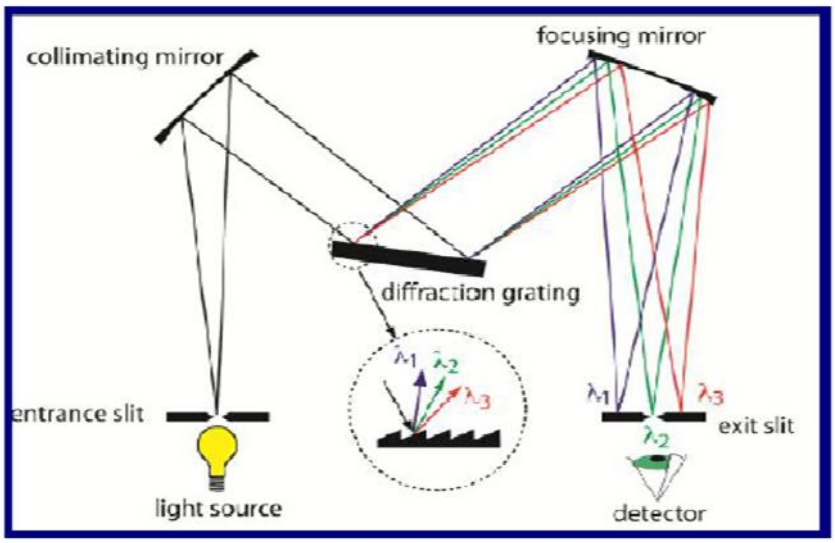

Fig 3.12: Constructions of monochromator

1. **Sample container:**

The containers (***cuvettes***) for the sample and reference solution must be transparent to the radiation which will pass through them. Quartz or fused silica cuvettes are required for spectroscopy in the UV region. These cells are also transparent in the visible region.

2. **Detector:**

A detector converts a light signal into an electrical signal. The photomultiplier tube is commonly used detector in UV-Vis spectroscopy. It consists of *photo emissive cathode* (a

cathode which emits electrons when struck by photons of radiation), several *dynodes* (which emit several electrons for each electron striking them) and an *anode*. Another type of detector is linear photodiode array which is an example of a *multichannel photon detector*. These detectors are capable of measuring all elements of a beam of dispersed radiation simultaneously. Photodiode arrays are complex devices but, because they are solid state, have high reliability.

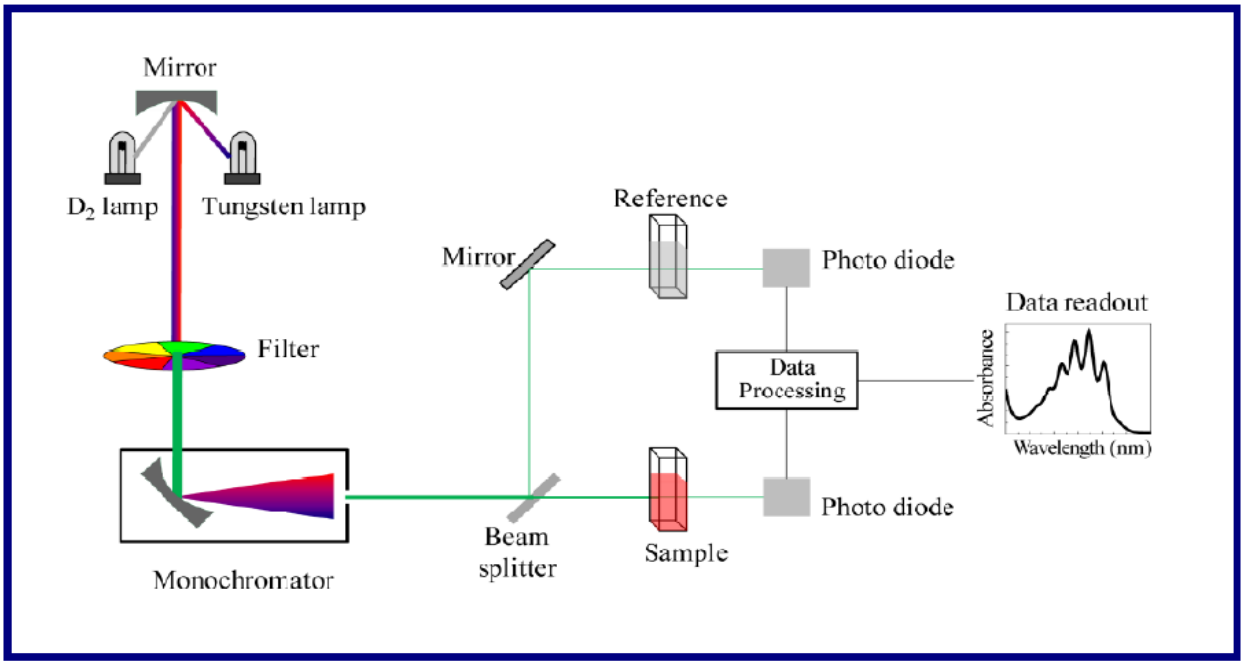

Fig 3.13: Configuration of UV-Visible spectrophotometer.

Fig 3.14: Experimental set up of UV-Visible spectrophotometer.

3.2.4. Energy Dispersive Analysis of X−rays (EDAX):

- **Basic Principle:**

EDAX is an analytical technique used for elemental analysis or chemical characterization of a sample. It is based on the investigation of a sample through interactions between electromagnetic radiation and matter, analyzing X−rays emitted by the matter in response to being hit with the electromagnetic radiation. Its characterization capabilities are due in large part to the fundamental principle that each element has a unique atomic structure allowing X−rays that are characteristic of an element's atomic structure to be identified uniquely from each other.

To stimulate the emission of characteristic X−rays from a specimen, a high energy beam of charged particles such as electrons or a beam of X−rays, is focused with the sample being studied. At rest, an atom within the sample contains ground state (or unexcited) electrons in discrete energy levels or electron shells bound to the nucleus. The incident beam may excite an electron in an inner shell, ejecting it from the shell while creating an electron hole where the electron was. A position vacated by an ejected inner shell electron is eventually occupied by a higher energy electron from an outer shell and the difference in energy between the higher energy shell and the lower energy shell may be released in the form of an X−ray. The amount of energy released by the transferring electron depends on which shell it is transferring from, as well as which shell it is transferring to. The number and energy of the X−rays emitted from a specimen can be measured by an energy dispersive spectrometer. As the energy of the X−ray is characteristic of the difference in energy between the two shells, and of the atomic structure of the element from which they were emitted, this allows the elemental composition of the specimen to be measured.

- **Experimental Set Up:**

An experimental arrangement of EDAX attached to an SEM. It consists of four primary components:

1.Beam source

2. X−ray detector

3. Pulse processor

4. Analyzer

EDAX systems are most commonly found on scanning electron microscopes and electron microprobes. Scanning electron microscopes are equipped with a cathode and magnetic lenses to create and focus a beam of electrons. The energy of the electron beam has to be selected to give a compromise between the requirements of resolution and X−ray production efficiency. The X−radiation excited in the specimen was analyzed in two fully focusing crystal spectrometers. The EDS X−ray detector measures the relative abundance of emitted X−rays versus their energy. The detector is typically lithium drifted silicon, solid state device. When an incident X−ray strikes the detector, it creates a charge pulse that is proportional to the energy of X−ray. The charge pulse is converted to a voltage pulse by a charge−sensitive preamplifier. The signal is then sent to a multichannel analyzer where the pulses are sorted by voltage. The energy, as determined from the voltage measurement, for each incident X−ray is sent to a computer for display and further data evaluation. The spectrum of X−ray energy versus counts is evaluated to determine the elemental composition of the sample volume.

Elements of low atomic number are difficult to detect by EDAX. The Si (Li) detector is often protected by a Beryllium (Be) window. The absorption of the soft X−rays by the Be precludes the detection of elements below an atomic number of 11 (Na). In windowless systems, elements with as low atomic number as 4 (Be) have been detected, but the problems involved get progressively worse as the atomic number is reduced .

3.2.5 Transmission electron microscope (TEM):

- **Basic Principle:**

Transmission electron microscopy (TEM) is a technique used for analyzing the morphology, defects, crystallographic structure, particle size and even composition of a specimen. In this technique a beam of electrons is transmitted through an ultra thin specimen, interacting with the specimen as it passes through. An image is formed from the interaction of the electrons transmitted through the specimen; the image is magnified and focused onto an imaging device, such as a fluorescent screen, on a layer of photographic film, or to be detected by a sensor such as a CCD camera. The transmission electron microscope (TEM) operates on the same basic principles as the light microscope but uses electrons instead of light. What you can see with a light microscope is limited by the wavelength of light. TEM use electrons as "light source" and their much lower wavelength make it possible to get a resolution a thousand times better than with a light microscope.

TEMs are capable of imaging at a significantly higher resolution than light microscopes, owing to the small De Broglie wavelength of electrons. This enables the instrument's user to examine fine detail even as small as a single column of atoms, which is tens of thousands times smaller than the smallest resolvable object in a light microscope. TEM forms a major analysis method in a range of scientific fields, in both physical and biological sciences. TEMs find application in cancer research, virology, materials science as well as pollution and semiconductor research. At smaller magnifications TEM image contrast is due to absorption of electrons in the material, due to the thickness and composition of the material. At higher magnifications complex wave interactions modulate the intensity of the image, requiring expert analysis of observed images. Alternate modes of use allow for the TEM to observe modulations in chemical identity, crystal orientation, electronic structure and sample induced electron phase shift as well as the regular absorption based imaging.

- **Experimental Set Up:**

TEM offers two methods of specimen observation-

1. Image mode

2. Diffraction mode

In image mode, the condenser lens and aperture will control electron beam to hit the specimen, the transmitted beam will be focused and enlarged by objective and projector lens and form the image in the screen, with recognizable details related to the sample microstructure. In diffraction mode, an electron diffraction pattern is obtained on the fluorescent screen, originating from the sample area illuminated by the electron beam. The diffraction pattern is entirely equivalent to an X−ray diffraction pattern. A single crystal will produce a spot pattern on the screen and polycrystal will produce a powder or ring pattern.

The microstructure, e.g. the grain size, and lattice defects are studied by use of the image mode, while the crystalline structure is studied by the diffraction mode.

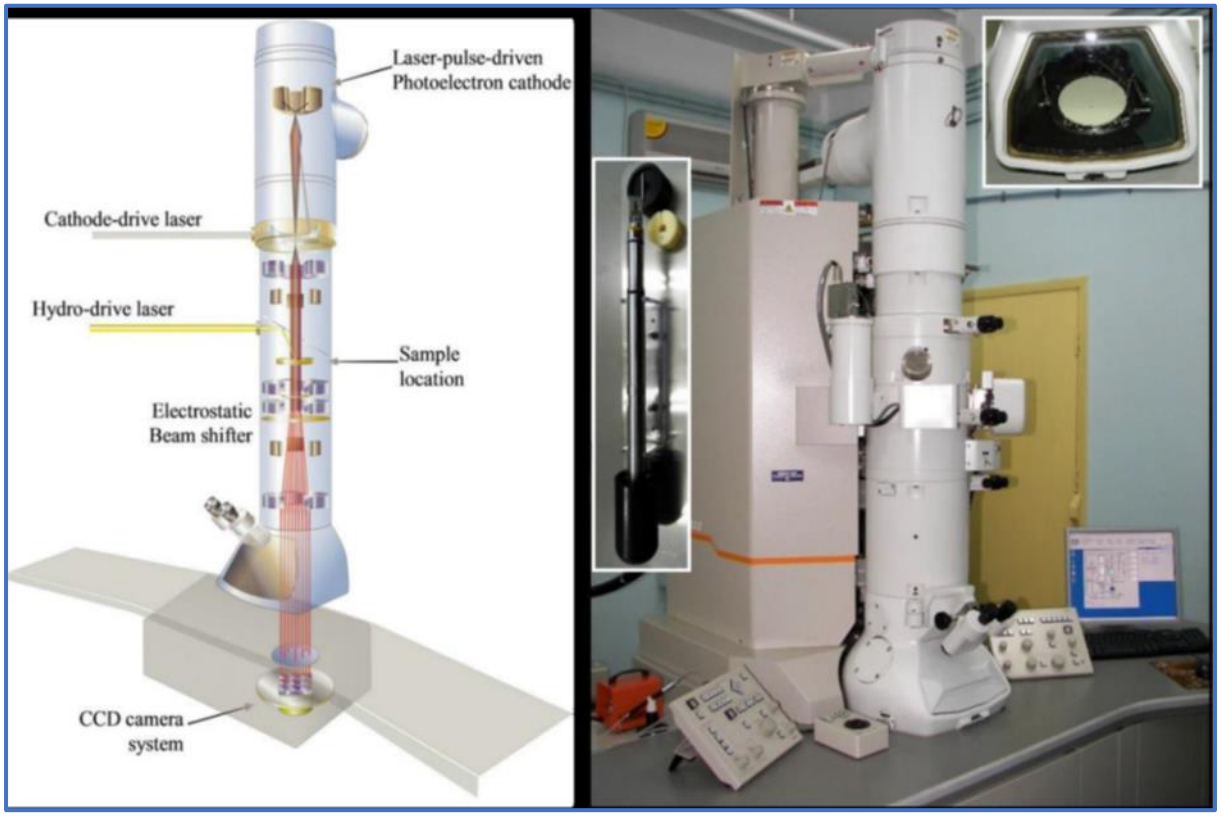

Figure 3.15: Left: Layout of optical components of basic TEM instrument

Right: JEOL JEM-2100 HRTEM

- **Restrictions on samples:**

Sample preparation for TEM generally requires more time and experience than for most other characterization techniques. A TEM specimen must be approximately 1000 A^{o} or less in thickness in the area of interest. The entire specimen must fit into a 3 mm diameter up and be less than about 100 microns in thickness. A thin, disc shaped sample with a hole in the middle,

the edges of the hole being thin enough for TEM viewing, is typical. The initial disk is usually formed by cutting and grinding from bulk or thin film/substrate material, and the final thinning done by ion milling. Other specimen preparation possibilities include direct deposition onto a TEM-thin substrate (Si_3N_4, carbon); direct dispersion of powders on such a substrate; grinding and polishing using special devices like tripod; chemical etching and electro-polishing; and lithographic patterning of walls and pillars for cross-section viewing. A focused ion beam (FIB) may be used to make cross-sections; however this capability is not currently available at HUJ.

- **Applications:**

a. Morphology

The size, shape and arrangement of the particles which make up the specimen as well as their relationship to each other on the scale of atomic diameters.

b. Crystallographic Information

The arrangement of atoms in the specimen and their degree of order, detection of atomic scale defects in areas a few nanometers in diameter.

c. Compositional Information (if so equipped)

The elements and compounds, the sample is composed of and their relative ratios, in areas a few nanometers in diameter.

3.2.6. X-Ray Photoelectron Spectroscopy (XPS):

X-Ray Photoelectron Spectroscopy is one of the most powerful surface analytical techniques capable to provide accurate qualitative elemental analysis (for all elements except hydrogen and helium), quantitative composition and determination of chemical state such as binding and oxidation can also be done. The information should be originated within ~10 nm from the outer surface.

- **Principles of XPS:**

XPS is based on the photoelectric effect which is discovered by Hertz in 1887. In this case, electron emission from the surface is resulted due to the interaction of an x-ray photon of

$$h\nu = E_b + E_{kin} + W_f$$

sufficient energy with the solid surface. The applied x-ray of 1-15 KeV energy is capable to induce electrons not only from the outer shells but also from the core levels of all elements of periodic table. The governing equation of this phenomenon is as follows:

Where, $\mathbf{E_b}$ is binding energy, $\mathbf{E_{kin}}$ is kinetic energy of photoelectron, $\mathbf{W_f}$ is work function of the instrument.

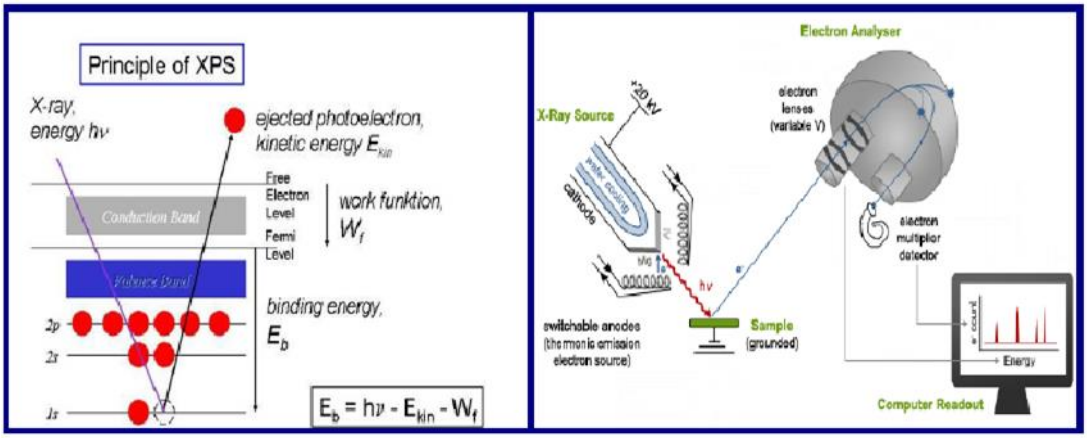

Fig 3.16: Basic principles and constructions of XPS

- **Configuration of XPS instrument:**

The experimental set up contains mainly the following parts: (i) an X-ray source for XPS, (ii) an electron energy analyzer, combined with a detection system and (iii) a sample stage, all contained within a vacuum chamber. As for most techniques, the system is operated and controlled by a computer, usually provided with software allowing mathematical treatment as shown in Fig 3.16.

- **X-ray source:**

Since XPS is concerned with the analysis of core electrons from a solid surface, sources used in XPS must be able to produce photons of a sufficient energy to access a suitable number of core electron levels. Photons of this energy lie within the X-ray region of the electromagnetic spectrum. As a result, these are otherwise referred to as X-rays. X-ray tubes produce X-rays by directing a sufficiently energetic electron beam at some metallic solid. This metallic object is referred to as the X-ray anode, with the electron source being the cathode. Although any solid can in principle be used as an X-ray anode, Al has become that most commonly used in XPS

due to the relatively high energy and intensity of Al-*K*α X-rays, the minimal energy spread of Al-*K*α X-rays and the fact that Al is an effective heat conductor.

- **Electron energy analyzer:**

Since information in XPS is derived from the *Ekin* of the electron emissions, effective analysis requires energy filter that exhibits both a high-energy resolution and a high transmission. The former allows for the separation of closely spaced peaks, thereby optimizing speciation identification capabilities, while the latter allows for sensitivity to be maximized. The two primary energy filter configurations used in XPS named **Cylindrical Mirror Analyzer (CMA), Concentric Hemi spherical Analyzer (CHA).**

- **Detector:**

In XPS, it is not only important to measure the energy of the electron emissions but also the number of electrons produced. XPS spectra is plotted in units of energy versus intensity, with the energy defined by the energy analyzer used and the intensity defined by the number of electrons recorded by the detector. To obtain the best possible sensitivity, the detector must be capable of recording individual electrons, that is, operating in pulse counting mode. This signal is recorded in units of current (A), which are then represented in units of counts per second.

- **Sample stage:**

The mounting of the samples on the sample holder should be done in such a way that electrical conduction is guaranteed. This is achieved by using metallic clips or bolt-down assemblies. Alternatively a metal loaded tape may also be used. In the case of powders, the particles can be pressed into an indium foil or carbon tape.

- **Vacuum requirement:**

As XPS is a surface sensitive method, impurities can play a major role in the observed spectra. The criterion is that a good vacuum is needed to maintain the integrity of the surface. In general, 10^{-5}Torr is sufficient to allow the photoelectron to reach the detector without suffering collisions with other gas molecules. On the other hand, 10^{-9}Torr or lower is required to keep an active surface clean for more than several minutes. So, 10^{-8}-10^{-9}Torr provides a reasonable pressure range for XPS measurement. Sample analysis was performed on the SPECS with hemispherical energy analyzer (HAS 3500). Photoelectrons were excited using the monochromatic Mg Kα X-ray (1253.6 eV) or Al Kα X-ray (1486.6 eV) was used as the

excitation source operated at 10 kV and with an anode current 17 mA. The photograph of the X-ray photoelectron spectroscopy is shown in the **Fig3.17.**

Fig 3.17: Experimental set up of XPS

3.2.7. IV Characterization Apparatus:

IV setup as precision source/Measure Unit (SMU, KEYSIGHT B2902A) is used to measure current-voltage characteristics of any electronics device more accurately. It is also used to determine forward and reverse bias IV characteristics as well as leakage current measurement. SMU combines of a current source, a voltage source, a current meter, a voltage meter along with the capability to switch easily between this various functions into a single instrument.

An SMU is a precision power sourcing instrument that provides voltage sourcing and measurement resolution at or below 1 mV as well as current sourcing and measurement resolution below 1 μA. In addition, SMUs offer remote-sense capability and a four-quadrant output that incorporates both bipolar voltages and the ability to sink power. Finally, SMUs are optimized for sweeping both current and voltage to determine the IV characteristics of a device. As a result, SMUs have been widely adopted, especially in the semiconductor industry and are a common component in many automated test systems.

Virtually all research, design, development, and production applications require an instrument that can source power to a device that is being developed or tested. Many of these applications also require the ability to monitor the voltage and current being consumed by the device to characterize device behaviour or to test for proper operation. Often, you can meet both of these requirements with a single programmable power supply that sources either a constant voltage

or constant current as well as reads back the associated current or voltage. In these applications, milliamp sensitivity in current measurement often suffices.

Other applications require sourcing and measuring with more precision than you can find on a typical programmable power supply. For instance, consider ubiquitous electronic devices for which every μ amp of current drawn reduces battery life. Manufacturers often need to characterize these devices during production for power draw in a variety of states. For these situations, a high-precision power supply offering μamp-level sensitivity works well.

Certain applications are especially demanding and require even higher precision and specific features. Semiconductor validation and characterization is an example of an application that requires current sensitivity into the nanoamp range and below. In addition, the demand for m a traditional programmable power supply insufficient. For these situations, where precision low-level sourcing and measuring is needed, a source measure unit (SMU) is the best choice. ore precision, higher speed, remote sensing of voltage and four-quadrant outputs can render.

This SMU connects to PC via IV measurement software by a LAN connection. This IV measurement software is used to measure a variety of function such as sweep measurement, sampling measurement, graphical display functions. It also have an ability to save test result into CSV file. Figure 3.18 shows the Photograph of SMU (KEYSIGHT B2902A) instrument with display of IV measurement software.

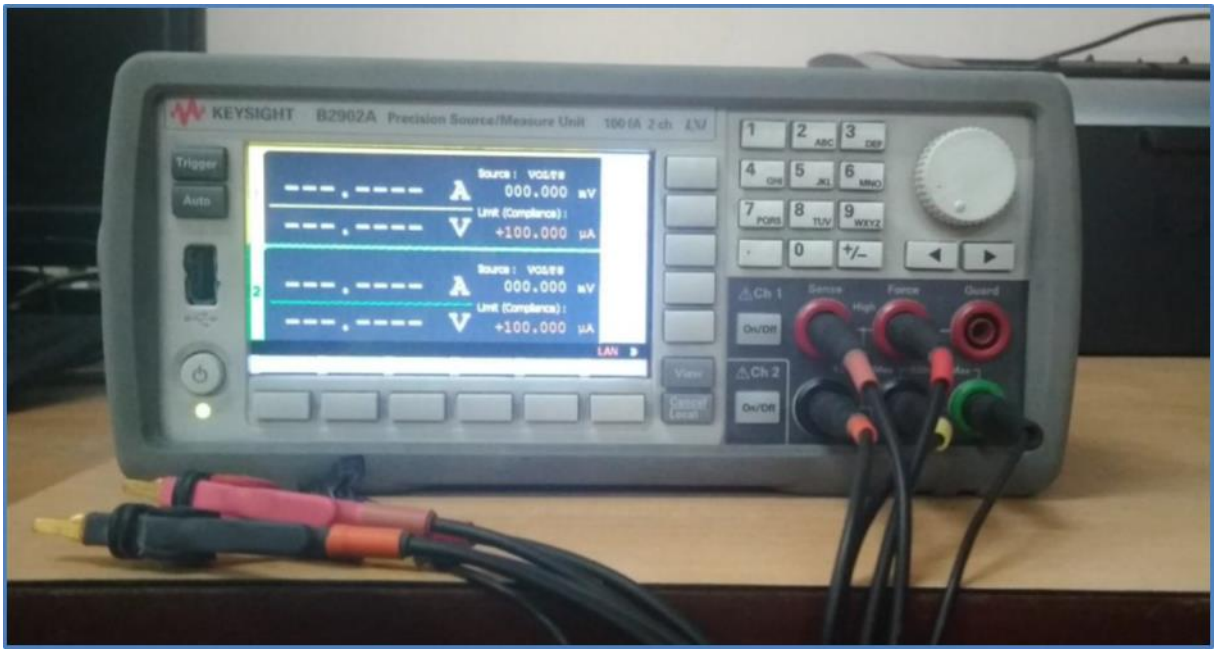

Fig. 3.18: The Keysight B2902A SMU at Thin Film and Nano Science Lab, JU

3.2.8 High Voltage DC power Supply:

In field emission instrument D.C voltage is applied between the cathode (sample under test) And the anode. For this experiment a 5 KV-0.5 A DC regulated power supply unit (model NTPL/91/03-04), which is manufactured by Neo Tele-Tronix Pvt.ltd, calcautta is used. The input to the unit is 230V, 50 Hz, 1 Ph, AC supply and output is continuously vary from 0 to 5KV.

3.2.9. Electrometer, Multimeter:

Keithley electrometer (Model 671 and 6517A) is used to measure current voltage characteristics of the samples. The range of the voltage and current are ± 1000v and ± 1pA to ± 20mA respectively. Another Keithley electrometer (Model 6514) is used to measure field emission current range ±100nA to ±21 mA. Also several multimeter (RISH MULTI 15 S) are used during the experiment.

3.3. Application oriented equipment

3.3.1. Apparatus for field Emission property measurement:

Field emission is a process where electrons can be pulled out of the surface with certain material. With the application of macroscopic electric field the surface potential barrier is educed in height but decreased in width. This would enable the electrons to tunnel from the barrier to reach the vacuum and the electrons can be collected by the anode. Field emission measurements are used a diode electrode configuration consisting of a cathode (the film under test) and a stainless steel tip anode (conical shape with a 1 mm tip diameter) is mounted in a liquid nitrogen trapped rotary diffusion vacuum chamber with appropriate chamber baking arrangement. The measurements are performed a base pressure of ~7 x 10^{-7} mbar. As the substrate was conducting, the positive terminal of the high voltage dc power supply was connected with the films by silver paint (Acheson Colloid Co. UK), at least 6 mm away from the position of the anode tip. The ohmic nature of the contact is checked before field emission experiment. The tip-sample distance is continuously adjustable to a few hundred μm by spherometric arrangement with screw-pitch of 10 μm. The position of just touching the anode with the sample is measured by an optical microscope and then various spacings are obtained by rotating the micrometer screw as its screw pitch is known. Field emission current voltage measurements are done by the help of a multimeter. The whole surface of the film is visible from the chamber view port, which is enabled to recognize the electron emission and discharge.

The schematic of the field emission apparatus is shown in **Fig 3.19**. The field emission current voltage relationship is satisfactorily explained by using the well-known general F-Nequation.

$$J = \frac{a\beta^2 E^2}{\phi} \exp\left(\frac{-b\phi^{3/2}}{\beta E}\right)$$

Where a & b are Fowler Nordheim constants, "ϕ" is work function, β is Field enhancement factor, E is the Applied electric field and J is Current density.

F-N plot is drawn in between ***ln(J/E²)*** vs. ***1/E***. Field enhancement factor (β) can be calculated from the following equation where S is slope of F-N plot.

$$\beta = \frac{-b\phi^{3/2}}{S}$$

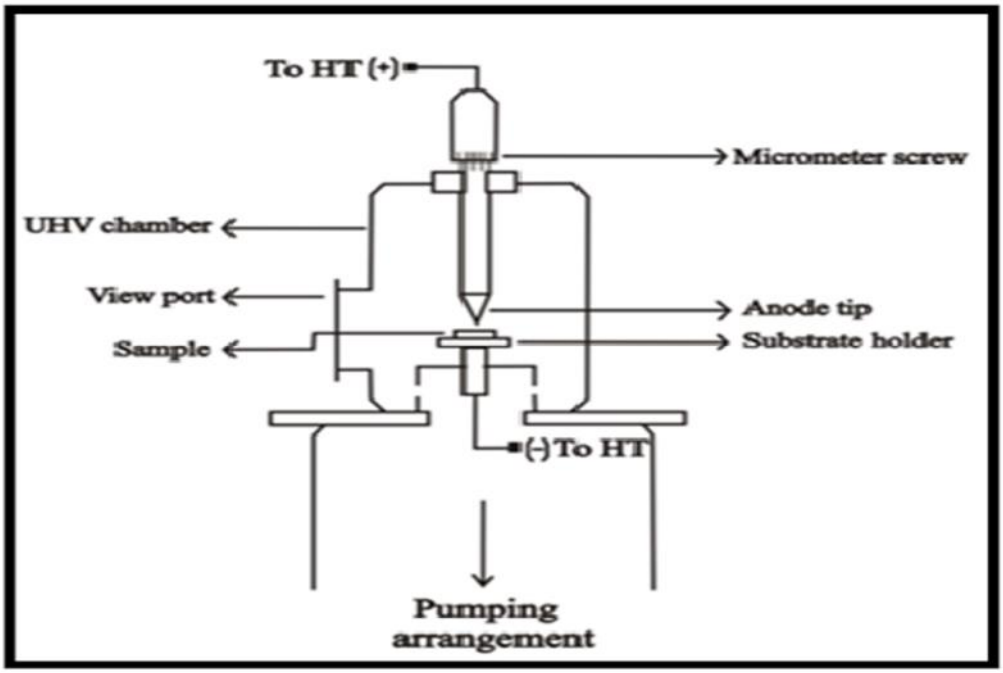

Fig 3.19: Schematic of Field Emission Apparatus

3.3.2. Apparatus for Photocatalysis measurement:

The photocatalytic measurement of CuBO2 nanoparticals for different sizes was studied by a photoreactor. It is also used for novel photoreactor. As in the case of water treatment to obtain the greatest reaction yield, whilst expend the least amount of energy. So photocatalytic reactor parameters for achieving these goal such as,

a) Photoreactor

b) Type of illumination

c) Catalyst type

d) Position irradiation source

- **Light Source**

CuBO2 nanoparticals absorb the radiation below the visible range of light spectrum. So photoactivation of CuBO2 nanoparticals require radiation with light of wavelength belonges to UV region. The type of irradiation is a major design issue for photocatalytic reactors. The reactor chamber was equippred with UV-C (200-280 nm) lamps (PHILIPS, emission maximum cantered at 254.6 nm). These UV tube provide light inside the photoreactor.

- **Photoreactor**

The photoreactor was designed with internal high pressure mercury lamp of 400 W (Philips) including a UV cut off glass filter transmitting λ>400nm and it was surrounded by a water cooling quartz jacket.

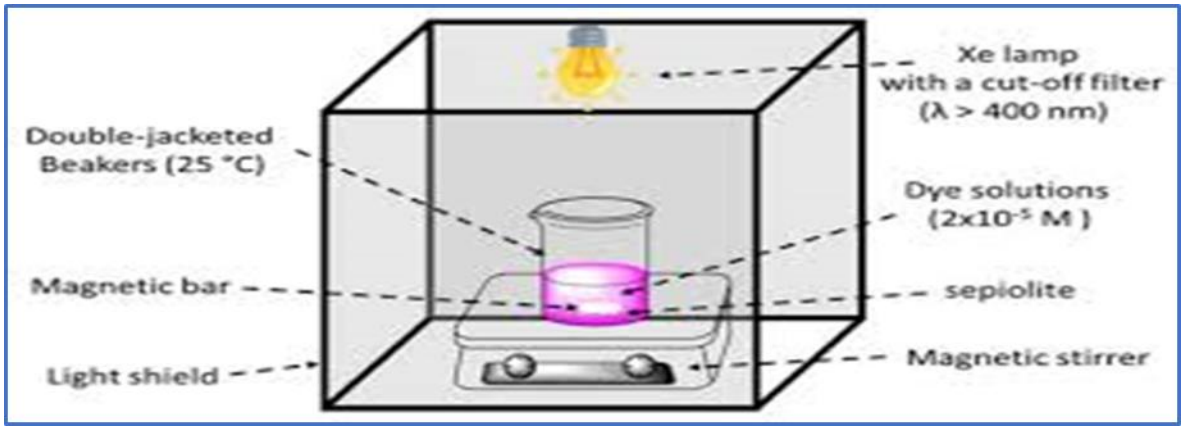

Fig 3.20: Photoreactor

All photocatalysis process was carried out in a simple rectangular photoreactor. The upper portion of the reactor is fixed with siding door, which are used for collecting the reaction solutions. All four sides are made of black colored wood which used to protect the UV

irradiation outside the reactor. The sample was dispersed with in a dye solution in a 50 mL quartz beaker. Inside this photoreactor, the distance between quartz beaker and the UV lamp is maintain approximately 15 cm. Then the solution was stirred magnetically for increasing the mass transfer and to provide a homogeneous system between the headspace and the liquid.

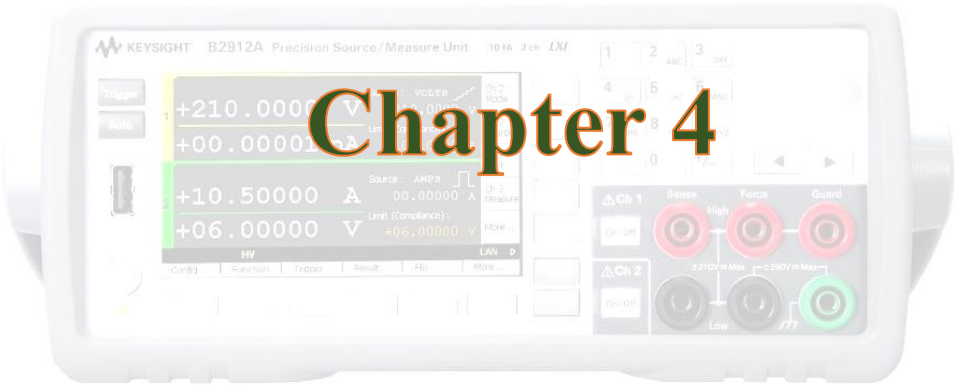

Chapter 4

MODULATION OF TRANSPORT PROPERTIES OF $CuBO_2$ BY SULFUR DOPING

Abstract

$CuBO_2$ is a novel material in the research field of transparent conducting oxide. Mixing of different orbitals to achieve proper control on transport properties via shallow acceptor levels is extremely important in order to have an actual p-type transparent oxide involving delafossite. However, there are few attempts towards these. This study demonstrates an effective way out to achieve significant delocalization of holes in the (Cu 3d + O 2p) valence band with a direct gap by different chalcogen (Ch = S, Se) doping. A modulated valence band in $CuBO_2$ was achieved via sulfur incorporation at the O site. From the exhibition of better transport properties were reflected in the doped material. Dispersion of Cu 3d character by incorporating shallower acceptor (Ch 3p) states is concluded upon analysing the photoemission spectra of the valence band. In this study we have synthesized $CuBO_2$ and sulfur doped $CuBO_2$ nanostructures via easy molten-salt method. Structural characterization was performed using X-ray diffraction (XRD) which confirmed good crystalline structure and proper phase formation. Field emission scanning electron microscopy (FESEM) revealed morphological information of the samples. The transport properties of the samples were studied using a "SMU" in room temperature. Here we discussed further how the conductivity of sulfur-doped $CuBO_2$ is increased up to a certain percentage of sulfur doping in $CuBO_2$, after that it will be decreasing.

4.1 Introduction

The rapid development of transparent conducting oxides (TCOs) reveals the huge market needs. Relative to the n-type TCOs such as ZnO, In_2O_3, SnO_2, the conductivity of p-type TCOs is much lower. The search for p-type transparent conducting oxides (TCOs) has done more to improve their conductivity. In many TCOs, $CuBO_2$ is well-known as an important TCO with various applications, e.g. electronic devices, [1−2] gas sensors,[3] energy generation devices,[4] thermoelectric materials, [5−6] photocatalysts.[7] However, its low p-type conductivity limits its efficiency. Doping is one of the promising means to solve this problem by introducing either a less electronegative element than O [8−10] or the hole carriers,[11−12] which has been confirmed to increase p-type conductivity of $CuBO_2$. The reduced band gap and effective mass of S-doped $CuBO_2$ have been reported,[9] indicating that the conductivity was enhanced. Here, considering $CuBO_2$, a prototype group IIIA delafossite as an example, we demonstrate geometrical and band structure engineering both theoretically and experimentally to remove its inherent indirectness of the band gap with additional potential Functionality.

Mazumder et al. [10] further investigated the effect of chalcogen incorporation at O site, showing that the dispersed valence band top and the increased covalency were good for p-type conductivity. Recently, they found that the doping-induced polytype $CuBO_2$ has shown a direct band gap and the better transport character. On the other hand, the introduced holes [12] and the enhanced covalent character of Cu-O bonding [11] were all beneficial to p-type conductivity. The delafossite family of oxides, first discovered back in 1873, [13] usually crystallizes with rhombohedral and hexagonal symmetry [14-15]. Since the path breaking work of Hosono and his co-workers,[16] $CuMO_2$ delafossites, where M represents metals, rare earths, and lanthanides, [17-18] have been identified as the potential p-TCOs, heralding a new hope in transparent electronics [19-20]. Band structures of mostly cuprous delafossites have been investigated rigorously, but direct gap IIIA delafossite has not been reported in the literature to date. The equilibrium band structure of, say, $CuAlO_2$ is featured with an intrinsic indirect gap. The flat band from Γ to Z is due to π antibonding between Cu and O, and dispersion around F is due to hybridization between Cu $3d_z^2$–s and between d_z^2–s and O p_z states. Doping of a less electronegative element than oxygen at the O site can serve two-fold, (I) to reduce the overall "hole capacity" of the valence band (VB) edge by reducing the effective electronegativity and (II) to modify the band structure consisting of an increased shallower antibonding density of states (DOS) with lower effective mass for major charge carriers. For this to arrange, one of the dopant's dominant orbitals must participate in the "reconstruction" of the VB by hybridizing with Cu $3d_z^2$ or O $2p_z$ or with both of these. Copper aluminate, the prototype p-type delafossite, was chosen as host to verify the proposition. As Ch $3p_z$ is found to be situated near Cu $3d_z^2$ and O $2p_z$ states with effective p–p and p–d coupling, we have considered them as a proper dopant choice. Therefore, the aim of this Letter becomes to examine a proposition regarding generation of a shallower acceptor level in the vicinity of antibonding Cu 3d states as to facilitate higher conductivity as well as to disturb strong σ-symmetry between Cu $3d_z^2$ and O $2p_z$ states in group IIIA delafossites. The concept of TCO was primarily reported by Kawazoe *et al* [21] in 1997. In their work, fabrication of $CuAlO_2$ thin film with p-type conductivity and transparency of $CuAlO_2$ thin films was performed and a new idea, commonly known as 'chemical modulation of the valence band,' was proposed. This path-breaking study opened up the field of transparent electronics. Later on a group of Cu [I]-based delafossite TCOs was invented, such as $CuInO_2$, $CuCrO_2$, $CuGaO_2$, $CuYO_2$, etc. and very recently $CuBO_2$ [22-23], which has already showed multifunctional activities [24-25]. In this present paper, a novel nanonetwork-like structure of $CuBO_2$ has been reported for the first

time. Detailed morphological analysis and optical studies are carried out for the as-synthesized samples. Our present work to study the conductivity of $CuBO_2$ nanonetwork-like system.

4.2 Experimental details

4.2.1 Synthesis

All the precursors were used to synthesize $CuBO_2$ nanorods which were analytically pure and used without further purification. Commercially available copper acetate [$(CH_3COO)_2Cu.\ H_2O$ (99.99%)], Borax [$Na_2B_4O_7.10H_2O$ (99.99%)], Sodium chloride (NaCl) and Potassium chloride (KCl) were used as starting materials. For the optimization of the synthesis of proper phase $CuBO_2$, we have to take those precursors in a stoichiometric ratio of 1:0.25:40:40.

These materials were than taken in a mortar pester and grinded manually for 30 minutes to mixed them properly. The ground powder mixtures were taken into alumina boat and annealed in furnace at 800^0c for 180 minutes. The sample were cooled naturally at room temperature. The obtained deep brown product was thereafter washed in deionized water and filter several times to removed the residual salts. The residue was dried in an oven at 60^0c for 24 hours. Additionally, the probable chemical reaction involved behind the production of $CuBO_2$ may be written as the following:

$$Na_2B_4O_7 \cdot 10H_2O \rightarrow NaBO_2 + B_2O_3 + 10H_2O$$

$$Cu{-}ac \cdot H_2O \rightarrow Cu{-}ac + H_2O$$

$$NaBO_2 + B_2O_3 + Cu{-}ac \rightarrow Na{-}ac + CuBO_2$$

All the precursors were used to synthesize "sulfur Doped $CuBO_2$" nanorods which were analytically pure and used without further purification. Here potassium sulphide (K_2S) used as a sulfur source. Commercially available copper acetate [$(CH_3COO)_2Cu.\ H_2O$ (99.99%)], Borax [$Na_2B_4O_7.10H_2O$ (99.99%)], Sodium chloride (NaCl), Potassium chloride (KCl) and K_2S were used as starting materials. For the optimization of the synthesis of proper phase

$CuBO_2$, we had to considered the synthesis process at 800^0C for 180 minutes. In this work we were doped different percentages of sulfur in $CuBO_2$. For example, those precursors were mixed with various stoichiometric ratio which are respectively 1:0.25:40:40:02, 1:0.25:40:40:.04, 1:0.25:40:40:.06, 1:0.25:40:40:0.10. The samples synthesized from different stoichiometric ratio were labelled as sample A, B, C, D respectively.

These materials were than taken in a mortar pester and grinded manually for 30 minutes to mixed them properly. The ground powder mixtures were taken into alumina boat and annealed in furnace at 800^0c for 180 minutes. The sample were cooled naturally at room temperature. The obtained deep brown product was thereafter washed in deionized water and filter several times to removed the residual salts. The residue was dried in an oven at 60^0c for 24 hours.

Fig 4.1: Digital picture of mortar pester and sample after annealing

4.2.2 Characterization

The synthesized samples were characterized by studying for proper phase formation with the X-ray diffraction (XRD; Bruker, D-8 Advance) with the Cu Kα radiation of wavelength λ = **1.5406 Å**. The morphological nature of the synthesized samples was studied by field emission scanning electron microscope(FESEM,Hitachi,S-4800). The elemental composition was analyzed by X-ray photoelectron spectroscopy using monochromatic Al Kα (hν = **1486.6 eV**) X-ray source and a hemispherical analyzer (SPECS, HSA 3500).

4.3 Results and discussion

4.3.1 Structural studies

The XRD patterns of pure $CuBO_2$ and sulfur doped $CuBO_2$ are shown in the figure 4.2. The distinct and intense diffraction peaks are indicating good crystalline and proper phase formation of $CuBO_2$ and sulfur doped $CuBO_2$ delafossite (JCPDS 28-1256). In figure 4.1 2%, 4%, 6%, and 10% sulfur doped $CuBO_2$ are indicating sample A, B, C, and D respectively. The peaks near 32^0, 35^0, 36^0,38^0,42^0,48^0,53^0,58^0, and 61^0 have come due to reflection from (006), (100), (011), (012), (014), (106), (107), (018), (0011) planes respectively of $CuBO_2$ lattice.

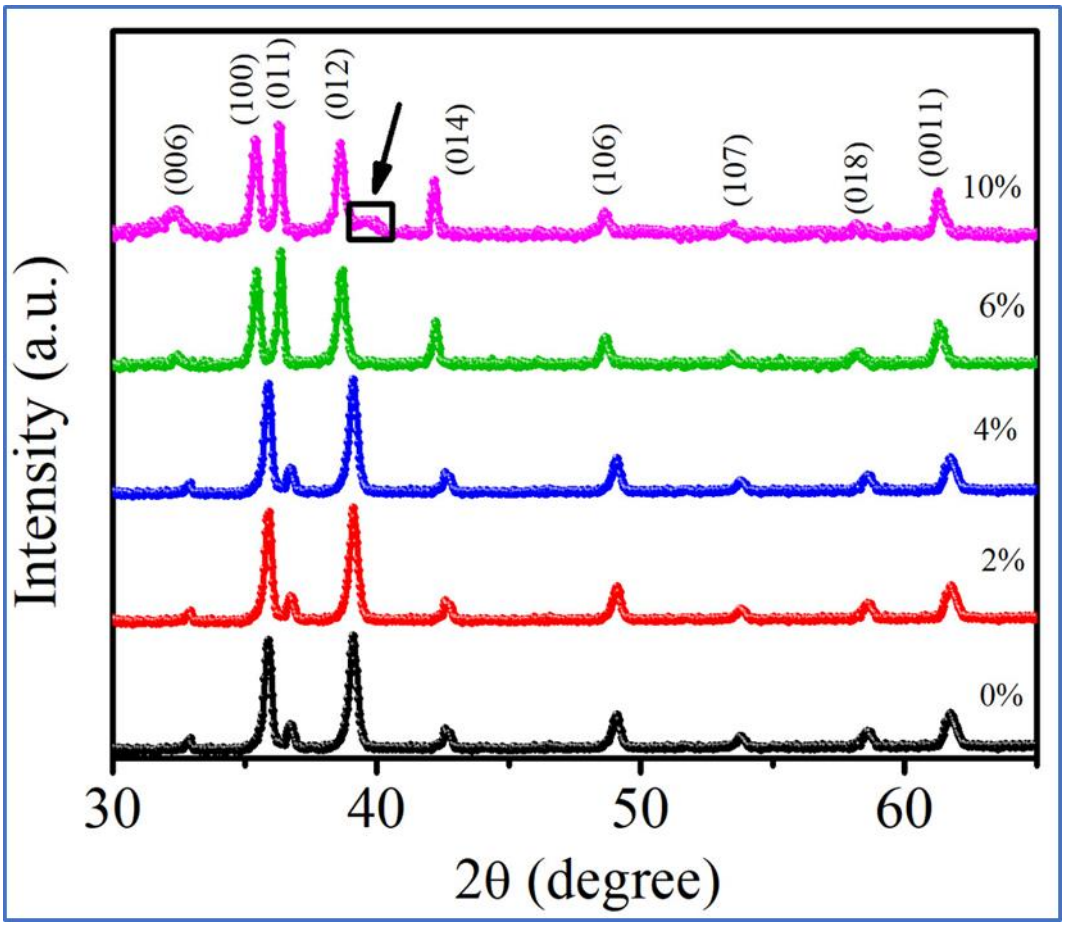

Fig 4.2: XRD patterns of $CuBO_2$ and different percentage sulfur doped $CuBO_2$

The crystallites sizes were calculated from the XRD data using following well known Scherrer's equation-

$$L = 0.9\lambda/2\omega \text{Cos}\,\theta$$

Here 2ω is the full-width half-maxima (FWHM) of the XRD peak and L denotes the average dimension of the grains. From the above "Scherrer Equation" we have calculated the grain size of $CuBO_2$, sample A, B, C, D are 35.16nm, 44.09nm, 28.62nm, 33.10nm and 59.90nm respectively. Figure 4.3 represents the variation of particle size of different samples.

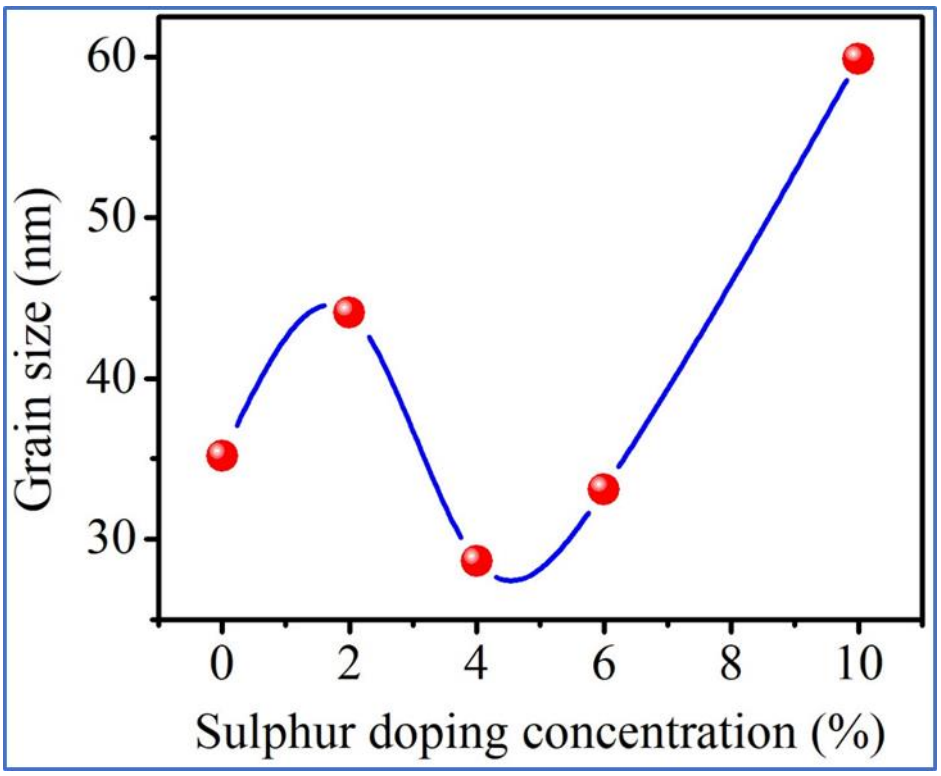

Figure 4.3: Particle size plot for different percentage of sulfur doped $CuBO_2$

The strain Ɛ is calculated from the below equation,

$$\beta = Ɛ \tan \theta$$

Where β is full width half maxima (FWHM), θ is the diffraction angle. The strain is calculated for $CuBO_2$, sample A, B, C, D are 0.000316, 0.000252, 0.000397, 0.000336, 0.000271 respectively. Figure 4.4 represents the variation of strain of different samples.

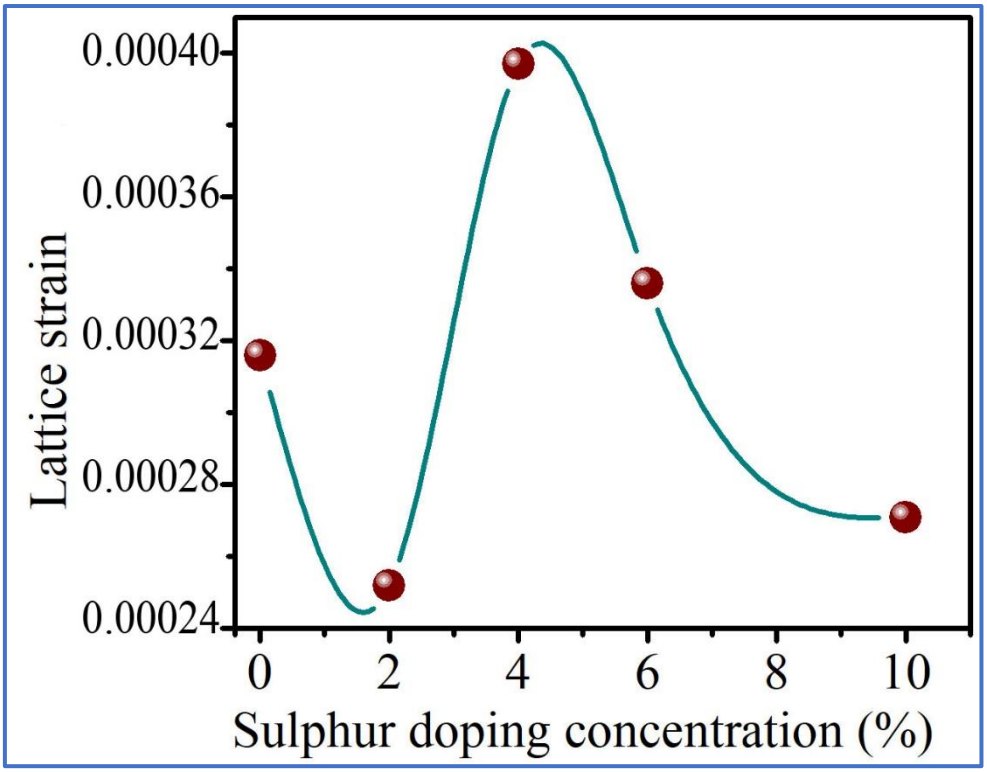

Figure 4.4: Strain plot for different percentage of sulphur doped $CuBO_2$

4.3.2 Compositional studies

The EDX analysis of samples expressed that all the constituent elements, i.e., copper, boron, and oxygen, were present with in the samples. Here EDX spectra of sample A and sample D was shown in figure 4.5 and 4.6 respectively. The atomic percentage of sulfur in sample D was more than sample A. so we can say that sulfur was successfully incorporated in all the samples.

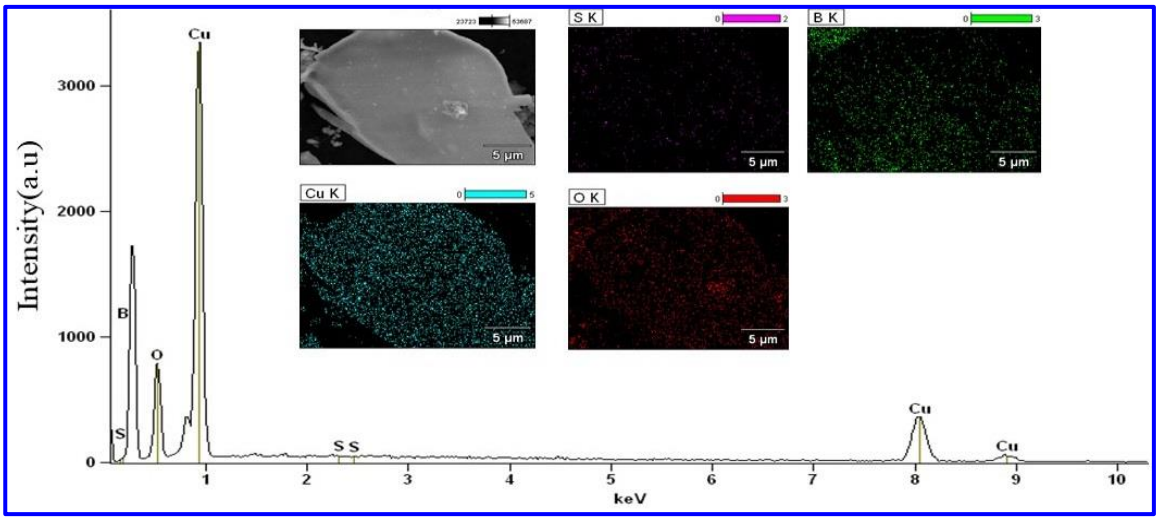

Figure 4.5: EDX spectra for sample A (2% sulphur doped $CuBO_2$)

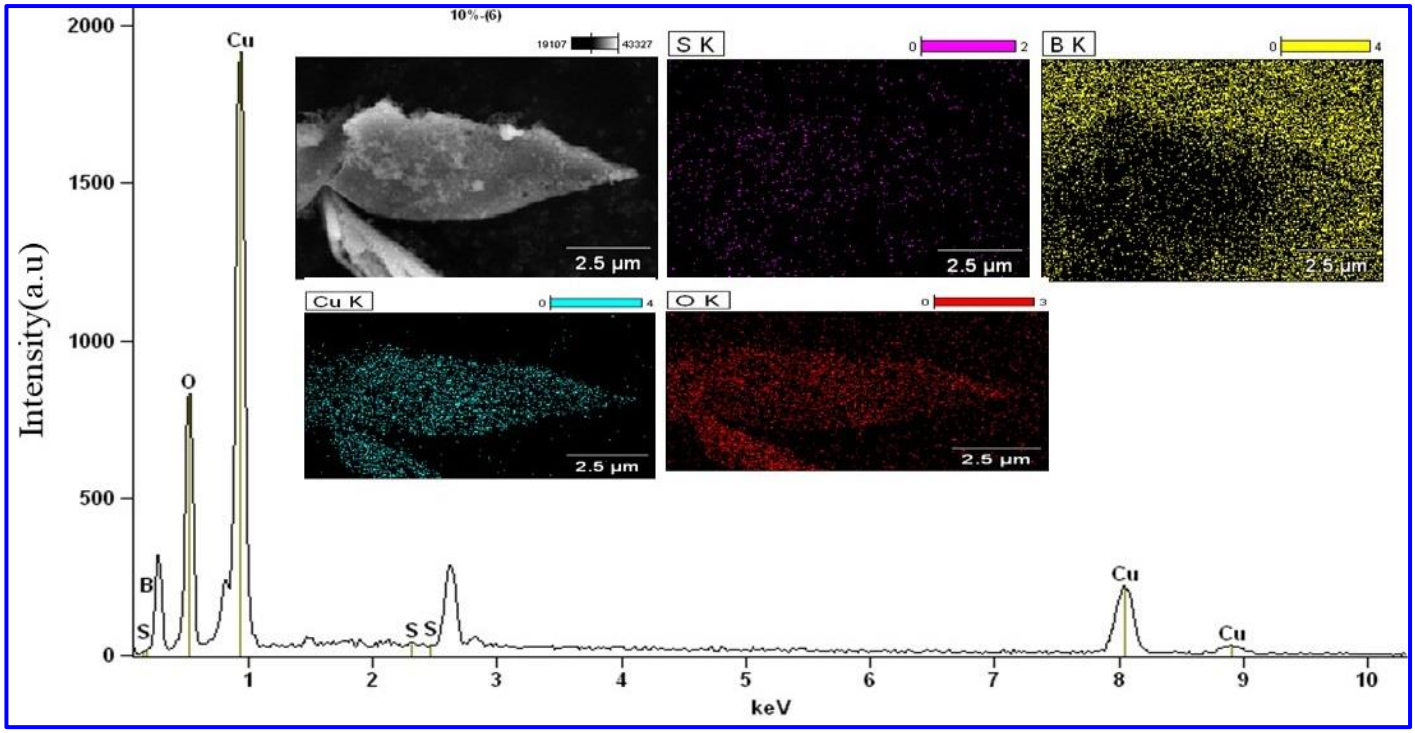

Figure 4.6: EDX spectra for sample D (10% sulphur doped $CuBO_2$)

4.3.3 Morphological studies

The micrographic images of all the samples are shown in figure 4.7 for pure $CuBO_2$, figure 4.8 for sample A, figure 4.9 for sample B, figure 4.10 for sample C, and figure 4.11 for sample D. The FESEM images of all the samples are same i.e. bundled rod like structure. The rods in all the samples have few numbers of irregular attachments.

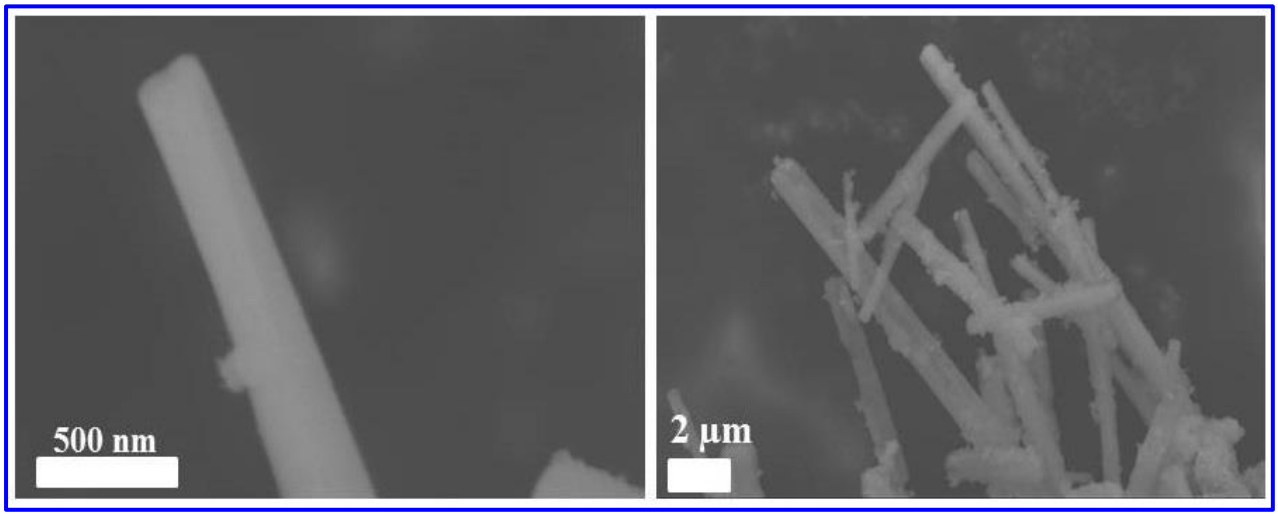

Figure 4.7: FESEM image of pure $CuBO_2$

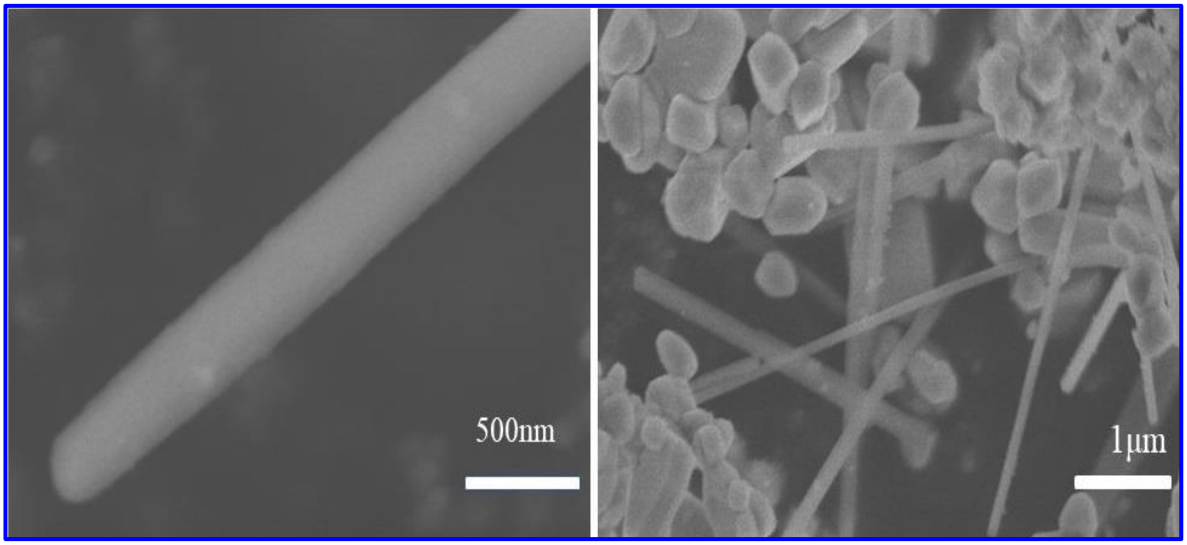

Figure 4.8: FESEM image of sample A

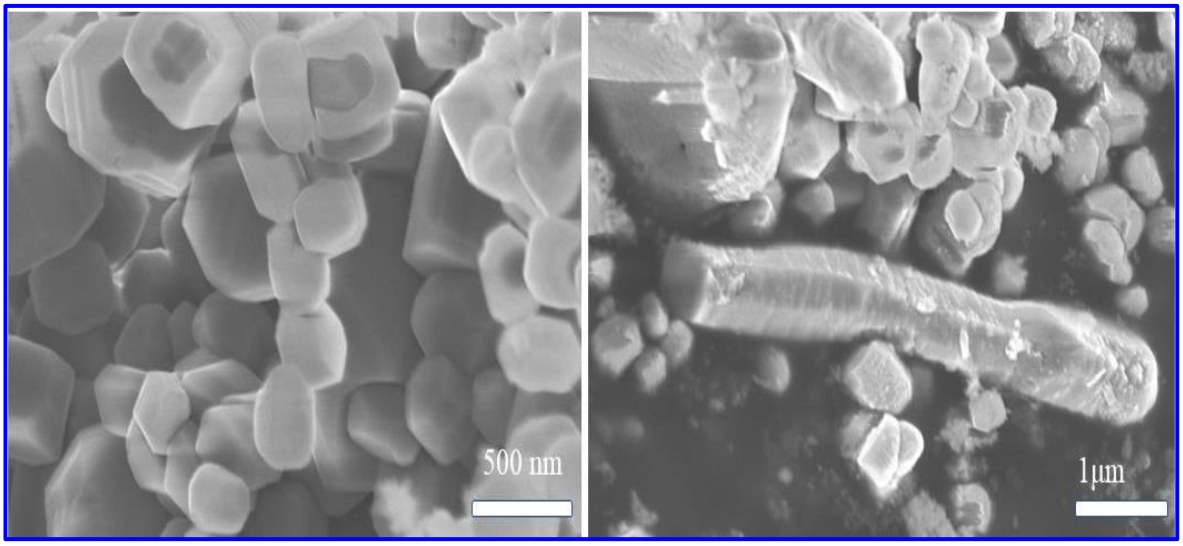

Figure 4.9: FESEM image of sample B

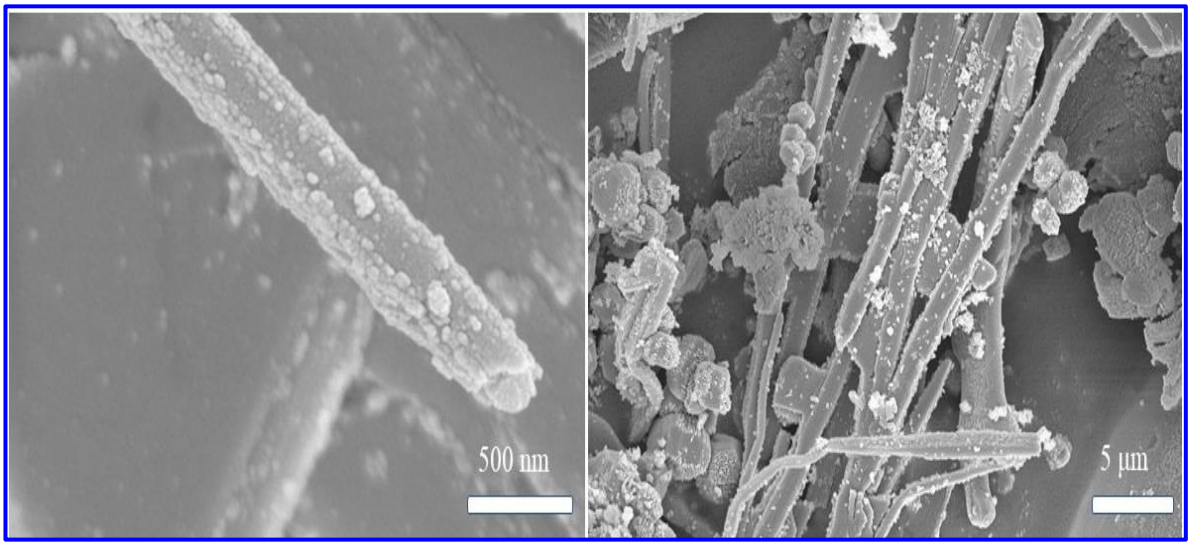

Figure 4.10: FESEM image of sample C

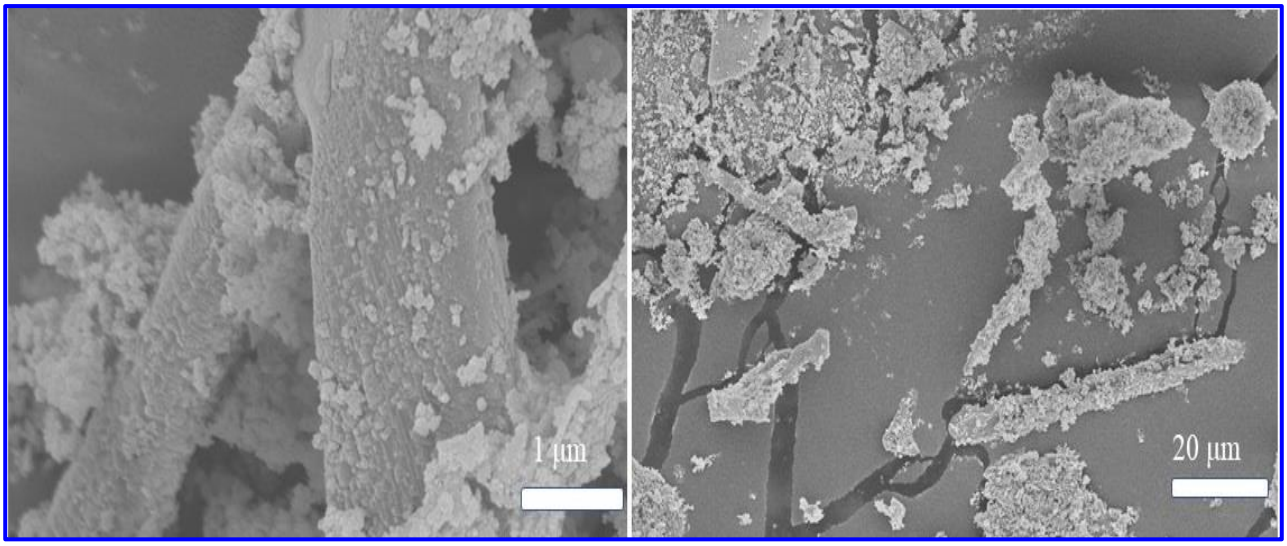

Figure 4.11: FESEM image of sample D

Transmission electron micrographic studies were carried out for sample B to know the exact dimension and crystallographic information of the nano rods, which is shown in figure 4.12.

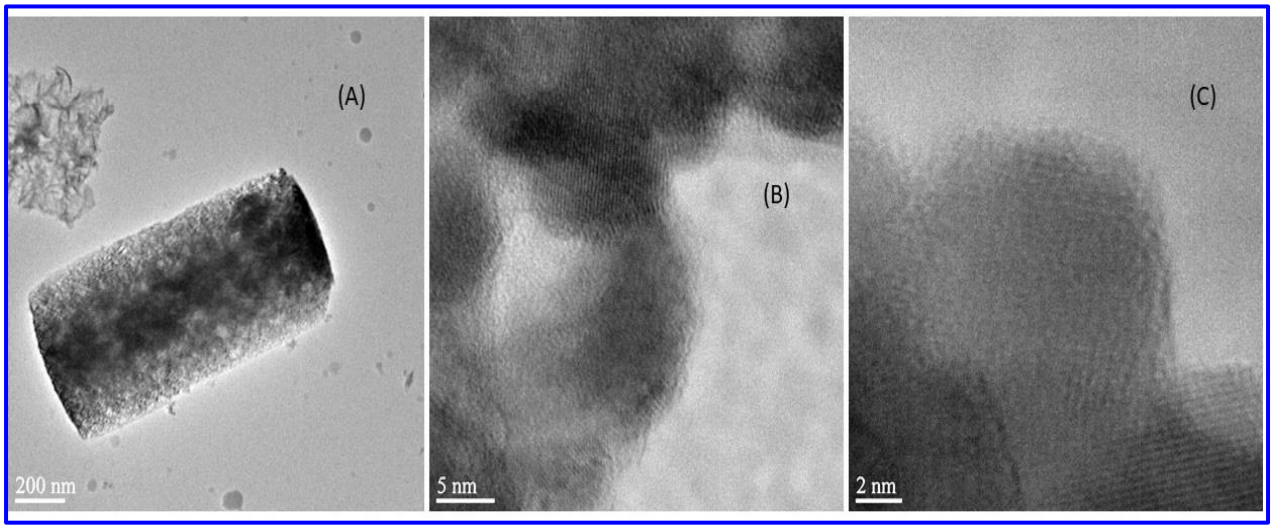

Figure 4.12: TEM image of (A) single nano rod and (B-C) lattice image of one nano rod.

4.3.4 Optical studies

The synthesized sample of different percentages of sulfur doping were spin coated on FTO substrates and their transmission spectra were recorded in the wavelength range 200 nm to 800 nm via UV spectroscopy. All the sample were showed average transparency in (~10%) in the visible range. The transmission spectra of sample A were shown in figure 4.13.

The optical band gap of sample A was calculated using the fundamental absorption which corresponds to electron excitation from valance band to conduction band. Their relation can be presented from the formula as given below

$$(\alpha h\vartheta)^{1/n} = A(h\vartheta - E_g)$$

Where,

E_g = Band gap of the sample.

A=constant

n=Type of transition (n= $^1/_2$for direct band gap,n=2 for indirect band gap) Here we plotted $(\alpha h\nu)^{1/n}$ vs hν taking the direct band gap by taking n=$^1/_2$.Extrapolating the linear portion of the graph to hν axis, the direct band gap was obtained from the intercept which was found to be around **3.41 eV** for sample A.

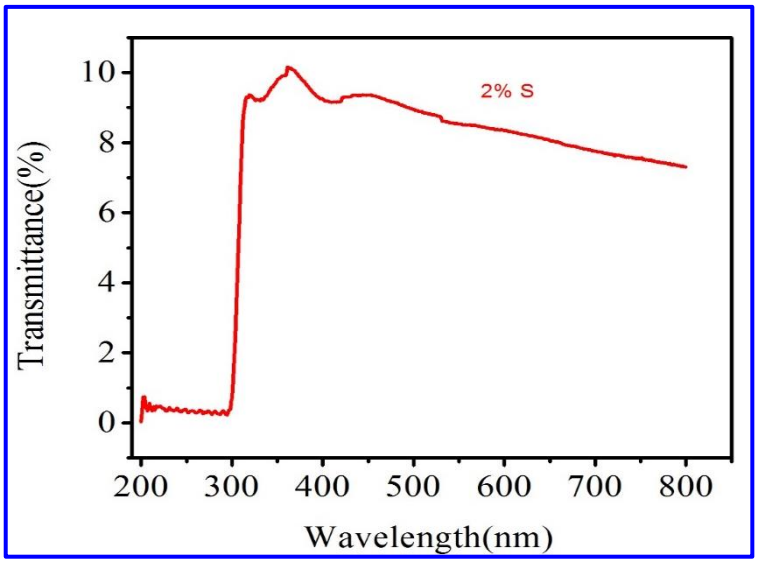

Figure 4.13: Transmission spectra of sample A

4.3.5 IV characteristics

All the samples were characterized using a "SMU" meter to investigate their transport properties. A remarkable enhancement of electrical conductivity was obtained for the samples as depicted in figure 4.14. The actual values of resistivity vs sulphur doping concentration is plotted in figure 4.15. The resistivity was found to decrease with sulphur doping. These results were accounted for the replacement of oxygen by sulphur. The replacement in anionic sites with an atom of higher ionic radii cause larger hopping space for the carriers and thus causes a higher conductivity.

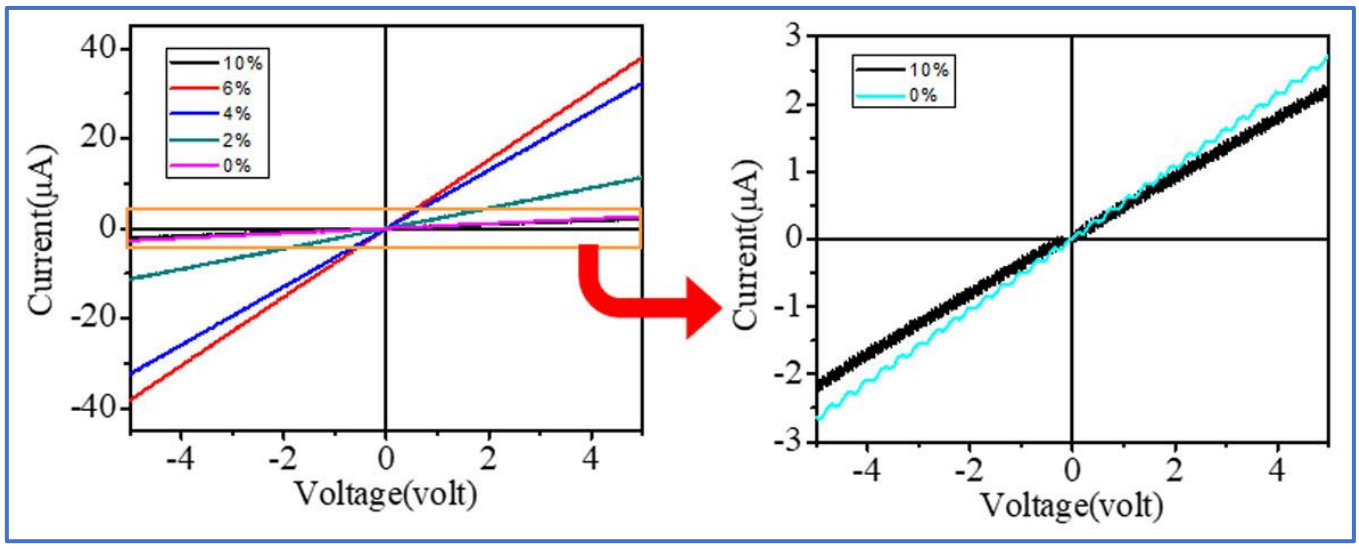

Figure 4.14: IV characteristics of different concentration sulphur doped $CuBO_2$

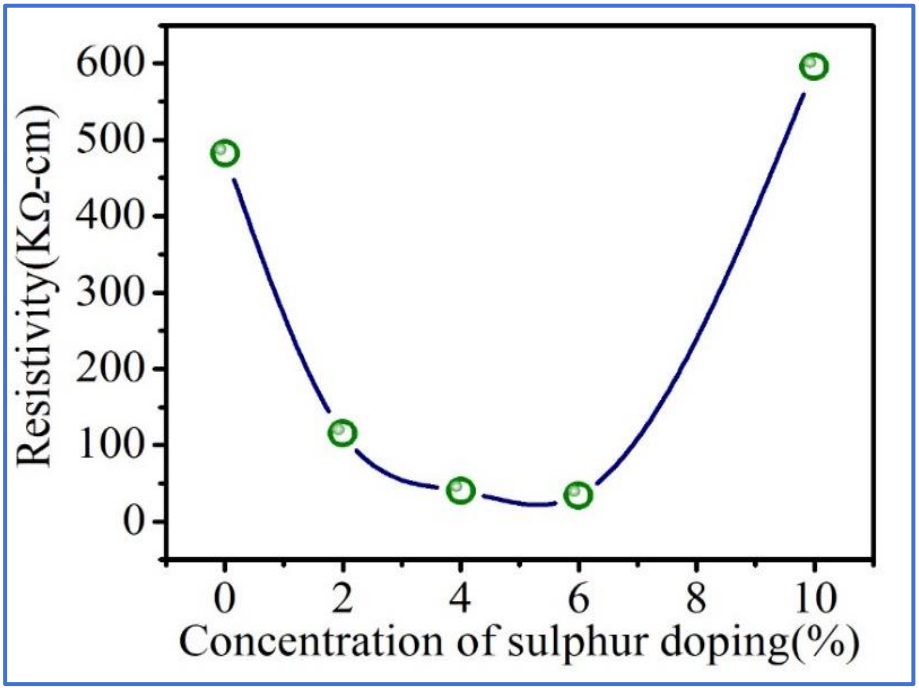

Figure 4.15: Resistivity vs concentration of sulphur doping

However, on further increment of doping concentration of sulphur, the conductivity was found to decrease rapidly. There may be several reasons for this. Firstly, incorporation of foreign atom in too high concentration may cause lattice imperfection. Occurrence of unidentified shoulder peak in XRD spectra may be correlated with such distortions. Secondly, such presence of impurity peak may cause other lattice defects which could not be directly visible under x-ray or EDX studies and can lead to decreased conductivity.

4.4. Conclusion

Sulphur doped $CuBO_2$ delafossites were synthesized using molten salt method. XRD studies revealed the proper phase formation. A slight deformation of the phase was obtained for high amount of sulphur doping. Morphological studies with FESEM and TEM confirmed nanostructural dimension of the samples with rod-like shapes of 22.77 nm diameter. The transport properties of the samples were investigated using standard method which showed a remarkable enhancement of conductivity by 4%. However, an optimized value of sulphur doping concentration (6%) was observed for the samples beyond which, the conductivity of the system became inferior again. This phenomenon was accounted for the increased lattice distortion and phase impurity caused due to heavy sulphur doping. This work opens up a new opportunity to enhance conductivity of novel copper delafossites via replacing the host anions by higher atomic radii chalcogenide atoms.

Reference

[1] D.O. Scanlon, K.G. Godinho, B.J. Morgan, and G.W.Watson, Article name, J. Chem. Phys. 132 (2010) 024707.

[2] J. Luo, Y.J. Lin, H.C. Hung, C.J. Liu, and Y.W. Yang, J. Appl. Phys. 114 (2013) 033712.

[3] C. Baratto, R. Kumar, G. Faglia, et al., Sensors Actuat. B: Chem. 209 (2015) 287.

[4] P.H. Hsieh, Y.M. Lu, W.S. Hwang, et al., Mater. Chem. Phys. 144 (2014) 547.

[5] C. Ruttanapun, W. Kosalwat, C. Rudradawong, et al., Energy Procedia 56 (2014) 65.

[6] T. Suriwong, T. Thongtem, and S. Thongtem, Curr. Appl. Phys. 14 (2014) 1257.

[7] D.H. Xiong, X.W. Zeng, W.J. Zhang, et al., Inorg. Chem. 53 (2014) 4106.

[8] N. Mazumder, D. Sen, U.K. Ghorai, et al., J. Phys. Chem. Lett. 4 (2013) 3539.

[9] H.G. Gao, J. Zhou, and M.H. Lu, Sci. China Phys. Mech. Astron. 53 (2010) 1261.

[10] N. Mazumder, D. Sen, and K.K. Chattopadhyay, AIP Conf. Proc. 1512 (2013) 1060.

[11] H.F. Jiang, X.C.Wang, X.P. Zang, et al., J. Alloys Comp. 553 (2013) 245.

[12] Y. Xu, Z.M. Ao, and D.W. Yuan, Phys. Lett. A 376 (2012) 2613.

[13] Rogers, A. Delafossite from Kimberley. Am. Mineral. 1922, 7, 102−104.

[14] Prewitt, C. T.; Shannon, R. D.; Rogers, D. B. Chemistry of Noble Metal Oxides. II. Crystal Structures of PtCoO2, PdCoO2, CuFeO2 and AgFeO2. Inorg. Chem. 1971, 10, 719−723.

[15] Köhler, B. U.; Jansen, M. Synthesis and Crystal Structure of 2HCuAlO2. Z. Kristallogr. 1983, 165, 313−314.

[16] Kawazoe, H.; Yasakuwa, H.; Hyodo, H.; Kurita, M.; Yanagi, H.; Hosono, H. p-Type Electrical Conduction in Transparent Thin Films of CuAlO2. Nature 1997, 389, 939−942.

[17] Shannon, R.; Rogers, D.; Prewitt, C. Chemistry of Noble Metal Oxides. I. Syntheses and Properties of ABO2 Delafossite Compounds. Inorg. Chem. 1971, 10, 713−718.

[18] Duan, N.; Jayaraj, M. K.; Tate, J.; Sleight, A. W. Transparent p-Type Conducting CuScO2+x Films. Appl. Phys. Lett. 2000, 77, 1325−1326.

[19] Thomas, G. Invisible Circuits. Nature 1997, 389, 907−908.

[20] Banerjee, A. N.; Chattopadhyay, K. K. Recent Developments in the Emerging Field of Crystalline p-Type Transparent Conducting Oxide Thin Films. Prog. Cryst. Growth Charact. 2005, 50, 52−105.

[21] Kawazoe H, Yasukawa M, Hyodo H, Kurita M, Yanagi H and Hosono H 1997 *Nature* **389** 939

[22] Snure M and Tiwari A 2007 *Appl. Phys. Lett.* **91** 092123

[23] Santra S, Das N S and Chattopadhyay K K 2013 *Mater. Lett.* **92** 198

[24] Ruttanapun C 2013 *J. Appl. Phys.* **114** 113108

[25] Soylu M, Al-Ghamdi A A, Omran S B and Yakuphanoglu F 2014 *J. Alloys Compd.* **617** 602

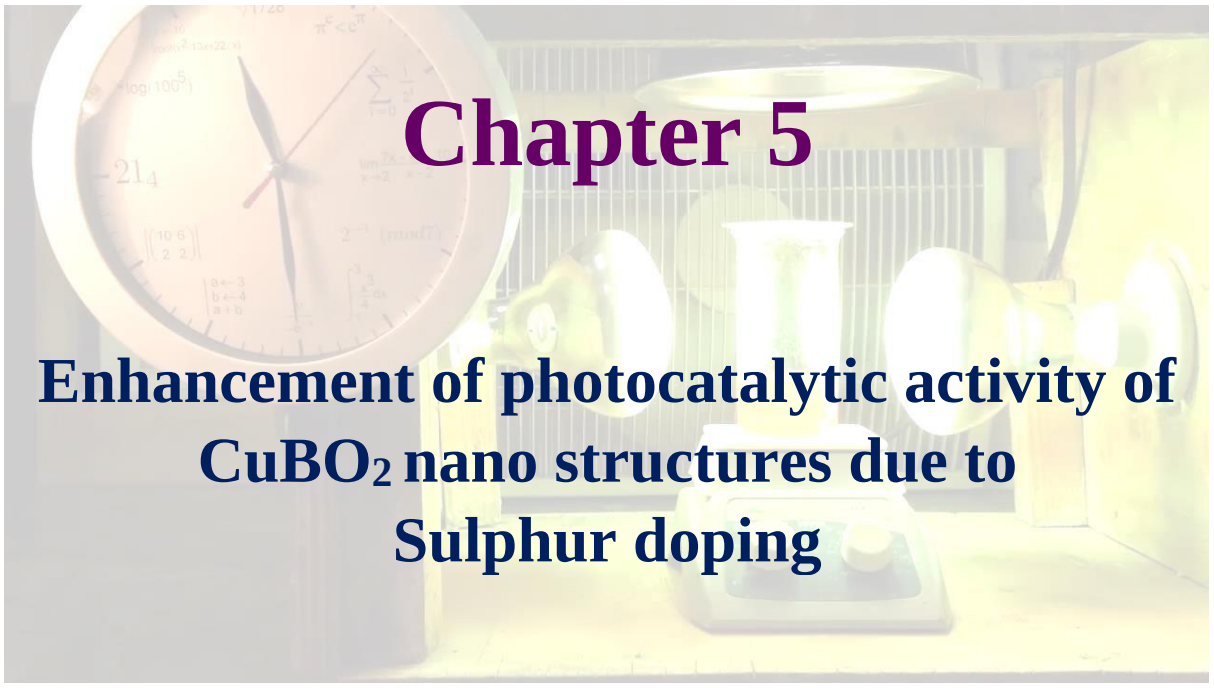

Chapter 5

Enhancement of photocatalytic activity of $CuBO_2$ nano structures due to Sulphur doping

Abstract

Different concentration of Sulphur doped Copper based delafossite $CuBO_2$ nanocrystalline powders of different grain sizes were synthesized via molten-salt route. Structural characterization was performed using X-ray diffraction (XRD) and transmission electron microscopy (TEM) which confirmed good crystallinity and proper phase formation of the samples. Field emission scanning electron microscopy (FESEM) revealed morphological information of the samples. Energy dispersive X-ray studies (EDX) were processed to identify the compositions of the materials. The photo catalytic performance of this delafossite material to degrade hazardous organic compound rhodamine B (RhB) was studied with a standard photo catalytic set-up and the photo catalytic efficiency was found to increase with decreasing grain size. According to my experiment, the photocatalytic rate constant and Efficiency for sample A (2%) is greater compared to pure $CuBO_2$ due to the Sulphur doping in pure $CuBO_2$.

5.1 Introduction

The fast and foremost interesting fields for the scientific research of martializing based electronics was developing p-type wide band gap metal oxides. Successful synthesis of suitablep-type TCOs with suitable optical and electrical properties is therefore treated as the key factor for exploring technologies like invisible electronics using wide band gap all transparent junction-based devices [1,2]. Hosonoet and other researchers were contributed for the progress in fabrication and characterization of various copper based delafossites[3]. Till now the electrical properties of $CuAlO_2$ can be compared with its n-type counterparts. So it is vital to look for a newer p-TCOs.

In metal oxides the valence band is made up of oxygen 2p orbital whereas the conduction band is mostly formed by spatially spread metal s orbital. As the p orbitals are localized in nature, hence even if holes are created by some external doping or due to non-stoichiometry (i.e. excess oxygen), the mobility of the holes are low and this is one of the main causes for inferior electrical conductivity of the p-type TCOs [4-5]. To overcome this barrier the brilliant concept of chemical modulation of valance band Cu delafossites such as $CuMO_2$ (M = Al, In ,Ga) were proposed. The unique structure of delafossites where the O–A–O dumbbell layers are interweaved with edge-sharingMO_6 blocks along the c-axis may help in achieving good

photocatalytic performance. we have found that it is comparatively easier to vary the grain size of this material in a controlled fashion by different concentration of Sulphur doped in $CuBO_2$.The large electronegativity of oxygen and the localised nature of p-orbital limits the hole mobility [6-8].This practical barrier helped us in search of a newer based delafossite and the latest member in this group is $CuBO_2$[9]. As reported $CuBO_2$is expected to have the largest band gap among the delafossite group as the ionic radius of Boron is the smallest in Group III elements [10].

Out of the broadest range of applications of Cu based p-TCOs nanomaterials, their use for eradication of organic dyes present in the industrial waste, a major threat to human lives, through photocatalytic degradation has not been explored at all till now. This will become an area of recent scientific interest not only due to their environmental friendly approach but on account oftheir huge commercial impact. Eradication of organic dyes through photocatalysis using n-type metal oxides like TiO_2 and ZnO has been explored over the last several years extensively [11–14]. Photocatalysis by semiconductor materials depend upon several factors like average dimension of the nanostructures, effective surface area, band gap, electron–hole pair recombination rate etc. The catalytic efficiency of the as-synthesized $CuBO_2$ and sulphur doped $CuBO_2$nanoparticlesware estimated by degradation of rhodamine B (RhB) dye in the presence of UV irradiation.

In previous work $CuBO_2$ nanoparticles was evaluated by degradation of rhodamine B (RhB) and methyl orange (MO) dyes in presence of UV irradiation. We have seen that higher the aspect ratio better will be the photocatalytic activity. In another work we have seen that nanocubes of copper delafossites have higher aspect ratio which in turn helps in better photocatalytic activity.

In this particular work, we have examined the hazardous dye degradation capability of prepared samples considering Rhodamine B as a standard dye dissolved in water. The entire experiment was carried out to obtain the time evolved UV-vis spectra of mixture solution in specific time intervals. We have also investigated grain size dependent performance of the novel p-type nanocrystals for its rhodamine B(RhB) degradation performance and observed results.

5.2 Synthesis and characterization

I have already discussed the synthesis of $CuBO_2$ and sulphur doped $CuBO_2$in chapter 4. In this particular work, Pure $CuBO_2$, 2%, 6% and 10% sulphur doped samples were subjected to photocatalytic performance investigation. The as-prepared samples were characterized by studying forproper phase formation with the X-ray diffraction (XRD; Bruker, D-8 Advance) with the Cu Ka radiation of wavelength l = 1.5406 A˚. The morphological natures of the as prepared samples were studied by a field emission scanning electron microscope (FESEM, Hitachi, S-4800). The exact particle size and lattice images along with selected area electron diffraction (SAED) pattern were determined from transmission electron microscopic (JEOL, 200 kV HRTEM) imaging. The elemental composition were analysed by energy dispersive X-ray diffractometer (EDX, associated with FESEM unit).

The photocatalytic activities of pure $CuBO_2$ and different concentration sulphur doped $CuBO_2$ (sample A, B, C, D) were studied with standard photocatalytic set up with dye RhB. Prior to the experiment, all the glassware and accessories were cleaned properly with dilute HCl and subsequently by multiple washing with DI waters. After that, they were dried properly to avoid any additional unwanted concentration modification. For a typical experiment, RhB stock solution of 0.01 g ml^{-1} was prepared. 10^{-5} M test solution of RhB was then prepared by adding required amount of de-ionized water to the stock solution. 0.015 g of prepared $CuBO_2$ and sample A, B, C, D powder samples were added to this test solution separately and stirred for 1 h in same speed in dark condition. Afterwards the solution containing each powder sample were kept under UV irradiation using one 40 W UV tube (Phillips) which emits wavelength of 254.6 nm (UV C) and the tube to suspension surface distance was kept at 15 cm. The abovementioned solutions were retained under UV emission for 120 min and parts of the solutions were collected in 30 minutes time intervals for absorption study.

5.3. Results and discussions

5.3.1. Crystallographic study

Figure 5.1. shows the XRD spectra of the as prepared samples. It can be seen that all the samples exhibit high degree of crystallinity as presented by the intense diffraction peaks. The XRD peaks appearing near 32º, 35º, 36º, 38º, 42º, 48º, 53º, 58º and 61º were assigned to be

arising due to reflections from (006), (100), (011), (012), (014), (106), (107), (108) and (0011) planes respectively. It can be also seen that an unidentified diffraction peak near 39^o which was explained to be occurring due to sulphur over doping. Lattice strain occurring within the samples was estimated using the relation

$$\varepsilon=\beta/4\tan\theta$$

Where β is the full width at half maxima of the diffraction peaks. The variation of lattice strain with sulphur doping is presented in figure 5.1. which showed that lattice strain initially decreased with minor amount of sulphur doping. However, the same was increased due to high doping amount which is expected in case of high concentration foreign element inclusion within a host lattice system.

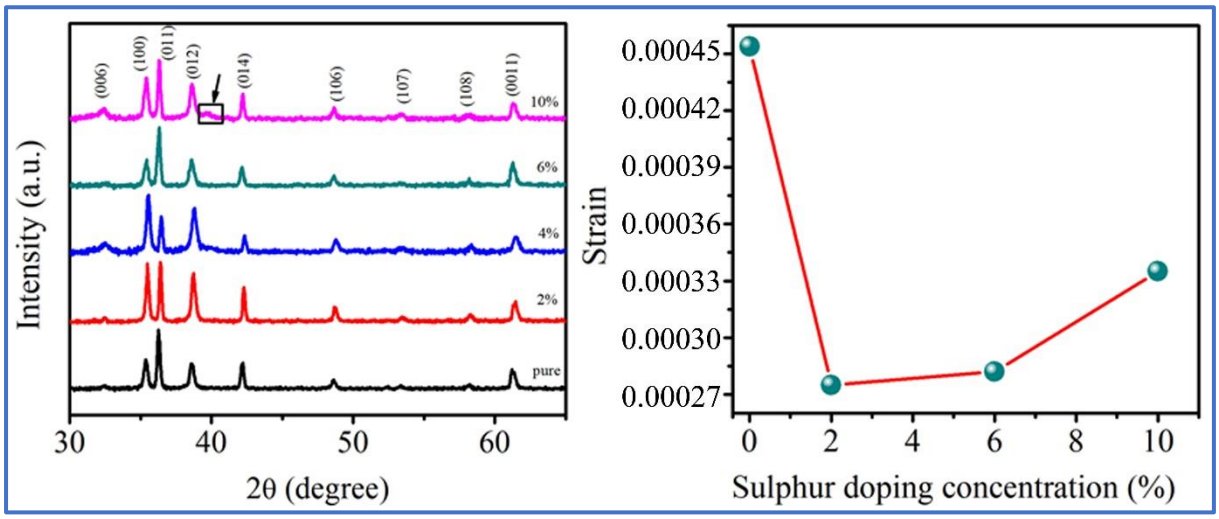

Figure 5.1: (a) XRD pattern of the sample and (b) Variation of Lattice strain with sulphur doping

5.3.2. Morphological study

FESEM images of pure and 6% s doped samples are presented in figure 5.2. It can be seen that the samples exhibit both rod like nature associated with non-uniform attachment of $CuBO_2$ nanoparticles, The diameter of the rod like structures was found ~ 70 nm whereas the length was found to be few micrometers. The particles attached to the surface of the rods were found to have dimension below 30 nm. Doping via sulphur did not affect the shape and dimension of the samples as reflected in figure 5.2.

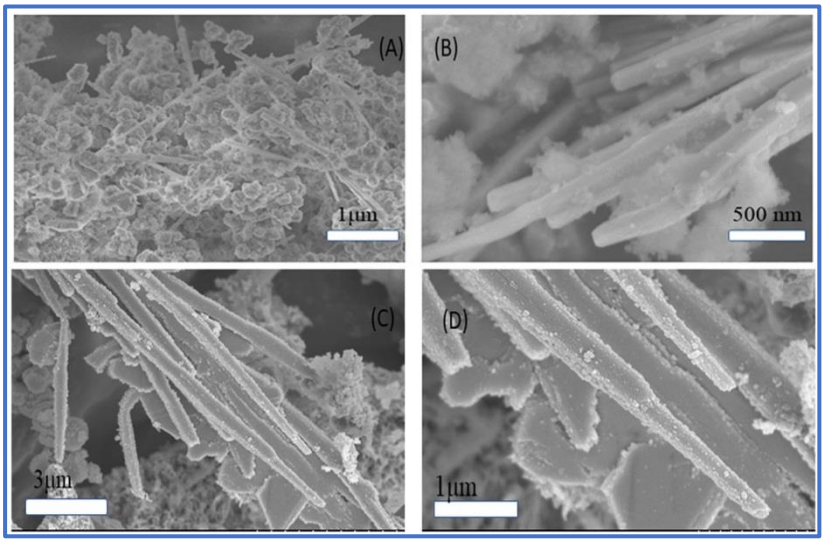

Figure 5.2: FESEM images of pure $CuBO_2$ (A and B) and Sample C (C and D)

5.3.3. Composition study

The elemental mapping of the 6% sulphur doped sample is presented in figure 5.3. It can be seen that all the elements are present in uniform distribution within the samples. Presence of all the constituent elements and the dopant element 'sulphur' can also be confirmed from the elemental mapping of EDX study.

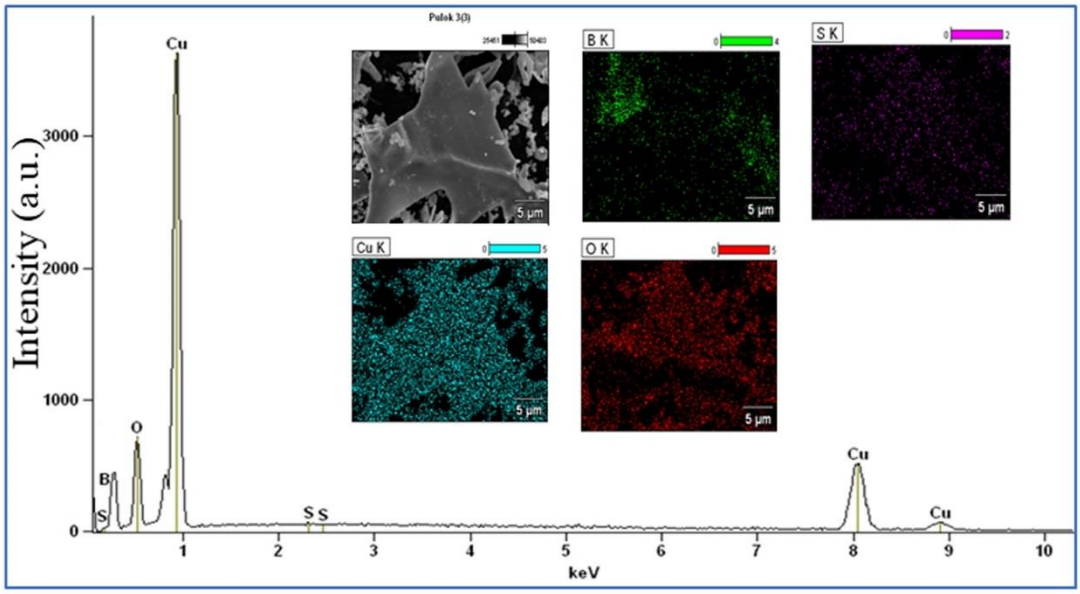

Figure 5.3: EDX spectra of Sample C (6% sulphur doped)

5.3.4 Photocatalytic activity analysis

The photocatalytic performances of the samples are presented in figure 5.4. The time evolved absorbance spectra of the pure and sulphur doped samples showed that the $CuBO_2$ sample doped with 2% sulphur could degrade the hazardous dye RhB less than 5% within 2h. This performance is much better than the activity shown by the pure $CuBO_2$ sample, i.e, degradation upto 30%. However, the performance of degradation of RhB gradually became inferior as the sulphur content was increased further (6%). It could degrade only 20% of the initial concentration of RhB though this is still better than the performance of the pure one. The photocatalytic dye removal efficiency became even more inferior for 10 % sulphur doped sample which could degrade less than 60% of the initial concentration of RhB.

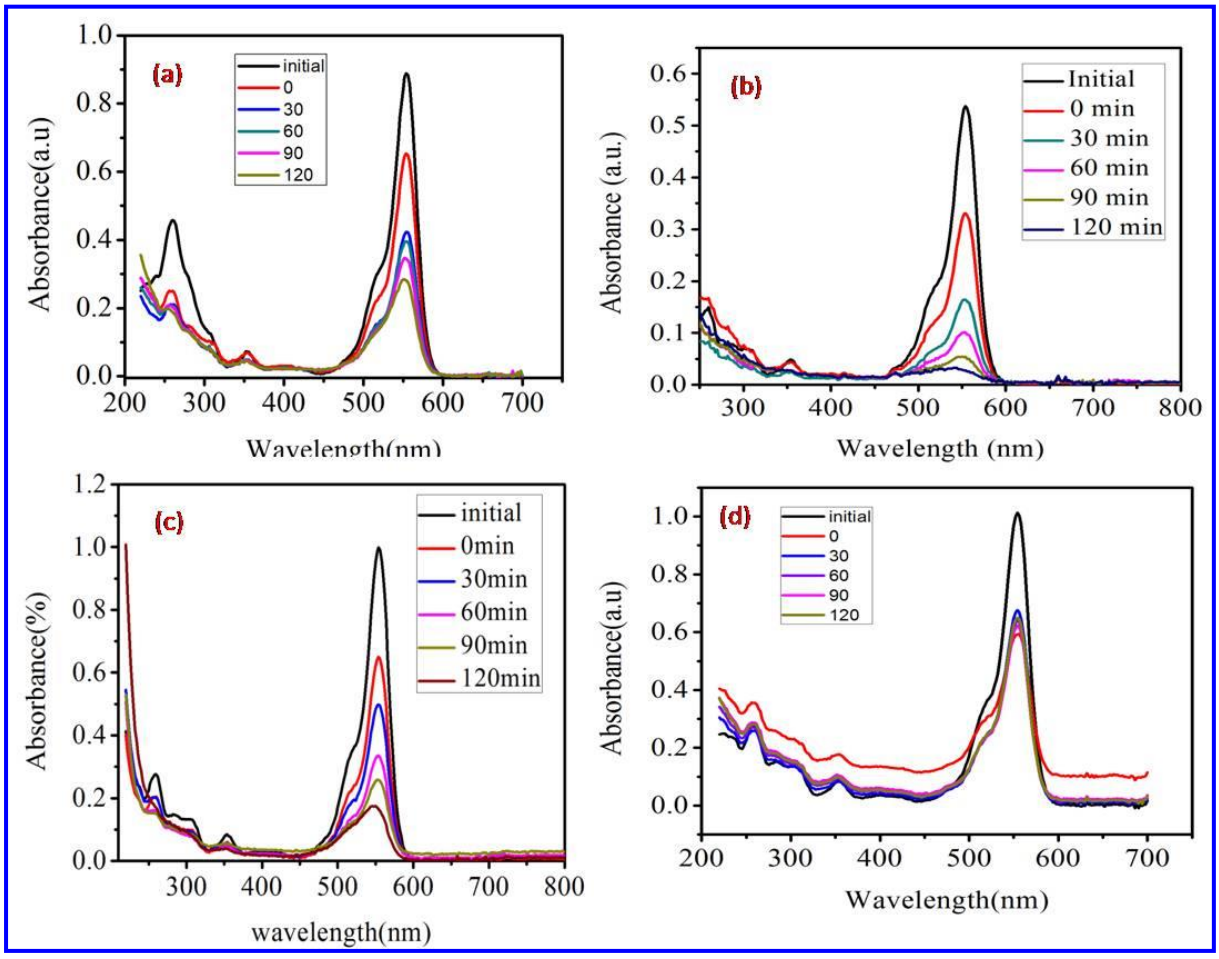

Figure 5.4: Time evolved UV-Vis spectra for photocatalytic activities of (a) Pure, (b) 2% , (c) 6% and (d) 10% S doped samples

A set of digital images of the filtrate collected in different time interval during the photocatalytic experiment is presented in figure 5.5 where it can be seen that the

decolourization of the Rh B solution occurred faster in case of the sulphur doped sample compared to the case when the pure sample was used as the active catalyst.

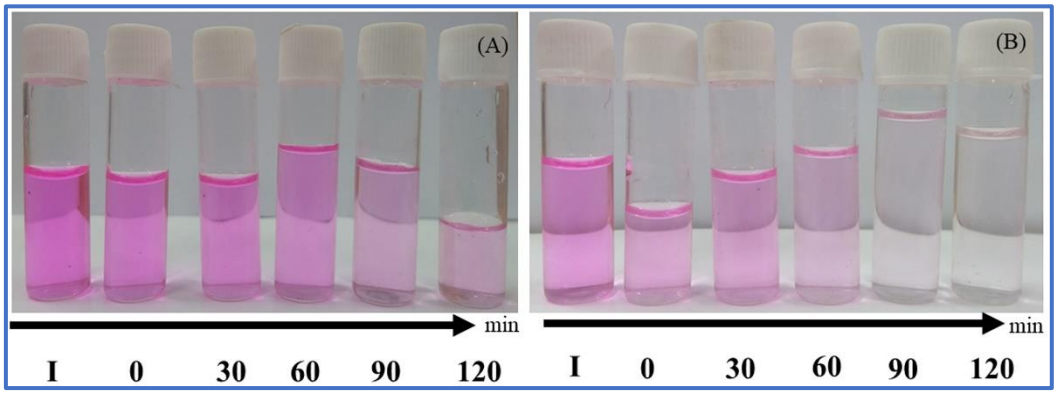

Figure 5.5: Digital images of the catalysis medium filtrate for (A) pure (B) 2% S doped sample

The photodegradation of RhB under UV irradiation can be demonstrated in the following steps. As soon as a $CuBO_2$nanostructure containing $CuBO_2$ molecules absorbs a UV photon of light with energy equal to or larger than its bandgap, an electron–hole pair (e-/h+) is generated and faces separation due to low dimension of the catalyst. This separation is also dependent upon the conductivity of that particular catalyst.

$$CuBO_2 \xrightarrow{h\nu} h^+ + \nu^- \quad 5.1$$

These photo generated carriers then reacts with water and absorbed oxygen leading to the formation of •OH radicals.

$$h^+ + H_2O \rightarrow \bullet\,\mathrm{OH} + H^+ \quad 5.2$$

These •OH radicals are well-known for their action as oxidizing agents for organic pollutants which gradually decomposes RhB molecules via the following steps

$$\bullet\, O_2^- + H^+ \rightarrow HOO\bullet \quad 5.3$$

$$e^- + HOO\bullet + H^+ \rightarrow H_2O_2 \quad 5.4$$

$$H_2O_2 + e^- \rightarrow \bullet\,\mathrm{OH} + OH^- \quad 5.5$$

$$\bullet\,\mathrm{OH} + \mathrm{RhB} \rightarrow intermediates \rightarrow degradation\ products \quad 5.6$$

Regarding the explanation of the photocatalysis performance of the samples, firstly, it is to be noted that the dye degradation efficiency of $CuBO_2$ nanostructured reported here is either comparable or better than some of the related previous reported works as can be seen in the following table 5.1. The presence of nanoparticles and high aspect ratio rod like nanostructures

may be accounted for such high degradation ability. The degradation efficiency of the samples along with degradation rate constants is represented in the following figure.

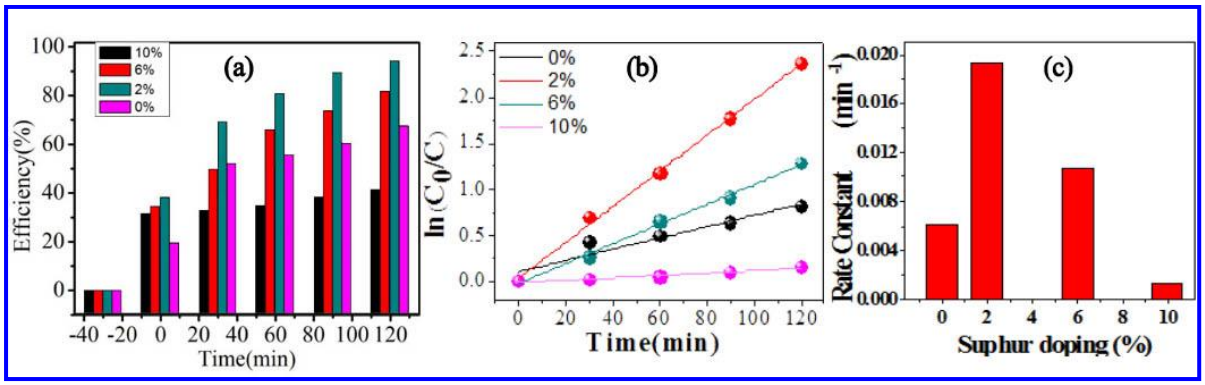

Figure 5.4: (a) Degradation efficiencies, (b) Ln(C_0/C) vs time plots (c) Variation of degradation rate constants for various samples

It can be clearly seen that the degradation efficiency is much increased for 2% S doped sample compared to the pure one. It is reflected even in increased degradation rate constant. The sample doped with 6% s also exhibit higher degradation rate constant than the pure one. However, smaller rate constant was obtained for 10% s doped sample. A direct correlation of degradation rate constant and the conductivity may be established from the results. Additionally, parameters related to crystallinity also affected the dye degradation efficiency of the samples. As soon as sulphur atoms were incorporated in the host $CuBO_2$ system, the conductivity of the sample increased. This enabled easy e^-/h^+ separation through more conducting paths. however, conductivity of the samples increased more in case of 6% S doped sample but the degradation rate constant slightly decreased compared to the 2% doped sample. This apparent anomaly can be explained considering the effect of crystallinity. Incorporation of foreign atom within a stable lattice system may locally enhance the defects. These defects may not be detectable in a fast x-ray scan but they should have considerable effect in charge movement through the crystal. Thus increment of conductivity should increase the possibility of photogenerated e^-/h^+ separation but presence of local defects within the crystal should hinder the charge movement. Thus an optimization is established in view of doping concentration which can have most favourable conductivity and lattice perfection. In this study, this optimum

condition was achieved for 2% S doped samples. Feasibility of this mechanism was clearly seen in the photocatalytic behaviour of 10% S doped sample. We saw in chapter 4 that the conductivity gradually increased from 2% to 6% S doped samples and it decreased remarkably for 10% S doped samples. In view of crystallinity, a new impurity peak occurred for 10% S doped samples. For 2% S doping, the conductivity is favourable and crystallinity is not much disturbed. Hence a remarkable enhancement of photocatalytic behaviour was found. For 6% S doping, conductivity is yet favourable, but crystallinity should be affected by higher impurity atoms, as result, photocatalytic activity became slightly inferior to 2% S doped sample but still better than the pure one. In case of 10% S doped sample, both the conductivity and crystalline features degraded than the other doped and pure sample. As a result, photocatalytic behaviour became inferior compared to other doped and pure sample.

This work is expected to open up new opportunities for application of copper based delafossites for smart water disinfection technology. There are plenty of methods available for increasing the conductivities of such delafossites and simply establishment of an optimum condition of crystalline perfection and conductivity may result into better delafossite photocatalyst.

Sample	Rate constant (min^{-1}) RhB	Experimental Condition				Reference
		Wavelength of UV light(nm)	UV source power(W)	Distance between source and solution(cm)	Amount of materials taken	
$CuBO_2$ nanoparticles	0.78023	254.6	80	~15	0.03g in 40ml sol	
TiO_2 (thin film)	0.00181	254	80	~10	6.25cm^2 thin film in 10ml sol	[15]
ZnO(Flower-like)	0.71700	High pressure	250		0.02 gm in 100ml sol	[16]
TiO_2-coated activated carbon	0.02070	Mercury lamp	50		0.5 gm in 200ml sol	[17]
2% sulphur doped $CuBO_2$	0.0193	254.6	40	~15	0.015 gm in 40ml sol	This work

Table 5.1: Comparison of photocatalysis performance of various systems

5.4. Conclusion

Pure and sulphur doped $CuBO_2$ samples were synthesized using molten salt method. Concentration of sulphur was varied by 2%, 6% and 10%. The samples showed proper crystallinity even after incorporation of s up to 6%. Compositional study by EDX confirmed proper elemental distribution and sulphur incorporation. Photocatalytic activity exhibited by the samples enhanced with an optimum amount of sulphur doping. The degradation rate constant enhanced around 0.02 min^{-1} for 2% S doped sample from 0.001 min^{-1} of the pure sample. Enhancement of photodegradation ability was correlated with enhanced conductivity and proper crystallinity of the sample. This work establishes the delafossite system to be flexible for photocatalytic application upon tuning by doping.

References

[1]A.P. Ramirez, Science 315 (2007) 1377–1378.

[2] T. Kamiya, H. Hiramatsu, K. Nomura, H. Hosono, J. Electroceram. 17 (2006) 267–275.

[3] H. Kawazoe, M. Yasukawa, H. Hyodo, M. Kurita, H. Yanagi, H. Hosono, Nature 389 (1997) 939–942.

[4] A.N. Banerjee, S. Kundoo, K.K. Chattopadhyay, Thin Solid Films 440 (2003) 5–10.

[5] A.N. Banerjee, C.K. Ghosh, K.K. Chattopadhyay, Sol. Energy Mater. Sol. Cells 89 (2005) 75–83.

[6] A.N. Banerjee, S. Kundoo, K.K. Chattopadhyay, Thin Solid Films 440 (2003) 5-10.

[7] A.N. Banerjee, C.K. Ghosh, K.K. Chattopadhyay, Sol. Energy Mater. Sol. Cells 89 (2005) 75-83.

[8] R. Laskowski, N.E. Christensen, P. Blaha, B. Palanivel, Phys. Rev. B 79 (2009) 165209/1-7.

[9] M. Snure, A. Tiwari, Appl. Phys. Lett. 91 (2007) 092123/1-3.

[10] X. Nie, Su-H. Wei, S.B. Zhang, Phys. Rev. Lett. 88 (2002)066405/1-4.

[11] U.N. Maiti, S. Maiti, K.K. Chattopadhyay, Cryst. Eng. Commun. 14 (2012) 640–647.

[12] J. Matos, A. Garica, L. Zhao, M.M. Titirici, Appl. Catal. A 390 (2010) 175–182.

[13] A. Moulahi, F. Sediri, N. Gharbi, Mater. Res. Bull. 47 (2012) 667–671.

[14] N. Yan, Z. Zhu, J. Zhang, Z. Zhao, Q. Liu, Mater. Res. Bull. 47 (2012) 1869–1873

[15] A. Subrahmanyam, K.P. Biju, P. Rajesh, K.J. Kumar, M.R. Kiran, Sol. Energy Mater. Sol. Cells 101 (2012) 241–248.

[16] Y. Lai, M. Meng, Y. Yu, X. Wang, T. Ding, Appl. Catal. B 105 (2011) 335–345.

[17] W. Zhang, Y. Li, C. Wang, P. Wang, Desalination 266 (2011) 40–45.

Chapter 6

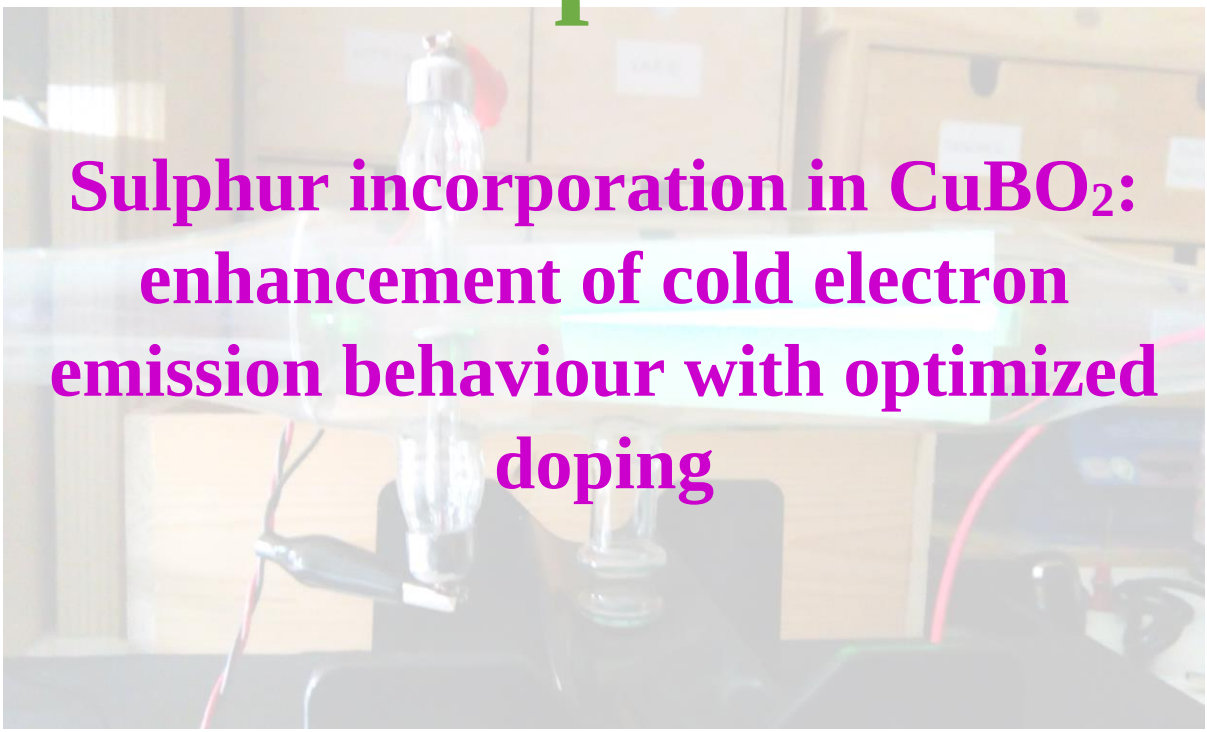

Sulphur incorporation in $CuBO_2$: enhancement of cold electron emission behaviour with optimized doping

Abstract

Copper based delafossites, p-type transparent conducting oxides (p-TCO) are technologically very important. Pure $CuBO_2$ and sulphur doped $CuBO_2$ nanorods were synthesized via easy molten salt route. All the samples were synthesized at 800^0c in blue box furnace for 180 minutes. The prepared samples were characterized for structural information using X-ray diffraction (XRD) that revealed the proper crystalline phase formation of $CuBO_2$. Field emission scanning electron microscopy (FESEM) and transmission electron microscopy revealed the morphological information of the samples. Compositional studies were performed by energy dispersive analysis of X-rays. Finally, the samples were characterized to study the field emission (FE) properties of the same using a laboratory-made high-vacuum field-emission setup which showed very good field emission performance. The information regarding the work function was theoretically obtained using density functional theory. Those values were used to find out cold emission parameters like field enhancement factor. It was observed that the higher grain sized $CuBO_2$ nanorods were actually better field emitters. In this studies, we observed that field enhanced factor increased by increasing a certain percentage of Sulphur doping in pure $CuBO_2$.

6.1 Introduction

TCOs are one of the most important novel nanomaterials which proved as promising candidates for optoelectronics device technology and junction based “invisible device” fabrication. The nanostructures-based p-type TCOs are paying attention for their rear combination of excellent electrical and optical properties. Ternary metal oxides and their nanostructures are well investigated for revealing optical properties like photoluminescence [1-2], easily tunable optical band gap [3-4], remarkable photocatalytic performance [5-6], excellent electrical properties like room temperature electrical conductivity [7], good thermoelectrical properties [8] and microscopic field emission performance [9]. However, industrial usage of TCO nanostructures are mainly dominated by n-type oxides like SnO_2, ZnO, In_2O_3, etc [10-13] and their p-type counterparts are comparatively less used for these purposes. The reason is p-type TCOs are generally considered to exhibit inferior electrical conductivity compared to the n-types, and thus they are not appropriate candidates to be used in smart applications like “invisible electronics” [14]. Strongly localized nature of p orbitals in O 2p states in p-type binary oxides restricts carrier mobility for holes and therefore introduces a harder barrier for

obtaining appreciable conductivity. Doping of n-type oxides sometimes solves the problem partially, but the necessity of development of highly conducting intrinsic p-type TCOs can never be ignored. The first successful attempt toward this was reported by Kawazoe and his co-workers [15], who introduced the theory of "chemically modulated valence band" (CMVB) and smart p-type TCO $CuAlO_2$ having enhanced electrical conductivity and good transparency. In this case hybridization of d orbital of Cu with p orbital of oxygen is enabled better hole mobility. Exploiting the principle of chemical modulation of valence band, several cooper based delafossites were developed having $CuMO_2$ structure with M as Cr, Fe, Ga, Sc, Y, etc [16-19]. Those Cu delafossites and their nanostructures exhibit very high conductivity and appreciable transmittance. In some of our earlier studies, we reported high performance cold cathodes [20-21]and thermoelectric26 systems involving $CuAlO_2$. We also extended this work on the new copper delafossite $CuBO_2$ which was first reported by Snure et al. in 2007 [22].

Along with other electrical properties, Cu delafossites are also important for exhibiting field driven electron emission[9].It is well known that the electron field emission depends upon several factors like surface morphology [23] and defect state density [24] also better conductive nanomaterial often show enhanced FE properties which may offer considerable progress for applications in low power consuming flat panel display [25]. Theoretical reports indicate the band gap of $CuXO_2$ compounds increase with the decreasing ionic radius of X (where X is the Group III elements) and hence $CuBO_2$ should have the largest band gap [26] among the copper delafossites and should possess very low electron affinity which effectively can enhance electron emission. Driven by this idea of using better conductive p-TCO for FE applications.

It was observed that Sulphur doped $CuBO_2$ exhibited excellent field emission properties with high emission current density than pure $CuBO_2$. The grain size of the delafossite was found to considerably affect the FE performance.

6.2 Synthesis and Characterization

Synthesis of all samples and characterizations for this works are as same as demonstrated in the chapter 4. In this particular work, sulphur doped $CuBO_2$ synthesis was carried out for 2%, 4%, 6% and 10% doping. All of the samples were characterized with x-ray diffractometer for proper phase formation, EDX spectrophotometer was used to find out composition related information and field emission scanning electron microscopies studies were performed to

investigate morphological features. Finally all of the samples with proper phase purity were studied for their field emission behavior under our laboratory made high vacuum field emission set up.

6.2.1. Field emission experiment

Field emission properties of pure and S doped $CuBO_2$ samples were performed in our high vacuum field emission setup by using a diode configuration. The setup is made of two electrodes of a stainless-steel conical tip (1.5 mm diameter) acting as a anode. The base steel plate also comprises more than one metallic clips which can attach the thin film sample with the base. Then the as prepared thin film samples were positioned onto the steel base platform and the metallic clip was tightened on the previously masked part of the ITO film where the samples were not deposited. The interelectrode separation was made adjustable to a few hundred micrometers by means of micrometer screw, and the measurement ware performed keeping tip-sample distance at 100 μm. Then the entire diode system was placed in in a transparent chamber which was evacuated up to ~10^{-7} mbar base pressure using a compound setup of rotary and oil diffusion pump. The surface of the sample was kept under observation through the chamber view port, which enabled us to recognize any discharge, if occurring at all. It was confirmed that no discharge occurred during the application of high electric field, and hence the currents observed in these measurements were considered to be cold field emission of electron from the samples.

The emission current I and the applied voltage E are theoretically related by the following equation

$$I = (Aa\beta^2E^2/\phi) \exp [-b\phi^{3/2}/ (\beta E)] \qquad (6.1)$$

Where ϕ and β are the local work function and the field enhancement factor respectively, A is the emission area (= area of the anode tip = $(\pi/4)*1.5$ mm^2), a, b are Fowler-Nordheim constants having values a = $1.56*10^{-10}$ and b = $6.83*10^3$ $eV^{-3/2}$ V μm^{-1} . The applied voltage E was determined by dividing the external voltage (V) by the actual inter electrode distance d which was maintain the same (100 μm) throughout the experiment.

Equation (1) can further be written as

$$\ln(J/E^2) = \ln (a\beta^2/\phi) - b\phi^{3/2}/(\beta E) \qquad (6.2)$$

Where J = I/A is emission current density.

Therefore, a plot of $\ln(J/E^2)$ vs 1/E should result into a straight-line having slope (say m) = $-b\phi^{3/2}/\beta$ and intercept = $\ln(a\beta^2/\phi)$. So from the values of the slope, the field enhancement factor β can be figured out using the following equation

$$\beta = -b\phi^{3/2}/m \quad (6.3)$$

6.3. Result and discussion

6.3.1. Structural studies

The XRD patterns of the samples are presented in figure 6.1. The distinct and intense peaks occurring in the spectra indicate the formation of proper rombohedral phase of $CuBO_2$ [JCPDS]. The peaks were assigned to as (006), (100), (011), (012), (014), (106), (107), (108) and (0011) planes of rombohedral $CuBO_2$ which occurred near 32°, 35°, 36°, 38°, 42°, 48°, 53°, 58° and 61°. No peak corresponding to sulphur precursor or elemental sulphur was observed which indicate proper doping of S as impurity element. The grain sizes of the samples were calculated using well known Scherar equation

$$L = \frac{0.9\lambda}{\beta Cos\theta}$$

Where β is the full width at half maxima of XRD peaks. The variation of grain size with s doping concentration is presented in figure 6.1. It can be clearly seen that a minor decrement of grain size was obtained due to sulphur doping.

The exact reason of grain size variation may be correlated with atomic dimension of dopant. It is true that sulphur was selected as the potential dopant due to its ionic similarity as a replacement of oxygen, but high amount of sulphur doping should hinder the larger grain growth which is reflected in low smaller grain size obtained for high concentration of incorporated sulphur within the host $CuBO_2$ system.

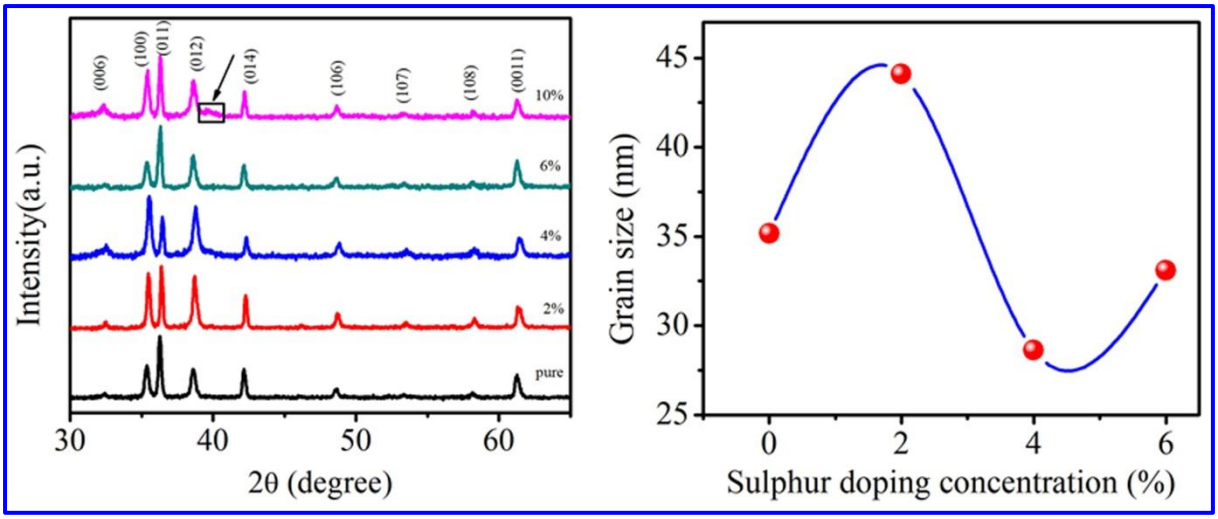

Figure 6.1: XRD patterns of $CuBO_2$ and different percentage sulphur doped $CuBO_2$

6.3.2. Morphological studies

Figure 6.2 presents the FESSEM images of pure and 4% sulphur doped samples. It can be observed that similar to the samples discussed in chapter 5, all the samples exhibit a non-uniform mixture of rod like and particulate features both in pure and doped form. The average size of the particles distributed in the image was determined to be below 30 nm.

The rod like structures were few micrometres long with diameters ~ 70 nm. No direct correlation of doping concentration and morphological features were found.

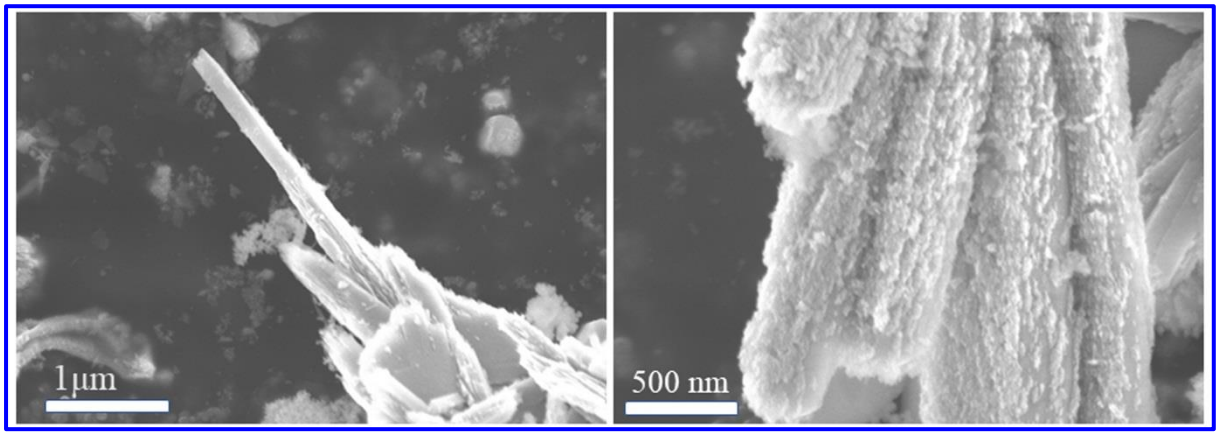

Figure 6.2: FESEM images of 4% S doped samples

To acquire clearer insight about the dimension of the nanorods, transmission electron microscopic studies of the samples were also carried out. The obtained micrographs are

presented in figure 6.3. In a first look, the non-distinct feature and close existence of nanorods and nanoparticles can be found. This is in well agreement with the FESEM images of the samples where particles were found to be closely attached with the nanorods. However, the agglomeration may also be contributed by stirring performed during TEM grid preparation. It can be seen that the diameter of the rods are 60 nm whereas they have an average length of 0.7 μm. The lattice images obtained for the samples were further analysed to reconfirm proper crystallinity of the samples. It can be seen that distinct lattice image with (012) planes are visible within the rods. It is to be noted that the diffraction peak corresponding to that particular lattice plane is the most intense one as observed in XRD studies. The spacing measured from the HRTEM image was ~ 2.33 Å. This is also very close to the data observed from JCPDS. The intense and distinct image of the lattice fringes with different spacing ensures the presence of multiple lattice planes which indirectly indicates the polycrystalline nature of the samples.

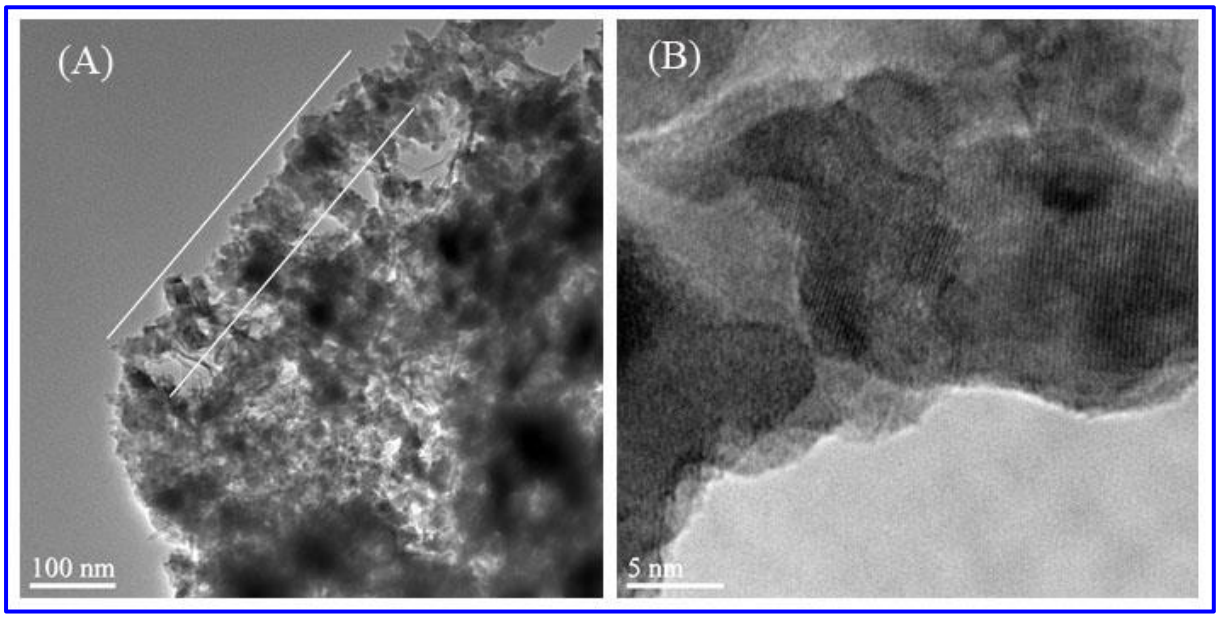

Figure 6.3: (a) TEM and (b) HRTEM lattice images of 4% S doped sample

6.3.3. Composition studies

The EDX data obtained for 4% S doped samples are presented in figure 6.4. It can be seen that all the expected constituent elements and the dopant element S is present in the sample. All elements are in general uniformly distributed and no trace of any additional impurity was obtained within the doped samples. The presence of sulphur inferred from EDX study confirmed successful incorporation of the same within host $CuBO_2$.

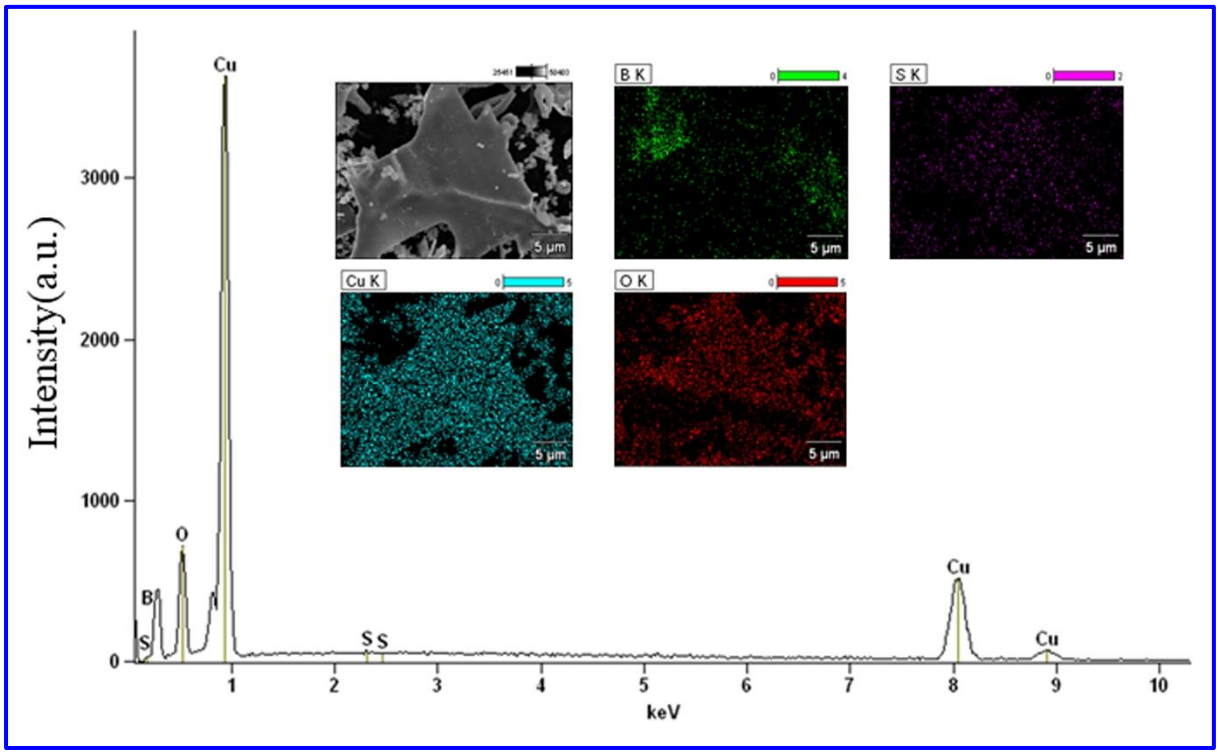

Figure 6.4: EDX spectra of Sample B (4%)

6.3.4. Field emission studies

The field emission performances of the as prepared samples are depicted in figure 6.5. It can be observed that the samples exhibited moderate field emission properties. However, the emission current densities definitely enhanced after sulphur doping. Highest emission current density, which is more than 300 $\mu A/cm^2$ was observed for sample doped with 2% and 4% sulphur though sample doped with 4% S achieved that current density at much lower applied electric field. However current densities decreased when impurity doping increased further upto 4% though it reached a higher value compared to the pure sample.

The turn-on filed was defined as the external field required for extracting emission current density of 5 $\mu A/cm^2$ was estimated for the samples. It was observed that the pure and 2% S doped samples exhibit high turn-on field and their values are close. The turn-on field gradually decreased with further increment of doping concentration and reached a minimum value for 6% sulphur doped samples.

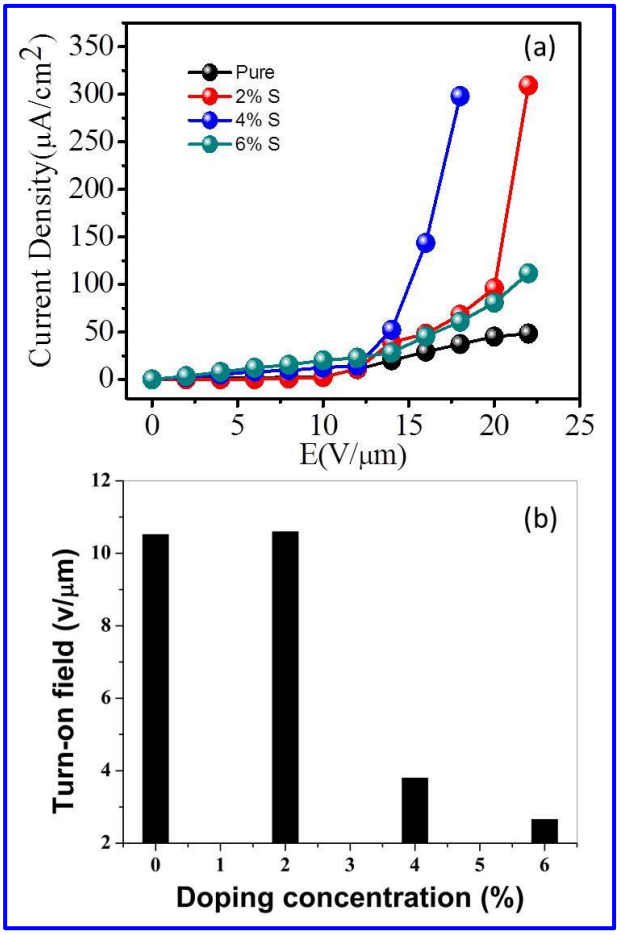

Figure 6.5: (a) Emission current density and (b) Turn-on field variation of the samples

It may be noted that the performance of the samples as cold cathodes vary in view of emission current density and turn on field. Firstly, the undoped sample performed the worst as far as emission current density and turn-on field is concerned. The reason is the lowest conductivity as obtained in chapter 4. The sample doped with 2% exhibited moderate current density but it required high external field for that. It could emit higher current density than the pure one due to increased conductivity, i.e., higher carrier density in the sample. But it yet could not emit highest current density due to its high grain size. The 4% S doped sample emitted the highest current density under a low field. This could happen due to its lowest grain size and moderate conductivity. The 6% S doped sample had the highest conductivity but it did not show any appreciable current density. However, it showed a low turn-on field. Actually, low grain size ensured the presence of high aspect ratio individual emitters which is able to emit sufficient current to exhibit low turn on field. However, presence of too many emitters of high carrier density enables screening effect which hinders high output current at high field. Thus the

sample doped with 4% sulphur was found to be the most optimized one for field emission based applications.

Another very important parameter to estimate the field emission behavior of any sample is field enhancement factor. This is determined using the slope of the FN plots obtained from field emission data. The FN plots of the samples are presented in figure 6.6.

It can be clearly seen that all samples exhibit negative FN slopes which ensures cold electron emission. The work function of $CuBO_2$ was considered to be 4.79 eV [27] as obtained from earlier theoretical calculations. The field enhancement factor increased remarkably with sulphur doping. The exact values of enhancement factors are very high for the pure and 2% S doped samples. However, after higher doping the enhancement factor increased though it did not vary much for samples doped with 4% S and 6% S. This variation may be accounted for the increased conductivity of $CuBO_2$ nanostructures with sulphur doping.

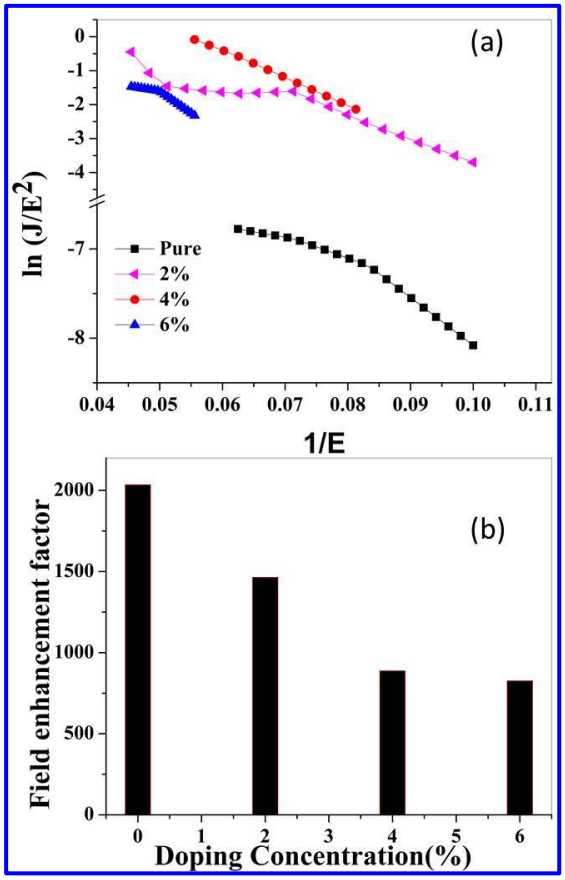

Figure 6.6: (a) FN plots and (b) Field enhancement factors of the samples

6.4. Conclusion

Pure and sulphur doped $CuBO_2$ nanostructures were synthesized using molten salt method. Proper phase formation was confirmed from XRD studies where as sample doped with 10% S showed inferior phase purity. Grain sizes of the samples were found to vary with sulphur doping. Compositional purity and presence of S was confirmed using EDX study. No special variation of dimension and shape could be observed from morphological studies. The samples were found to exhibit cold electron emission. Highest current density of ~ 300 $\mu A/cm^2$ was obtained for $CuBO_2$ samples doped with 4% S and it exhibited low turn-on field of 2.6 V/μm. The emission current density, turn on field and field enhancement factors were found to be governed by factors like grain size and conductivity.

Reference

[1] Santra S, Das N S and Chattopadhyay K K 2012 Proc. SPIE 8549 85491W/1

[2] Rastogi A C, Lim S H and Desu S B 2008 J. Appl. Phys. 104 023712/1

[3] Vanderbilt D 1990 Phys. Rev. B : Condens Matter 41 7892

[4] Sheng S, Fang G, LiC, Xu S and Zhao X 2006 Phys. Stat.Sol.203 1891

[5] Pack J D and Monkhorst H J 1977 Phys. Rev. B:Condens Matter. 16 1748

[6] Santra S, Das N S and Chattopadhyay K K 2013 Matter. Res. Bull. 48 2669

[7] Kawazoe H, Yasukawa M, Hyodo H, Kurita M, Yanagi H and Hosono H 1997 Nature 389939

[8] Banerjee A N, Maity R, Ghosh P K and Chattopadhyay K K 2005 Thin Solid Films 474 261

[9] Banerjee A N and Joo S W 2011 Nanotechnology 22365705/1

[10] Yang, B.; Kumar, A.; Zhang, H.; Feng, P.; Katiyar, R. S.; Wang, Z. J. Phys. D: Appl. Phys. 2009, 42, 045415/1−5.

[11] Tiwari, A.; Snure, M. J. Nanosci. Nanotechnol. 2008, 8, 3981−3987

[12] Mazumder, N.; Sen, D.; Saha, S.; Ghorai, U. K.; Das, N. S.;Chattopadhyay, K. K. J. Phys. Chem. C 2013, 117, 6454−6461.

[13] Jeong, J. A.; Jeon, Y. J.; Kim, S. S.; Kim, B. K.; Chung, K. B. Sol. Energy Mater. Sol. Cells 2014, 122, 241−250.

[14] Thomas, G. Nature 1997, 389, 907−908.

[15] Kawazoe, H.; Yasukawa, M.; Hyodo, H.; Kurita, M.; Yanagi, H.; Hosono, H. Nature 1997, 389, 939−482.

[16] Varadarajan, V.; Norton, D. P. Appl. Phys. A: Mater. Sci. Process. 2006, 85, 117−120.

[17] Park, S.; Keszler, D. A. J. Solid State Chem. 2003, 173, 355−358.

[18] Moharam, M. M.; Rashad, M. M.; Elsayed, E. M.; Shahba, R. M. A. J. Mater. Sci. 2014, 25, 1798−1803.

[19] Trari, M.; Bouguelia, A.; Bessekhouad, Y. Sol. Energy Mater. Sol. C 2006, 90, 190−202

[20] Banerjee, A. N.; Ghosh, C. K.; Das, S.; Chattopadhyay, K. K. Physica B 2005, 370, 264−276.

[21] Banerjee, A. N.; Chattopadhyay, K. K. Appl. Surf. Sci. 2004, 225, 243−249.

[22]Snure, M.; Tiwari, A. Appl. Phys. Lett. 2007, 91, 092123.

[23] Stratakis E, Kymakis E, Spanakis E , Tzanetakis P and Koudoumas E 2009 Phys. Chem. Chem. Phys. 11 703

[24] Kale V S,Prabhakar R R, Pramana S S, Rao M, Sow C H,Jinesh K B and Mhaisalkar S G 2012 Phys. Chem. Chem. Phys.14 4614
[25] Xiang B, Zhang Y, Wang Z, Luo X H, Zhu Y W, Zhang H Z and Yu D P 2005 J. Phys. D: Appl. Phys. 38 1152
[26] Nie X, Wei S H and Zhang S B 2002 Phys. Rev. Lett. 88 066405/1
[27] Santra, S.; Das, N. S.; Sen, D.; Chattopadhyay, K. K. Cubo2: A New Highly Transparent P-Type Wide Band Gap Electron Field Emitter. J. Phys. D: Appl. Phys. 2014, 47, 505301.

Chapter 7

Grand conclusion and Scope for future works

7.1 Grand conclusion

This thesis demonstrates an in-depth study of variation of different properties $CuBO_2$ in its pure form and after sulphur doping in various amounts.

In the first section of my work, sulphur doped $CuBO_2$ delafossites were synthesized using molten salt method. XRD studies revealed the proper phase formation. A slight deformation of the phase was obtained for high amount of sulphur doping. Morphological studies with FESEM and TEM confirmed nanostructural dimension of the samples with rod-like shapes of 22.77 nm diameter. The transport properties of the samples were investigated using standard method which showed a remarkable enhancement of conductivity by 4%. However, an optimized value of sulphur doping concentration (6%) was observed for the samples beyond which, the conductivity of the system became inferior again. This phenomenon was accounted for the increased lattice distortion and grain boundary resistance due to heavy sulphur doping. This work opens up a new opportunity to enhance conductivity of novel copper delafossites via replacing the host anions by higher atomic radii chalcogenide atoms.

After achieving success in increasing the conductivity of CuBO2 via doping with sulphur, I attempted the photocatalysis properties of the pure and doped samples. For this, Pure and sulphur doped CuBO2 samples were synthesized using molten salt method. Concentration of sulphur was varied by 2%, 6% and 10%. The samples showed proper crystallinity even after incorporation of s upto 6%. Compositional study by EDX confirmed proper elemental distribution and sulphur incorporation. Photocatalytic activity exhibited by the samples enhanced with an optimum amount of sulphur doping. The degradation rate constant enhanced around 0.02 min-1 for 2% S doped sample from 0.001 min-1 of the pure sample. Enhancement of photodegradation ability was correlated with enhanced conductivity and proper crystallinity of the sample. This work establishes the delafossite system to be flexible for photocatalytic application upon tuning by doping.

In the next section, I attempted the study of cold electron emission performance of the samples. Firstly, like the previous works, pure and sulphur doped $CuBO_2$ nanostructures were synthesized using molten salt method. Proper phase formation was confirmed from XRD studies where as sample doped with 10% S showed inferior phase purity. Grain sizes of the samples were found to vary with sulphur doping. Compositional purity and presence of S was confirmed using EDX study. No special variation of dimension and shape could be observed from morphological studies. The samples were found to exhibit cold electron emission. Highest current density of ~ 300 $\mu A/cm^2$ was obtained for $CuBO_2$ samples doped with 4% S and it

exhibited low turn-on field of 2.6 V/μm. The emission current density, turn on field and field enhancement factors were found to be governed by factors like grain size and conductivity.

7.2 Scope for future works

Due to time restriction, some important extensions of the work could not be performed which could lead to many important applications of this novel delafossite system. Additionally some important characterizations involving the samples synthesized in this work could clear up many important understanding regarding pure and doped $CuBO_2$ system. The following may be performed to achieve better understanding about the system.

[1] Detail study on Raman spectroscopy of the samples could be done in order to find out the actual change in carrier concentrations in the samples before and after sulphur doping.

[2] The samples showed optical band gap in UV-range, the effect of UV irradiation on the samples in view of conductivity could be a matter of great interest.

[3] After successful incorporation of sulphur, other chalcogenide atoms could also be used for doping. Depending upon the ionic radii of the dopants, successful doping could result into even better conductivity of $CuBO_2$.

[4] Photocatalysis study could be extended with scavengers test to find out the underlying actual mechanism of dye removal and recognition of responsible degradation agent(s).

[5] The samples could be subjected to phenol media and/or dye mixture solutions to find out the capability of the sample in actual application aspects.

[6] The effect of pH, catalyst load, dye concentration, recyclability test, dark stirring duration could be tested in order to find out its real performance as a smart photocatalyst.

[7] The effect of UV irradiation on the field emission properties could also be investigated

[8] A detail study on the change of work function of $CuBO_2$ after sulphur doping could be associated with present work to determine the actual possible effect on field enhancement factor. For this, theoretical studies with density functional theory could be performed so that effect of other dopants for better FE behaviour could be attempted without much uncertain experimental attempts.

[9] A detail study of dielectric properties could be performed so that those data can be used as inputs for theoretical simulation of field emission properties via ANSYS

MAXWELL software. This can help for actual application oriented optimization of electrode separation, base selection etc.

There may be several new applications which could be tested with pure and S doped $CuBO_2$ samples.

[1] As there was a remarkable enhancement of conductivity after S doping, different attempts could be made to fabricate an appropriate p-n junction diode with some suitable n-type counterpart.

[2] Charge storage capability of the pure and doped $CuBO_2$ samples could be studied in detail.

[3] Resistive switching properties of the sample could also be very important in order to apply this delafossite in future memory devices.